ISSN 0915-633X

NATIONAL INSTITUTE FOR FUSION SCIENCE

Energy Loss Mechanism of a Gold Ion Beam on a Tandem Acceleration System

A. Taniike

(Received - Apr. 25, 1995)

NIFS-352 May 1995

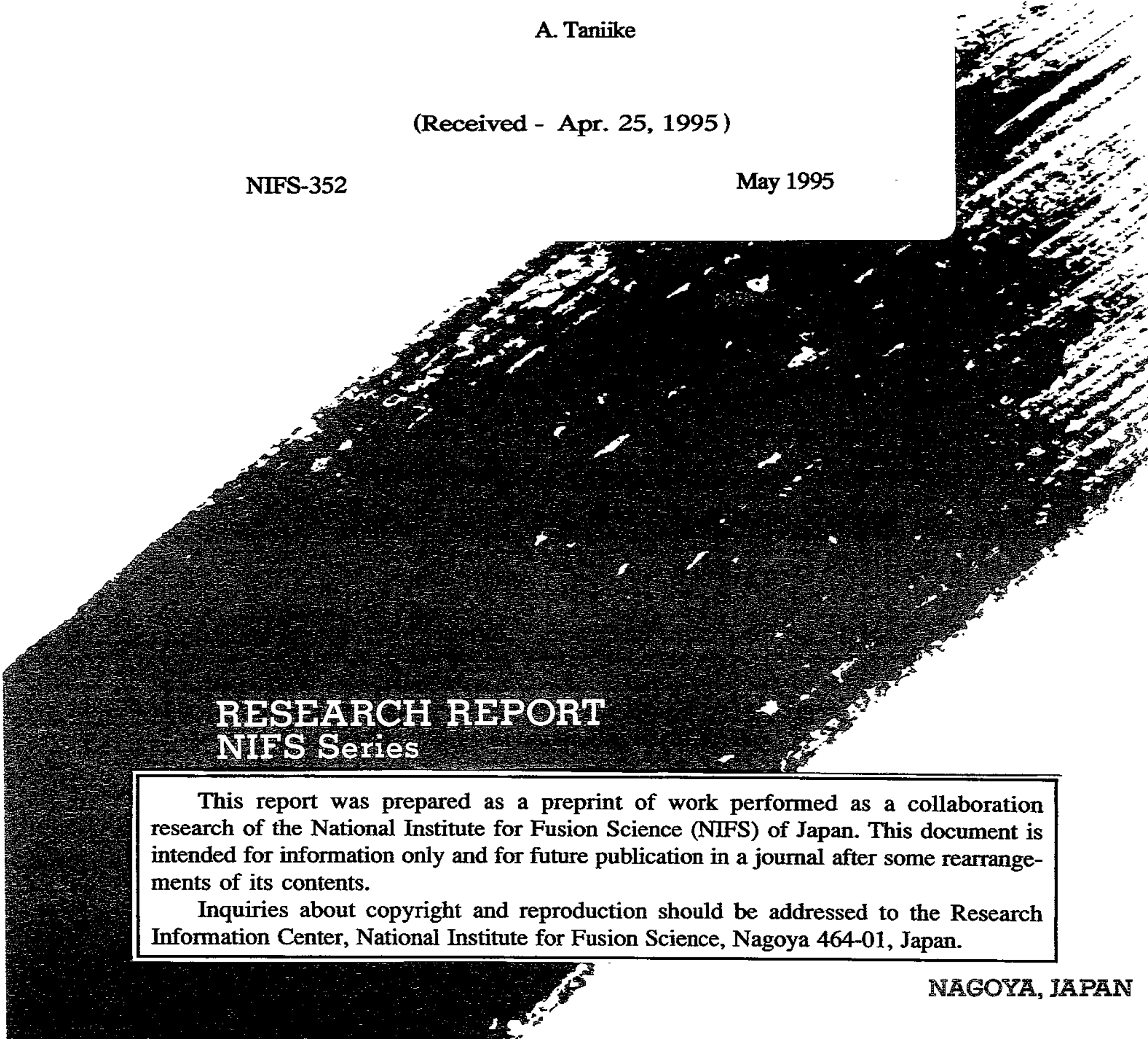

RESEARCH REPORT
NIFS Series

NAGOYA, JAPAN

Energy Loss Mechanism of a Gold Ion Beam on a Tandem Acceleration System

Akira Taniike

Doctor of Philosophy Thesis

Department of Fusion Science
The Graduate University for Advanced Studies

Abstract

A heavy ion beam probe (HIBP) is used as a reliable method to measure plasma potential and its fluctuation in a magnetically confined fusion plasma. A singly charged positive ion beam of mass about 200 amu with energy of 6 MeV is required in order to apply the HIBP to a large and strong magnetic field device such as the Large Helical Device (LHD) which is under construction at National Institute for Fusion Science, Japan. A primary beam with a small energy spread and of a current larger than 10 μA is required to measure the plasma potential as small as a few keV.

The origins of the energy spread on a tandem acceleration system are:

1. the fluctuation of acceleration voltage,
2. the energy spread of negative ions produced in an ion source,
3. the energy broadening caused in a charge stripping gas cell.

In the present work, I have carried out experimental and theoretical studies mainly on the second and the third problems.

In order to study energy loss mechanism on a tandem acceleration system, a tandem acceleration test stand has been constructed, and the charge state fraction, the beam profiles and the beam energy spectrum of an Au^+ beam have been measured. The test stand consists of a negative gold ion source, a tandem acceleration system, a movable Faraday cup and an energy analyzer.

The energy spectrum of an Au^- beam extracted from the ion source was measured. The energy width was less than 6 eV when Cs vapor was introduced to reduce the surface work function of the gold target. The

dependence of the energy width on the work function was well explained by the theory of the surface production of a negative ion.

The energy shift between the primary negative ion beam and a positive ion beam converted in a gas cell at small gas thickness was measured and found to be about 12 eV. The shift is caused by the two-electron loss process, and amounts to the sum of the electron affinity and the first ionization energy of the projectile.

Energy loss spectra of Au^+ ions produced from Au^- ions by electron stripping in He, Ar, Kr and Xe have been measured in the impact energy range from 24 to 44 keV, under the condition that the charge stripping gas thickness is thin enough so that the two-electron stripping process ($Au^- \rightarrow Au^+$) is dominant and the multiple collision processes are negligible. The full width at half maximum (FWHM) is typically 20 to 80 eV, and it increases with the impact energy. In general, a broader width is observed with a target of a lower mass number.

The energy broadening of the Au^+ beam is caused by elastic and/or inelastic loss processes. The amount of energy loss due to the elastic and the inelastic processes depends upon the impact parameter. The range of the impact parameter, which contributes to the energy loss spectrum is determined by the apparatus geometry (b_{min}) and by the threshold energy for charge stripping (b_{max}). The sum of elastic and inelastic energy losses causes the energy broadening of an Au^+ beam. There is no significant contribution of the elastic energy loss to the energy broadening in the energy range in the present experiment (24 keV ~ 44 keV).

A simple model is proposed using the semi-classical internal energy transfer function of Firsov's and the scattering by the unified potential of Ziegler's. The theoretical prediction of the present model reproduces the energy and mass dependence of the broadening. However, the absolute values of the theoretically predicted width are much smaller than the measured widths. The present model predicts that the energy spectrum in the higher energy region saturates with a FWHM of less than 10 eV, and the target mass dependence disappears.

In the target density region that the multiple collision is not negligible, the energy straggling of a beam is generally explained by the L.S.S. (J. Lindhard, M. Scharff and H. E. Schiøtt) theory. In this theory, the squared energy straggling is given by an integral of the squared energy loss function over the impact parameter from zero to infinity. However, when an energy loss spectrum of a singly-charged component of a beam is measured at forward angle, the energy loss function in a small impact parameter region does not contribute to the straggling. Therefore, a lower limit of integral region is taken into account. It is determined by the minimum impact parameter, b_{min}, or the impact parameter which corresponds to the inelastic energy transfer to produce an Au^{++}. Energy straggling of the present calculation is closer to the measured value than that calculated by the original L.S.S. theory.

The energy broadening of an Au^{+} beam produced by a tandem system can be estimated by the present theoretical prediction. The gas cell of the 3 MV tandem accelerator of LHD will have the same geometry as that of the present test stand. The energy broadening due to the electron stripping can be calculated to be 7 eV, and it does not depend upon the target mass. The calculation of the charge fraction predicts that the optimum gas thickness for Au^{+} beam production is about 6×10^{14} cm^{-2}. Together with the energy broadening due to the multiple collision at this target thickness, the total energy width of the Au^{+} beam produced by a tandem system might be less than several tens eV. The voltage ripple of the tandem power supply is also about several tens eV, therefore, the total energy spread of an Au^{+} beam is about a hundred eV. It will be small enough for a HIBP diagnostics on LHD where the plasma potential is a few keV.

Keywords

plasma sputter type ion source, energy width, energy broadening, negative gold ion beam, positive gold ion beam, tandem acceleration, electron stripping, elastic energy loss process, inelastic energy loss process, energy straggling, heavy ion beam probe

Acknowledgments

I am greatly indebted to Professor Yasuji Hamada for suggesting and supervising this work. I am also indebted to Professor Junji Fujita for helpful suggestions, and Professor Mamiko Sasao for the valuable discussions and the help in experiments.

I must send grateful thank to Professor Motoi Wada in Doshisha University for his valuable comments , suggestions, design the ion source and so on. I thank Professor Hiroyuki Tawara for very helpful comments on atomic processes, and Professor Yoshiharu Mori for comments on ion sources. I thank my colleagues, Masaki Osakabe, Hajime Sakakita, Mitsutaka Isobe, Joong San Koog and Hideharu Kuramoto for discussions and advice. I must acknowledge the financial assistance of Fusion Science Association, and I do greatly thanks for Shinshou Gakusha.

Finally, I would like to thank for many advice given by the scientists in the National Institute for Fusion Science.

Table of Contents

Appendices

§1. Introduction

A Heavy Ion Beam Probe (HIBP) has been used as a reliable method to measure a plasma potential and its fluctuation on a magnetically confined fusion plasma [1]. On the Large Helical Device (LHD) [2], which is a magnetic confinement fusion plasma device under construction in National Institute for Fusion Science, Japan, a singly charged beam of mass 200 amu with the energy of 6 MeV is required in order to explore into a large and strong magnetic field region of 3 T [3]. The primary beam will be injected from a bottom port. The secondary beam will be analyzed after escaping from a radial port that is toroidally displaced by a half section (Fig.1).

For the production of the particle beam of this energy region, two different methods can be considered. One is a 6 MV single stage acceleration of a positive ion beam, and the other is a 3 MV tandem acceleration starting with a negative ion beam. Figure 2-(a) shows a 6 MV single stage system and Fig. 2-(b) shows a 3 MV tandem acceleration system. In the case of the LHD project, the size of the 6 MV tank is almost intolerable. The maintenance of single stage acceleration system is another problem. The ion source, which is installed on the high voltage terminal, should be changed frequently because the life time of a thermionic-type heavy metal source is not long. On the other hand, a negative ion source is usually set on the almost ground potential level in the tandem acceleration system. The maintenance of a plasma-sputter-type negative ion source is simple; only the change of the target material or Cs for lowering the target work function is required. In general, a tandem acceleration system is compact in size and easy to maintain.

The stability of a high voltage power supply system is also important. A small energy spread of the primary beam is required for accurate measurement of the plasma potential. The higher the voltage is, the worse

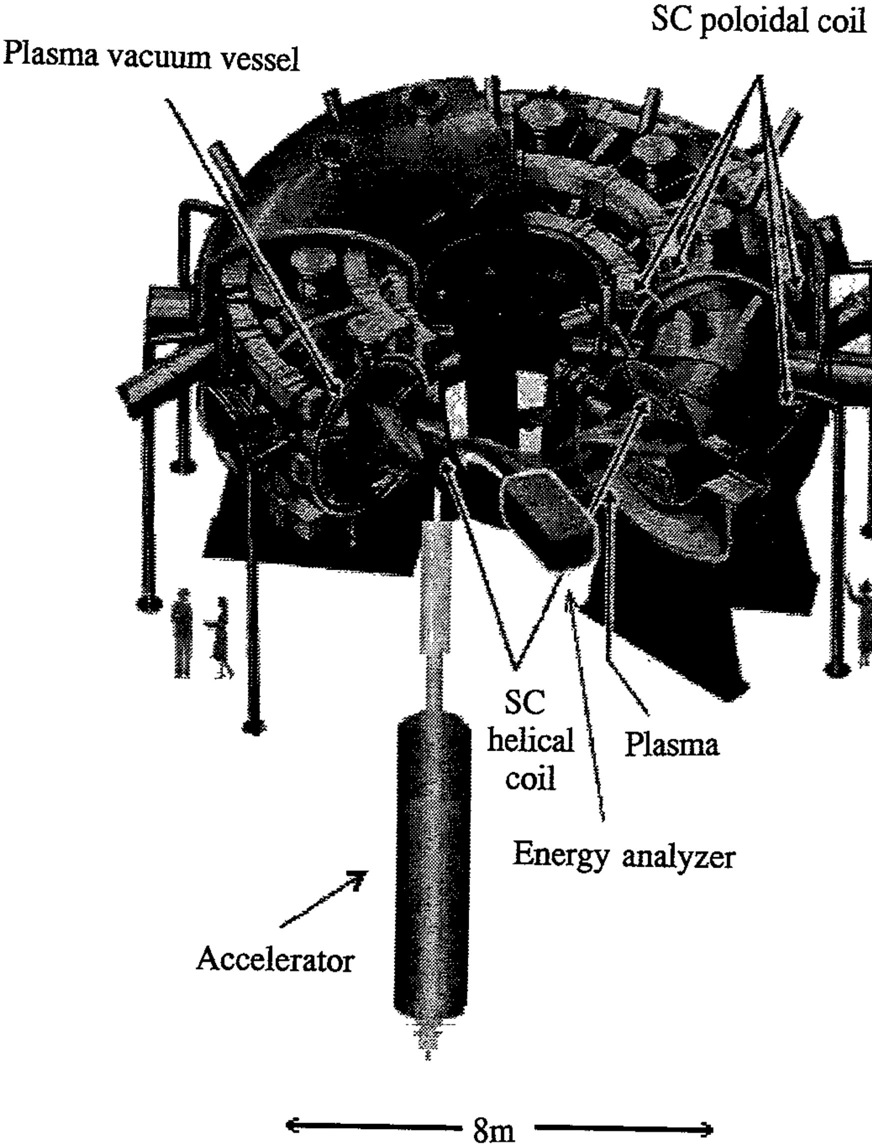

Fig.1. A schematic view of a Heavy Ion Beam Probe (HIBP) diagnostic system on the Large Helical Device (LHD).

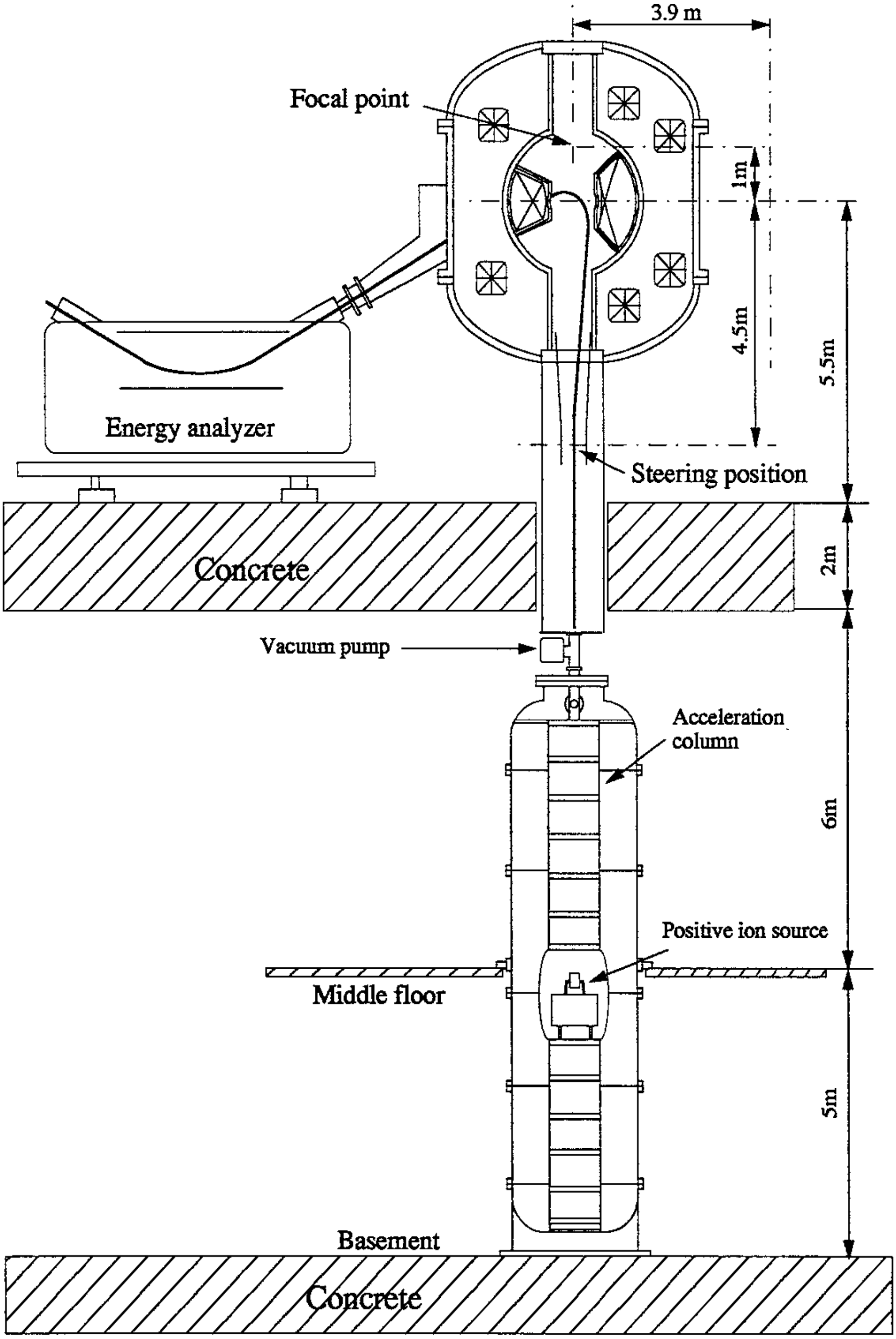

Fig. 2-(a). A schematic diagram of the single acceleration system.

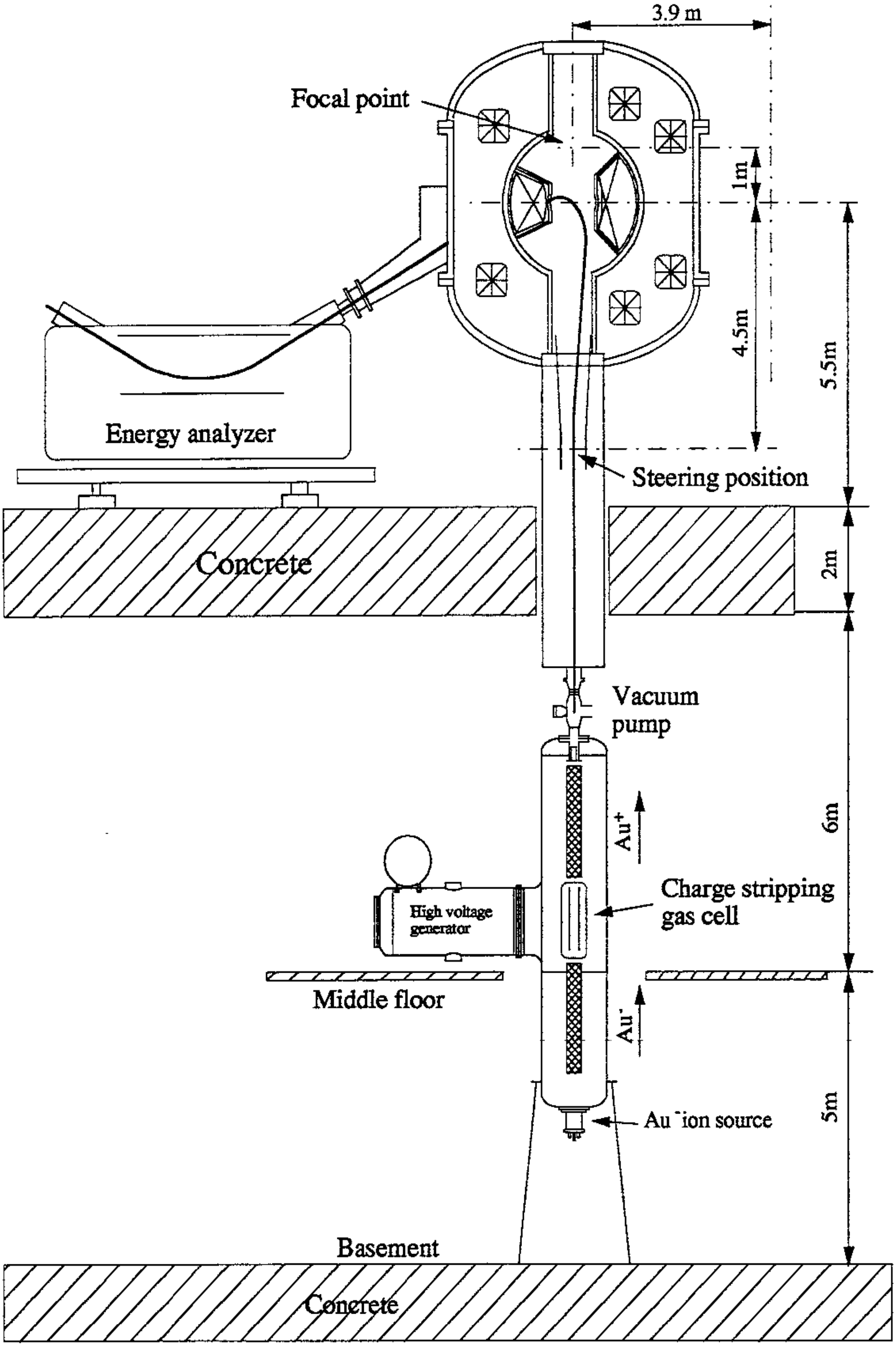

Fig. 2-(b). A schematic diagram of the tandem acceleration system.

its stability is. Although remarkable progress on a rapid feedback system using a charge sprayed high voltage terminal has been developed, more than 200 V fluctuation is anticipated at 6 MV. On a tandem system of 3 MV terminal voltage, an electrostatic high voltage system with a ripple ratio less than 10^{-5} can be realized. The comparison of the two systems is outlined in Fig. 3.

Taking these points into account, a tandem acceleration system is more attractive, provided that enough negative ion current with a small energy spread can be extracted from the ion source, and the energy broadening of the beam can be minimized in the process of charge exchange.

A negative ion source of high-energy-ion-beam-sputter-type has a large energy spread, a large beam emittance and a small beam current. Hence it is not considered to be useful for the application to HIBP. A plasma-sputter-type negative ion source can produce a beam of heavy elements with a current of more than several hundred micro amperes [4,5]. This type of ion source produces negative ions with a sputtering process using low energy plasma ions, and the energy spread of the produced negative ions can be small.

On LHD, a singly charged positive ion beam of gold (Au^+) produced from an Au^- beam with a 3 MV tandem acceleration system will be used to measure plasma potentials. Here, the energy spread of output beam must be small enough to measure a plasma potential as small as a few keV. If the mechanism of the energy broadening is understood, we will be able to design the stripping cell and optimize it for the potential measurement.

Thus, it is necessary to study the mechanism of the energy broadening, energy shift of the beam in the cell and the stripping efficiency to a singly charged positive ion beam. Especially the energy spectra of positive ions produced from negative ions have recently attracted attentions

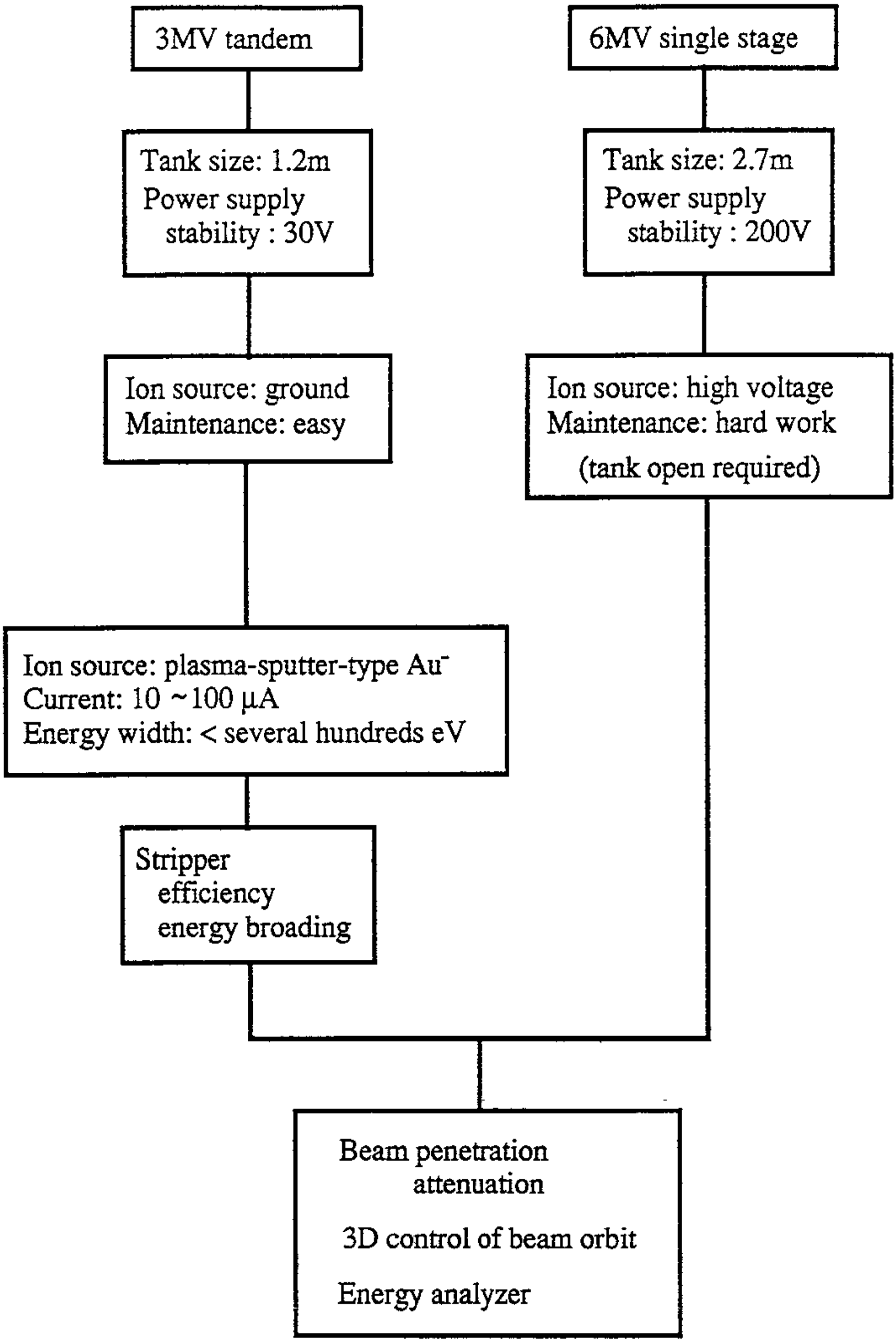

Fig. 3. A comparison between single stage and tandem acceleration configurations for Heavy Ion Beam Probe diagnostic system.

of researchers in accelerator physics. Here a small energy spread is required on the positive beam generated in the charge exchange gas cell on the high voltage terminal [6].

As one of important research subjects on the atomic physics, there have been many studies done on the angular distribution and the energy spectrum of the scattered secondary particles in heavy ion collisions at a small impact parameters, and various information on the intrinsic structures of atoms has been obtained [7]. The change of energy spectra of the incident ions resulting from forward angle atomic collisions at a large impact parameter should also be affected by the effective potentials between atoms, and/or atomic excitations.

In the present work, a tandem acceleration test stand has been constructed in order to study these problems. An Au^- beam from a plasma-sputter-type negative ion source is injected into the charge exchange gas cell, and the charge state fraction, the beam profiles and the beam energy spectrum of Au^+ are measured.

Information on the energy broadening can be obtained by the measurement of energy spectrum. When the charge stripping gas is thin and the multiple collision processes are negligible, the energy transfer function of double charge stripping process ($Au^- \rightarrow Au^+$) is obtained. In the region where the multiple collision is not negligible, the dependence of the broadening of an Au^+ beam upon the gas thickness is also measured.

The mechanism of energy broadening resulting from the stripping process has been theoretically studied considering the elastic potential scattering process and the semi-classical inelastic process. This model gives the energy broadening for thin gas target and the electron stripping cross sections. Then, the energy straggling, which is the effect of multiple collisions, is studied on the same bases of collision theory. The theoretical prediction has been compared with experimental results.

Finally, using these results such as the energy broadening, the energy straggling and the cross sections, the energy width and the charge fraction of the beam are estimated on 3 MV tandem acceleration system for HIBP on LHD.

In the following section, the experimental setup is shown. The theoretical model to treat the energy broadening due to the electron stripping process and the cross section are described in the section 3. In the section 4, the experimental results are presented and compared with calculations using the model, and the charge fraction and energy width on 3 MV accelerator are considered. The conclusion is given in the section 5.

§2. Tandem Acceleration Test Stand

Figure 4 shows a schematic view of the tandem acceleration test stand, which consists of a plasma-sputter-type gold negative ion source, a tandem acceleration system, an energy analyzer and movable Faraday cup.

2-1 Au^- Ion Source

A. *Structure and Operational Principle of Plasma-Sputter-Type Au - Ion Source*

A compact plasma-sputter-type Au^- source was fabricated to study its characteristics for the application to HIBP. As shown in Fig. 5, it consists of a 80 mm diameter 90 mm long cylindrical stainless steel plasma container, a gold disk target of 18 mm diameter brazed on a copper rod, a pair of tungsten filaments of 0.35 mm diameter, an extraction electrode, an einzel lens, a cesium oven, and Sm-Co magnets for plasma confinement. A typical filament current was about 16~20 A, the discharge voltage and the current were 40 V and 50~100 mA. An argon gas was introduced as the discharge gas.

The gold target surface, which was biased at a negative voltage (V_T) with respect to the discharge chamber, was sputtered by plasma ions such as Ar^+ or Cs^+, and produced a flux of Au^- ions directed to the extraction hole. The target voltage could be controlled in the range from 0 to 400 V, which was operated typically 350 V. In order to reduce the surface work function of the gold target, and hence, to increase the Au^- production, Cs vapor was introduced from an external Cs oven. The Cs quantity introduced into the discharge chamber was controlled by the oven temperature, operated in the

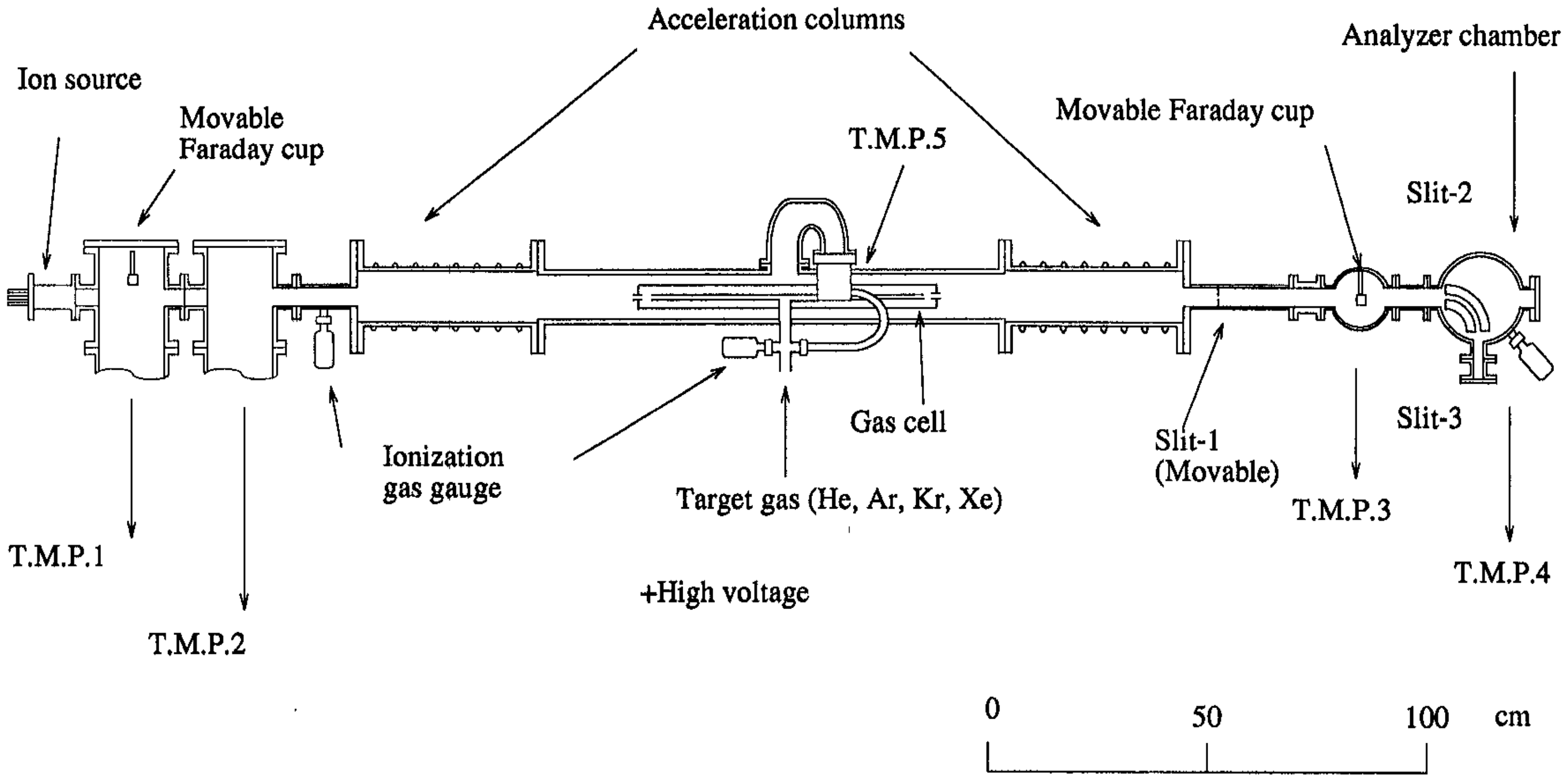

Fig. 4. A schematic view of the experimental set up.

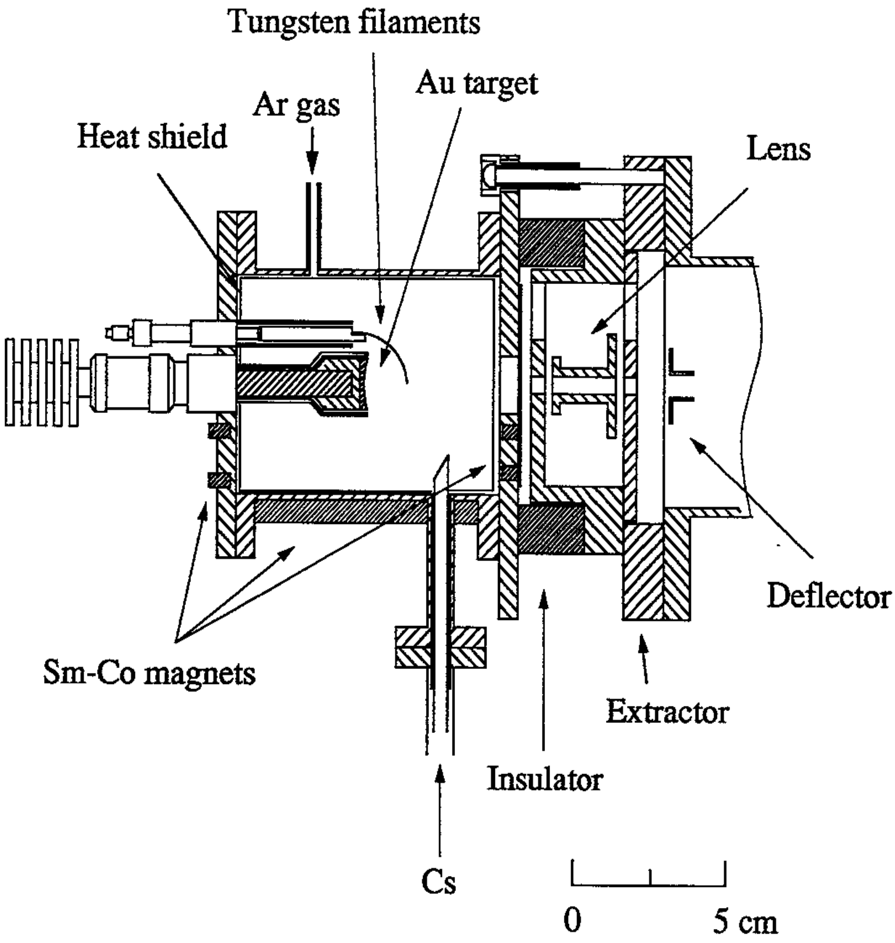

Fig. 5. A schematic view of the plasma-sputter-type Au⁻ ion source.

range of about 180~250 °C. For enhancing the recycling of Cs vapor in the ion source, a heat shield was placed in the discharge chamber.

The negative ions produced on the target were accelerated in the plasma sheath region and were extracted by the bias voltage between the discharge chamber and the extraction electrode of ground potential. Extraction of electrons in the plasma were suppressed by negative bias voltage on the front end plate of the discharge chamber, and the magnetic field produced by Sm-Co magnets around the extraction hole.

It is desirable to reject the impurity ions before injection to the tandem accelerator by the magnetic and/or the electric field, because the impurity ions such as H^- and O^- are often extracted from this source.

B. *Au⁻ Energy Spread*

The energy spectrum of negative ions produced from this type of source has been extensively studied [8,9]. It has an average energy of the target bias voltage (typically 300~400 V) plus a few eV, and its full width at half maximum (FWHM) is less than several eV. This is confirmed in the present experiment.

The energy distribution of Au^- ions from a plasma-sputter-type source can be determined by the energy distribution of particles ejected by the sputtering, $f(E_2,\theta)$, and the negative ion production probability, $P^-(E_2,\theta)$, as the following,

$$I^-(E) = \int f(E_2,\theta)\cdot P^-(E_2,\theta)\mathrm{d}\Omega \qquad (1)$$

$$E = eV_\mathrm{T} + E_2\cos^2\theta \ ,$$

where E_2 and θ are the energy of the ejected particle and the angle from the normal to the surface, respectively. The negative ion production probability, P^-, depends upon the surface work function, ϕ, the electron affinity of the ejected particle, ε_A, and its escaping velocity normal to the surface, $v_n = \sqrt{2E_2 / M} \cos\theta$. In low energy limit, there are approximate formulae [10,11].

$$P^-(E_2,\theta) = \frac{2}{\pi}\exp\left\{-c\frac{(\phi-\varepsilon_A)}{v_n}\right\} \quad \text{when } \phi > \varepsilon_A \qquad (2)$$

$$P^-(E_2,\theta) = 1-\frac{2}{\pi}\exp\left\{c\frac{(\phi-\varepsilon_A)}{v_n}\right\} \quad \text{when } \phi < \varepsilon_A , \qquad (3)$$

where c is constant. Figure 6 shows some examples of calculated spectrum for different work functions. Here the parameter α represents $c\ (\phi - \varepsilon_A)$, and the Thompson formula is used as the energy spectrum of the ejected particles [12].

The measured energy width of the Au^- beam from the source of this type is shown in Fig. 7 as a function of the target voltage. The instrumental width was much smaller than the measured spectrum width in this beam energy range. The width shows a weak energy dependence, and those for a high work function surface without Cs(circles) were a little larger than those for a low work function surface with Cs(triangles), as expected from the theory. However, measured minimum energy widths are much smaller than the value of the theoretical prediction of 7.4 eV. Present values of the energy width, W_{org}, are in the range from 4 to 5 eV, and smaller than those of previous experimental works [8], because of the better resolution of the energy analyzer.

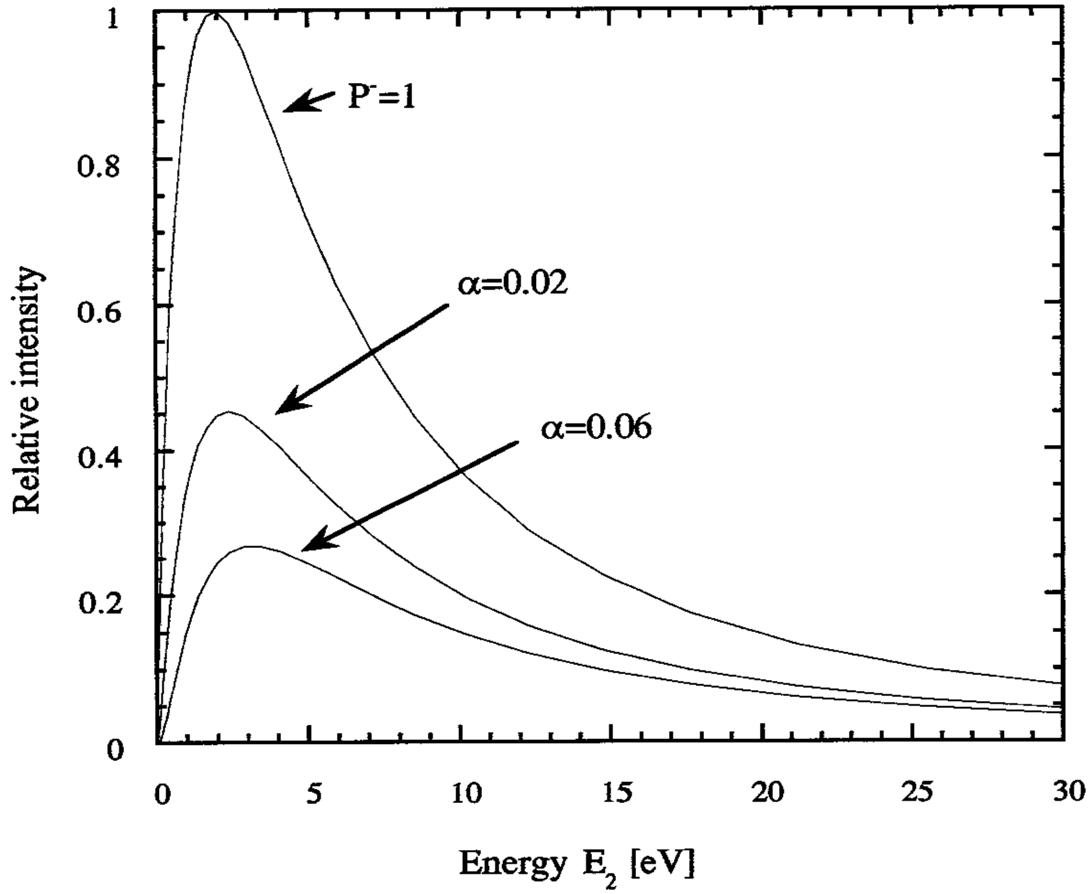

Fig. 6. Examples of calculated energy spectra of surface-produced Au⁻ beam for different negative ion production probability, P^-. In lower two cases $P^-=2/\pi\exp(-\alpha/v_n)$, where $\alpha=c(\phi-\varepsilon_A)$.

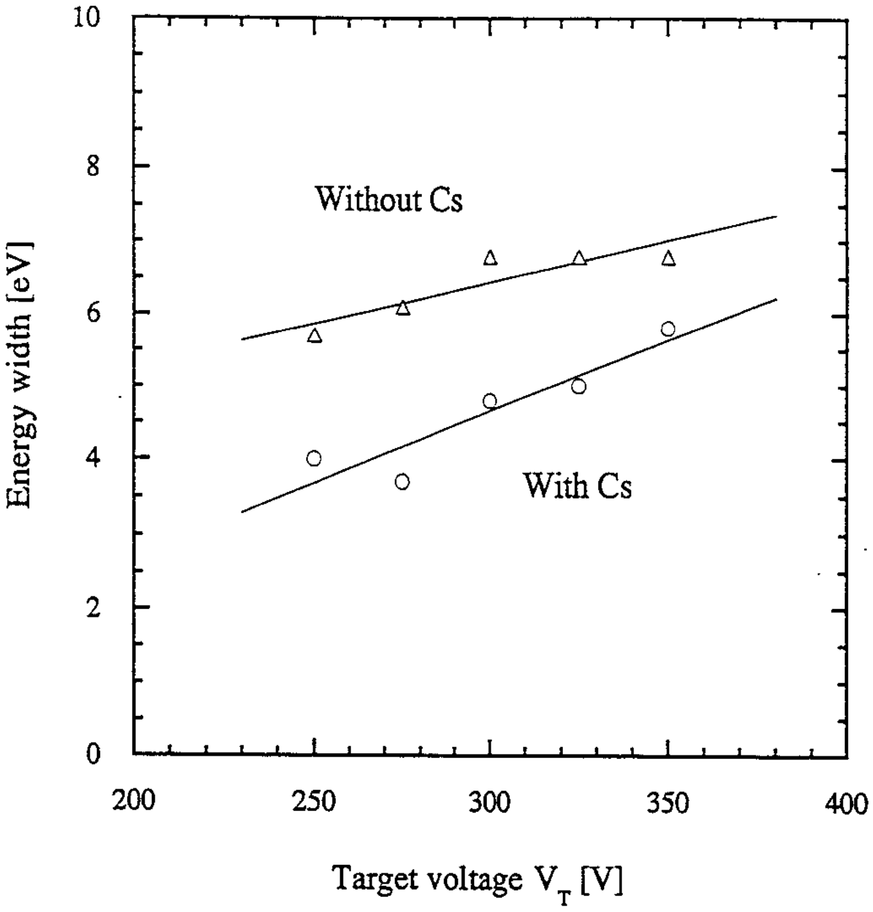

Fig. 7. The measured energy width of the Au^- beam plotted as a function of the target voltage.

C. *Operating System*

Because the ion source is operated on the high terminal as shown in Fig. 8, its power supplies and instruments to measure the operation parameters should be shielded and be operated by a personal computer through an optical fiber for insulation. This system can control voltages of the ion source such as the filament, the discharge, the target voltage and two Cs oven heater powers by using GP-IB controller units. The parameters such as the discharge current, the target current, the Cs oven and the valve temperature are monitored with an interval of one minute by SYSTEM DMM/SCANNER MODEL 199 (KEITHLEY). In Fig. 9, the block diagram of the operation program and an example of the control panel are shown.

2-2 Acceleration System

Figure 10 shows a schematic diagram of the tandem acceleration system. The negative ions from the ion source are preaccelerated with an typical energy of 4 keV, and injected into the accelerator column. The stability of the power supply for the preacceleration and that for the tandem acceleration are measured by a high voltage probe, and both are around 1×10^{-4}.

The charge stripping gas cell of a 14 mm diameter and 700 mm length is installed on the high voltage terminal. The cell is contained in a 900 mm length cylinder with an entrance and exit cylindrical tubes of the 14 mm diameter. An inert gas, such as He, Ar, Kr or Xe is introduced into the cell. The gas pressure is directly measured by an ionization gauge near the cell. The reading of the gauge has been calibrated for various gases prior to the experiments.

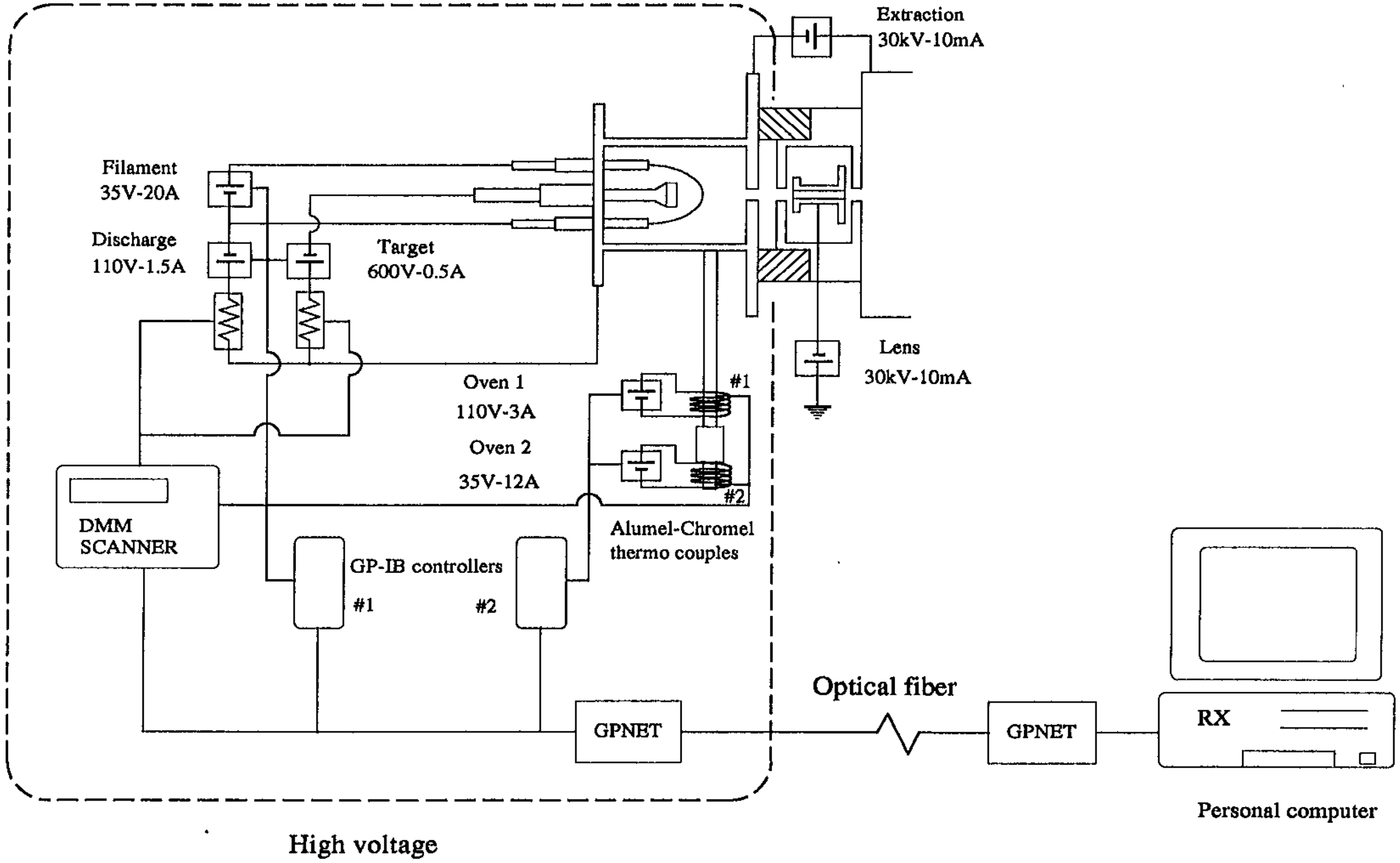

Fig. 8. A block diagram of the ion source operation system.

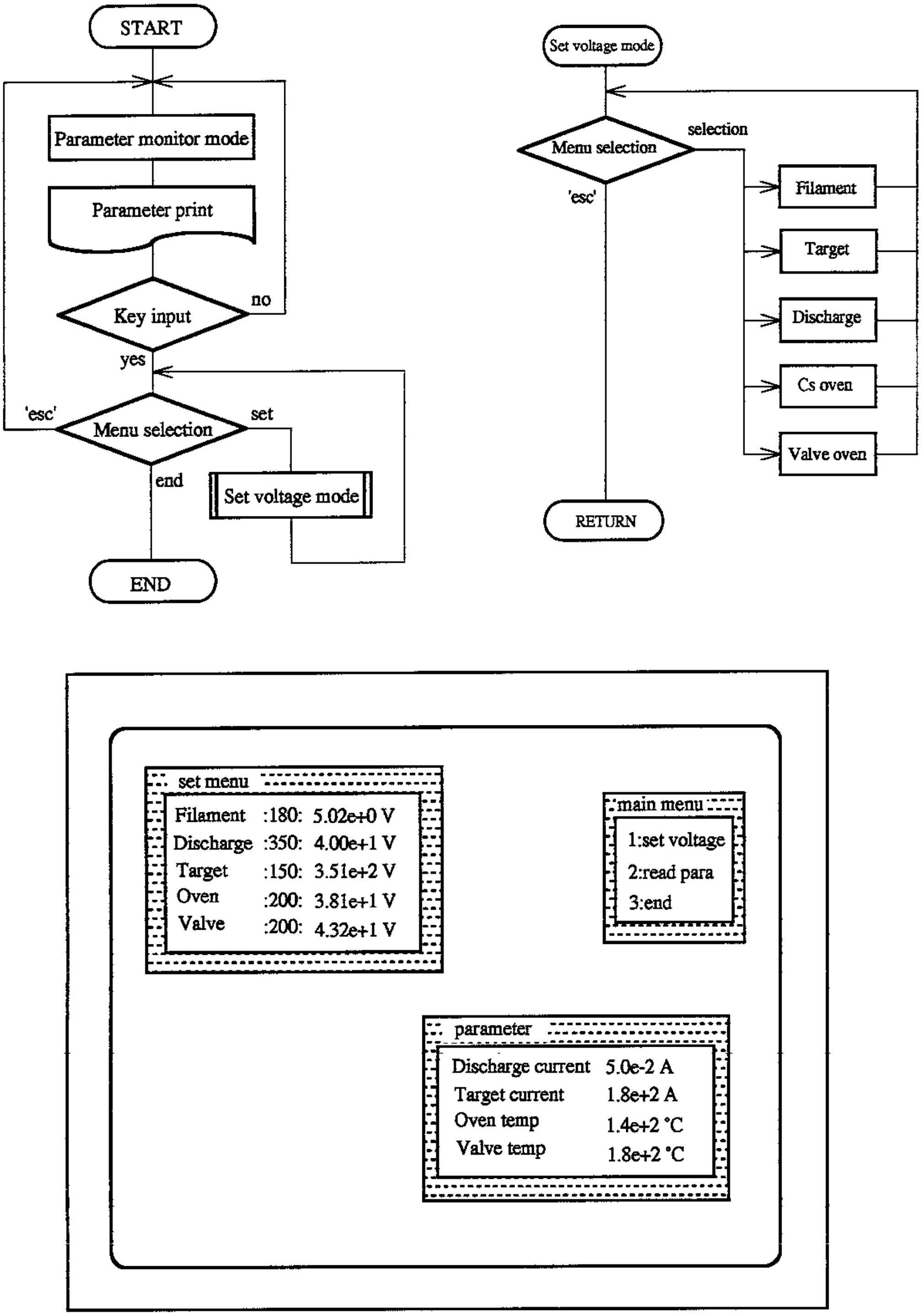

```
set menu
Filament   :180:  5.02e+0 V
Discharge  :350:  4.00e+1 V
Target     :150:  3.51e+2 V
Oven       :200:  3.81e+1 V
Valve      :200:  4.32e+1 V

main menu
1:set voltage
2:read para
3:end

parameter
Discharge current  5.0e-2 A
Target current     1.8e+2 A
Oven temp          1.4e+2 °C
Valve temp         1.8e+2 °C
```

Fig. 9. A block diagram of the operation program of ion source and an example of control panel.

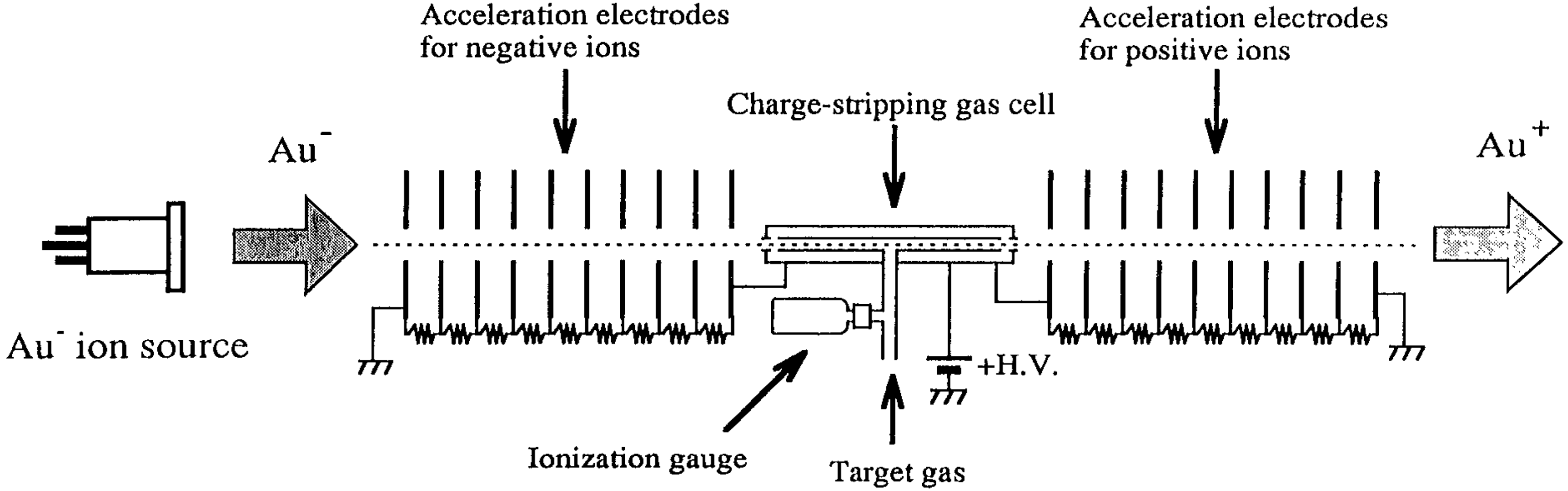

Fig. 10. A schematic diagram of the tandem acceleration system.

The target thickness, nl, is defined by

$$nl = \int n(x)dx = 3.5 \times 10^{16} \int p(x)\mathrm{d}x \ , \qquad (4)$$

where

x : the position in a gas cell

$n(x)$: the particle density in cm^{-3} at position x

$p(x)$: the gas pressure in Torr at position x .

The gas pressure, $p(x)$, in the cell and its vicinity can be roughly estimated by a calculation of conductance, and the target thickness is obtained by the following relation,

$$nl = 3.5 \times 10^{16} \cdot \frac{p_{\mathrm{m}} \cdot L_{\mathrm{g}}}{1.2} \qquad (5)$$

where

p_{m} [Torr] : gas pressure measured by the gauge

$L_{\mathrm{g}} = 90$ [cm] : the geometrical cell length.

The detail is discussed in appendix A.

The thickness is also estimated by measuring the attenuation cross sections of an H^- beam in an Ar gas target at 4, 5 and 7 keV, as is shown in Fig. 11. They are compared with those of the empirical fitting curve [13], as is shown in Fig. 12. Then, the target thickness, nl, is obtained by

$$nl = 3.5 \times 10^{16} \cdot \frac{p_{\mathrm{m}} \cdot L_{\mathrm{g}}}{1.8} \quad [\mathrm{cm}^{-2}] \ . \qquad (6)$$

In the present experiment, the effective target thickness calculated by Eq.(6) is used. Considering the accuracy of the conductance calculation and

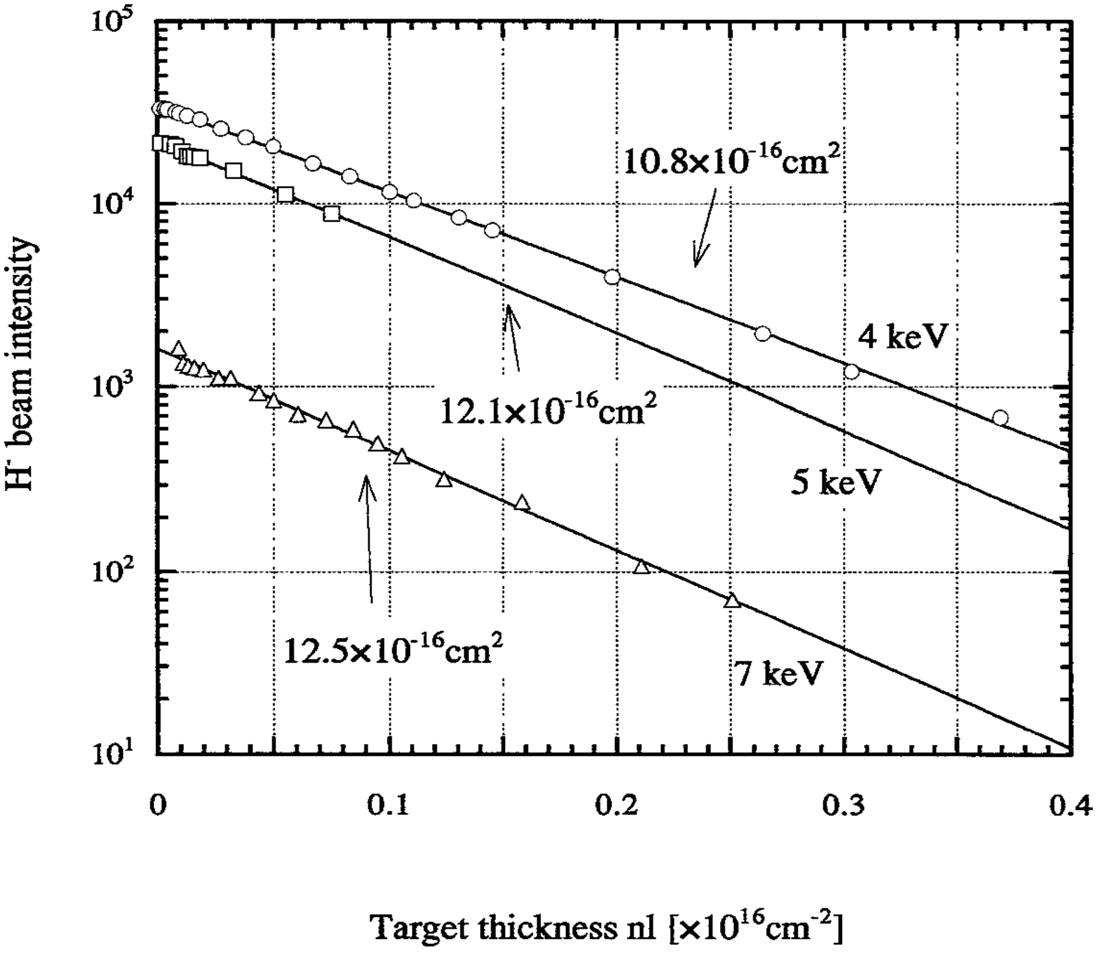

Fig. 11. Attenuation characteristics of an H^- beam penetrating into an Ar target and the cross sections dedicated from the characteristics.

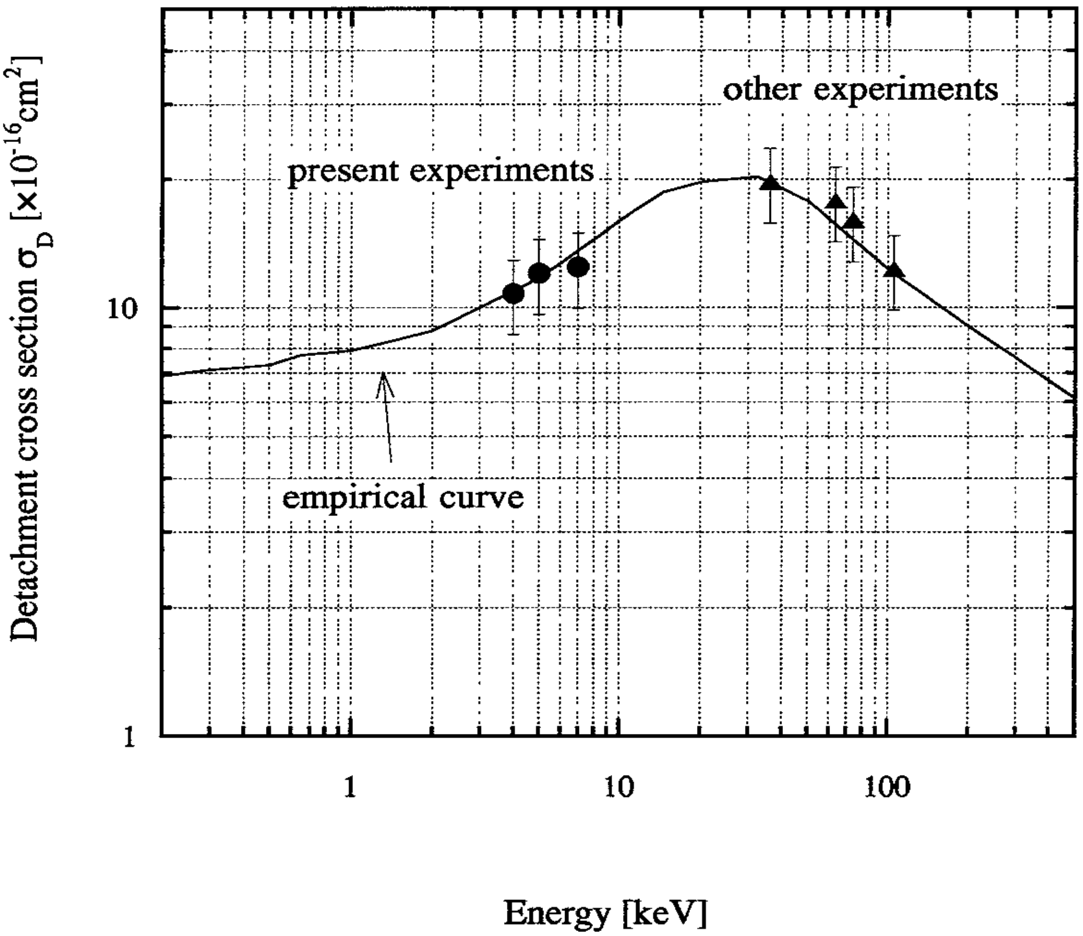

Fig. 12. Electron detachment cross sections of H$^-$ beam in Ar target in comparison with the empirical fitting curve.

that of the empirical fitting curve, both estimations result in the same values within their margins of uncertainty.

2-3 Energy Analysis System

A. *Structure of Energy Analyzer*

The positive ions produced in the cell are accelerated again to the ground potential and their energy spectra are measured by a 90 degree cylindrical electro-static analyzer (see Fig. 13). Two slits are set; a 0.015 mm slit at the entrance and a 0.03 mm slit at the exit.

The two electrodes are biased with the same voltages of opposite polarity. The first power supply generates a fixed voltage, and the second power supply adds variable voltage of ± 100 V. It is desirable to sweep out the impurity ions in the beam before injection to the tandem accelerator. In this experiments, a pair of samarium-cobalt magnets are simply installed on the analyzer in order to keep alignment of the beam trajectory. Because the broadening effect by the magnetic field separation has been confirmed to be negligibly small by comparing the Au peak's with the magnetic field and that without it, when the impurity peaks are not seen. The spectra with (a) and without (b) the magnetic field are shown in Fig. 14. The spectrum with the magnetic field is separated into different atomic components by the magnetic field.

A slit of 0.4 mm at the exit of the accelerator column restricts the beam entrance angle and improves the resolution of the analyzer. The effect of the slit at the tandem acceleration exit is shown in Fig. 15. Practically, the resolution does not change much, and the slit width of 0.4

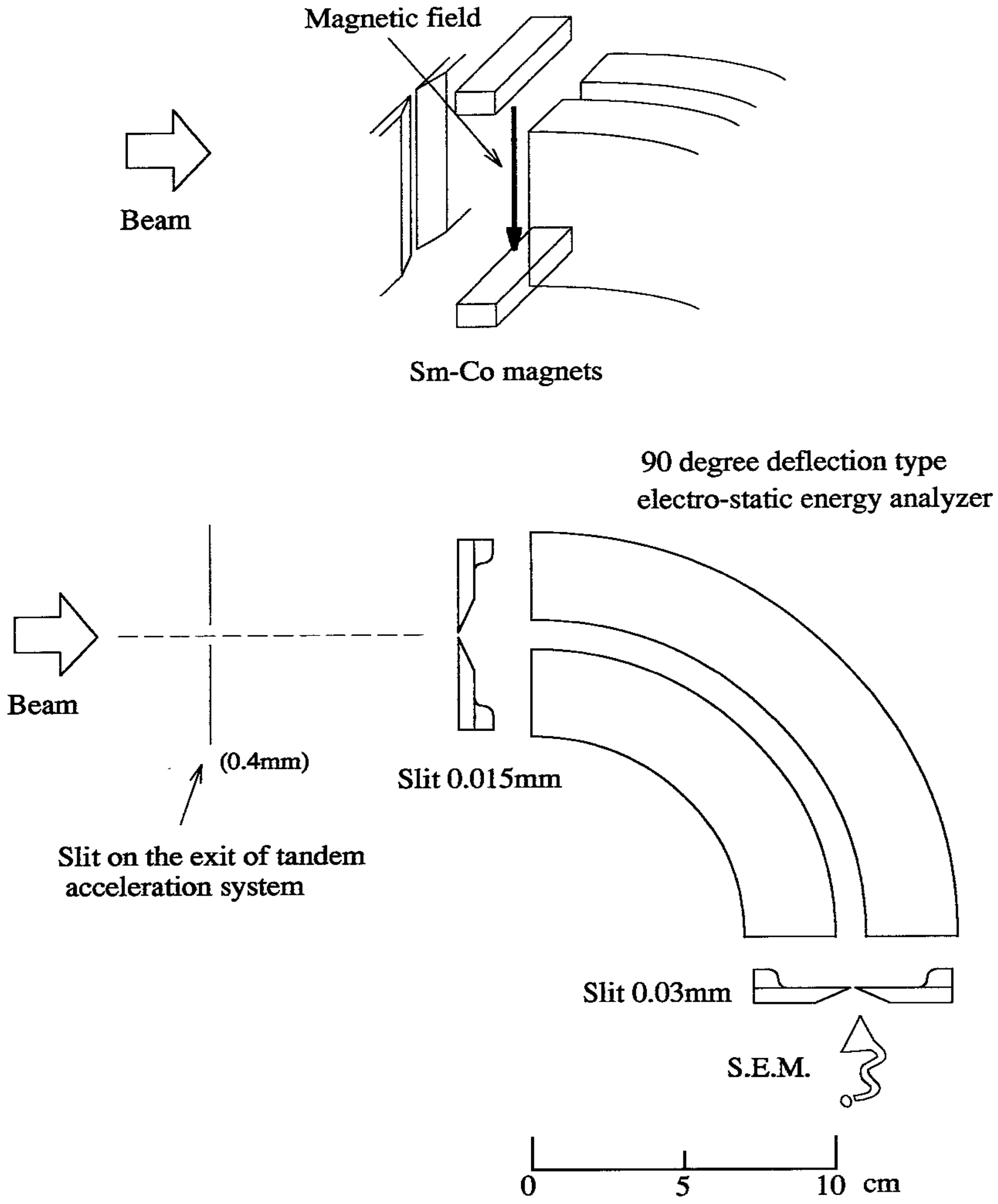

Fig. 13. A schematic view of beam energy analyzing system. The beam spectrum is measured by a 90 degree deflection type electro-static energy analyzer and the mass is separated by a magnetic field.

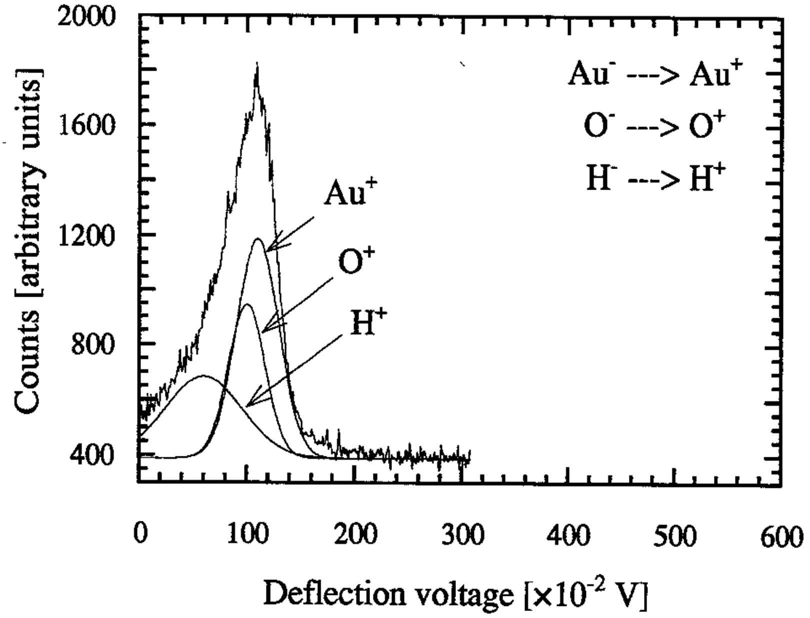

(a) without magnetic field in the drift space

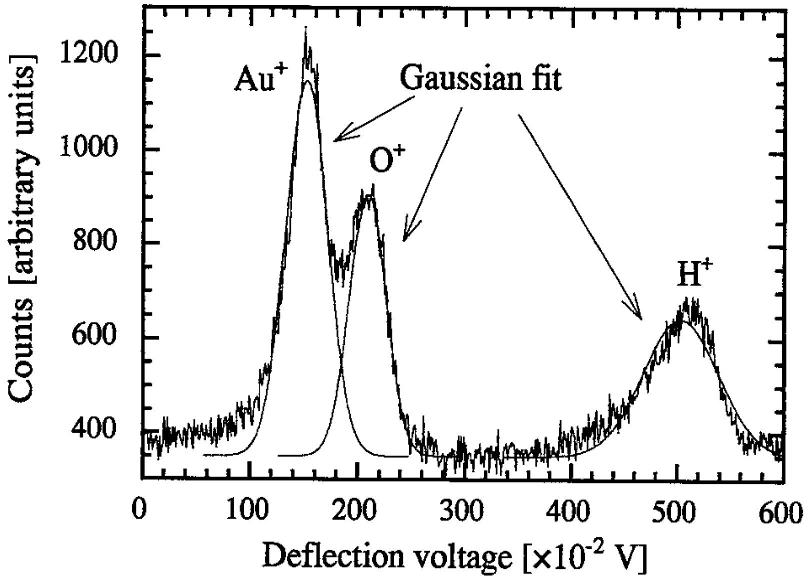

(b) with magnetic field in the drift space

Fig. 14. The effect of magnetic field in the drift space of an analyzer. The energy spectrum (a) is not mass-separated as the magnets are removed, and that in (b) is separated for different mass numbers by the magnetic field.

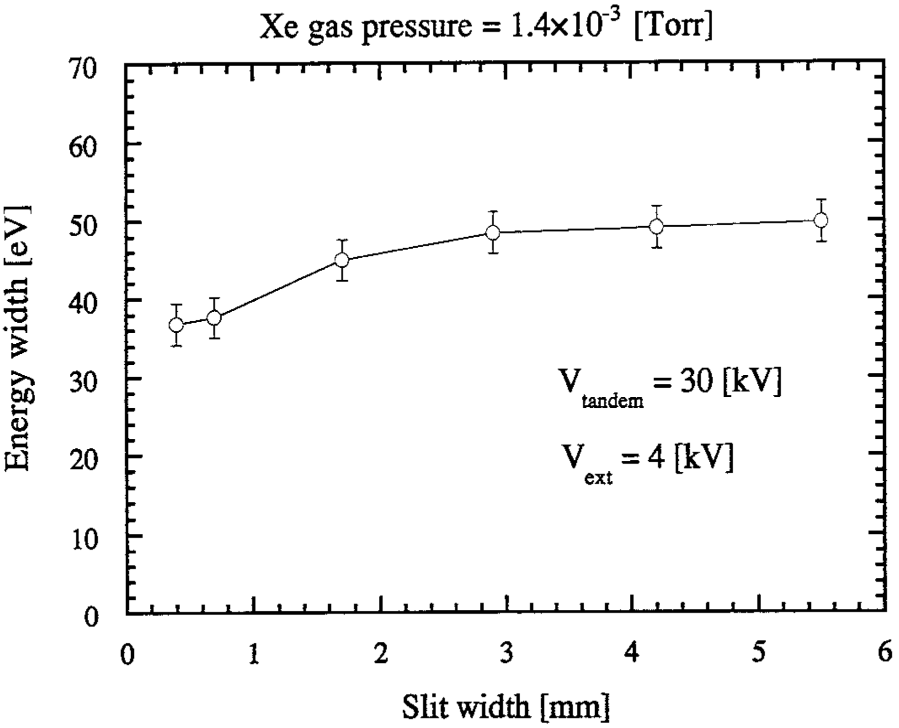

Fig. 15. The effect of the slit placed at the tandem acceleration exit.

mm seems to be sufficiently small to eliminate the deterioration due to the entrance angle.

An energy spectrum is obtained by sweeping the positive and negative bias voltages on the electrodes in every 0.1 V step with a personal computer, and counting the number of pulses from the secondary electron multiplier that detects beam particles passing through the exit slit.

B. *The Resolution of Energy Analyzer*

In this thesis, the energy width is defined by a full width at half maximum of the energy spectrum. The measured value of the energy width includes an experimental width caused by the resolution of energy analyzer and that caused by the ripple of the power supplies. The resolution of an ideal cylindrical energy analyzer, R_{an}, can be expressed by the following relation,

$$R_{\mathrm{an}} = \frac{\Delta E}{E} = \frac{w}{2r} \quad , \tag{7}$$

E : the particle energy
w : the slit width
r : the particle orbit radius.

In the present case, the slit width is 0.02 mm, and the particle orbit radius is 105 mm, then the resolution of the analyzer, R_{an}, is about 10^{-4}. The catalog values of the ripple of the power supplies on two electrodes, $\Delta V/V$, are less than 10^{-4}. Then, the experimental resolution is expected to be in the order of 10^{-4}.

The energy width of an Ar+ ion beam has been measured as a function of the beam energy in order to calibrate the energy resolution of the analyzer as shown in Fig. 16. Because these ions are directly extracted from the plasma volume of the source, the energy spread of the beam is expected to be around the plasma temperature that is less than a few eV. By fitting the experimental energy width with a following equation,

$$W_{\mathrm{exp}}(E) = \sqrt{W_{\mathrm{org,Ar}}{}^2 + W_{\mathrm{an}}{}^2} = \sqrt{W_{\mathrm{org,Ar}}{}^2 + (R_{\mathrm{an}} \cdot E)^2} \qquad (8)$$

where

W_{exp} : the measured energy width

$W_{\mathrm{org,Ar}}$: the original energy width of the Ar+ beam from the volume production source

W_{an} : the energy broadening due to the analyzer

R_{an} : the energy resolution of the analyzer,

the resolution of the analyzer, R_{an}, is experimentally determined to be

$$R_{\mathrm{an}} = (3.9 \pm 0.4) \times 10^{-4} \ .$$

C. *Operating System*

Figure 17 shows the operating system of the energy analyzer. Each electrode of the analyzer is biased by two voltage power supplies connected in series. One voltage output is variable and is swept in every 0.1 V by a personal computer. A Secondary Electron Multiplier (S.E.M.) is used for counting the beam particles passing through the exit slit. The front face of S.E.M. is at the ground potential, the electron exit side is biased at +2.3 kV and a signal detector made of silver is biased at +2.7 kV. The pulse

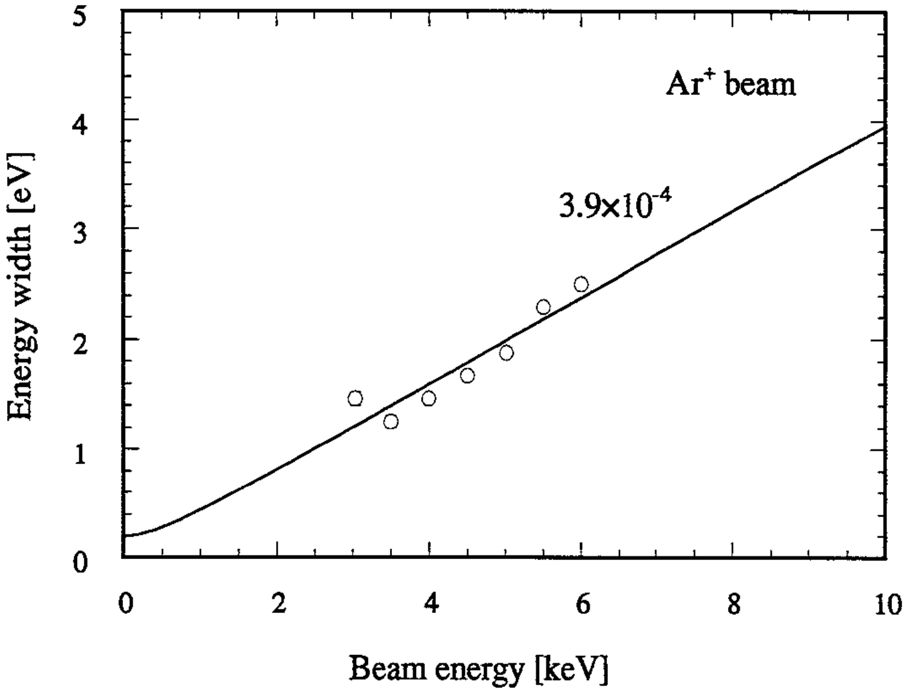

Fig. 16. The energy resolution of the analyzer measured by Ar+ beams.

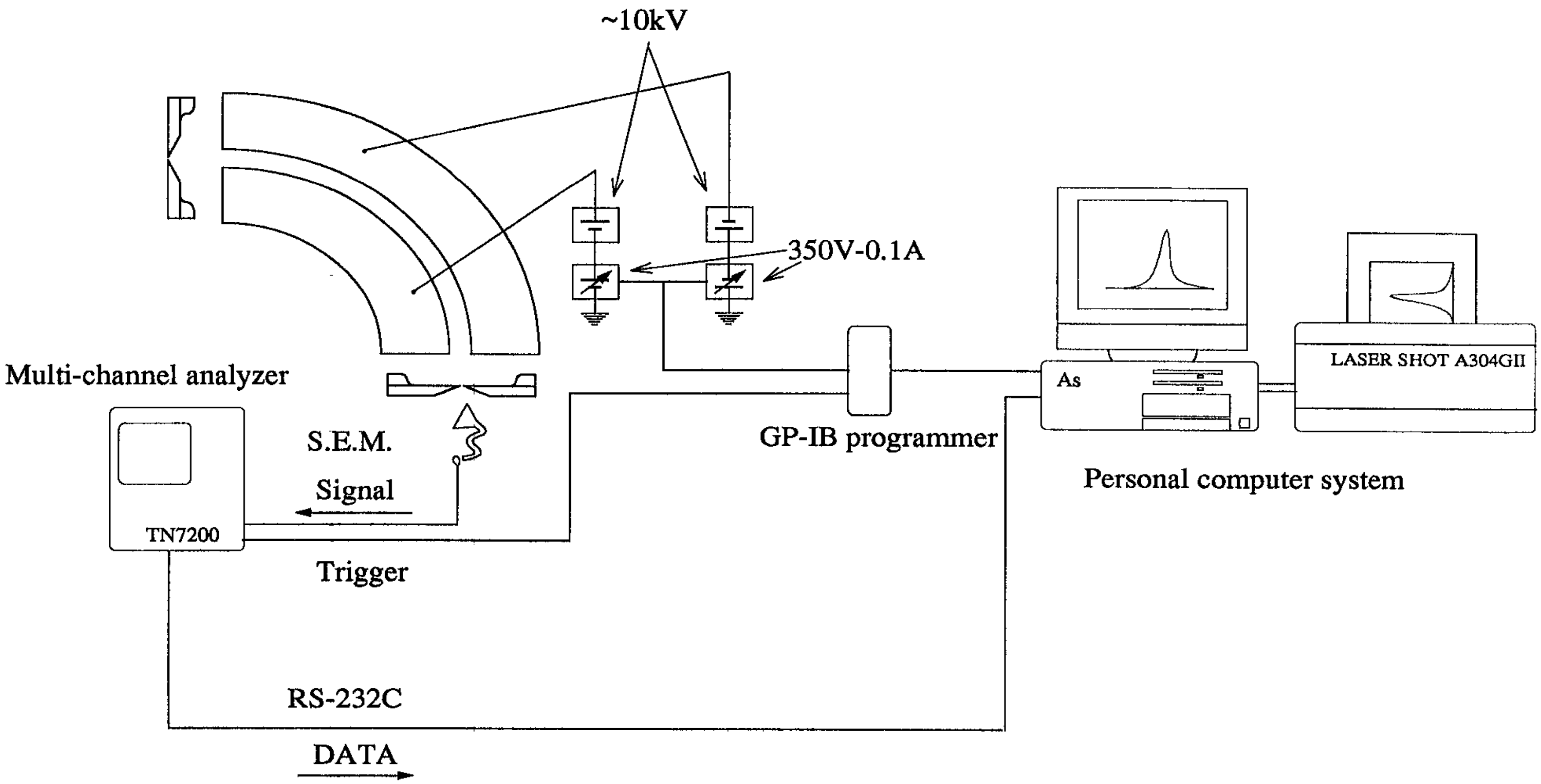

Fig. 17. A block diagram of the control system for the energy analyzer.

counting is taken by a multi-channel scaler TN7200 (Tracor Northern). In Fig. 18, the block diagram of the operation program and an example of the control panel are shown.

2-4 Beam Current and Profile Measurement System

The beam current is measured by Faraday cup at 50 cm away from the exit of the tandem acceleration, which can travel perpendicular to the beam line as is shown in Fig. 19. This system can measure the beam profile and the current. By applying the magnetic field at a place of 25 cm upper stream of the beam line from the cup, impurity components of the beam can be swept out. The beam current is measured by programmable electrometer, (KEITHLEY Model 617), which can measure down to 0.01 nA.

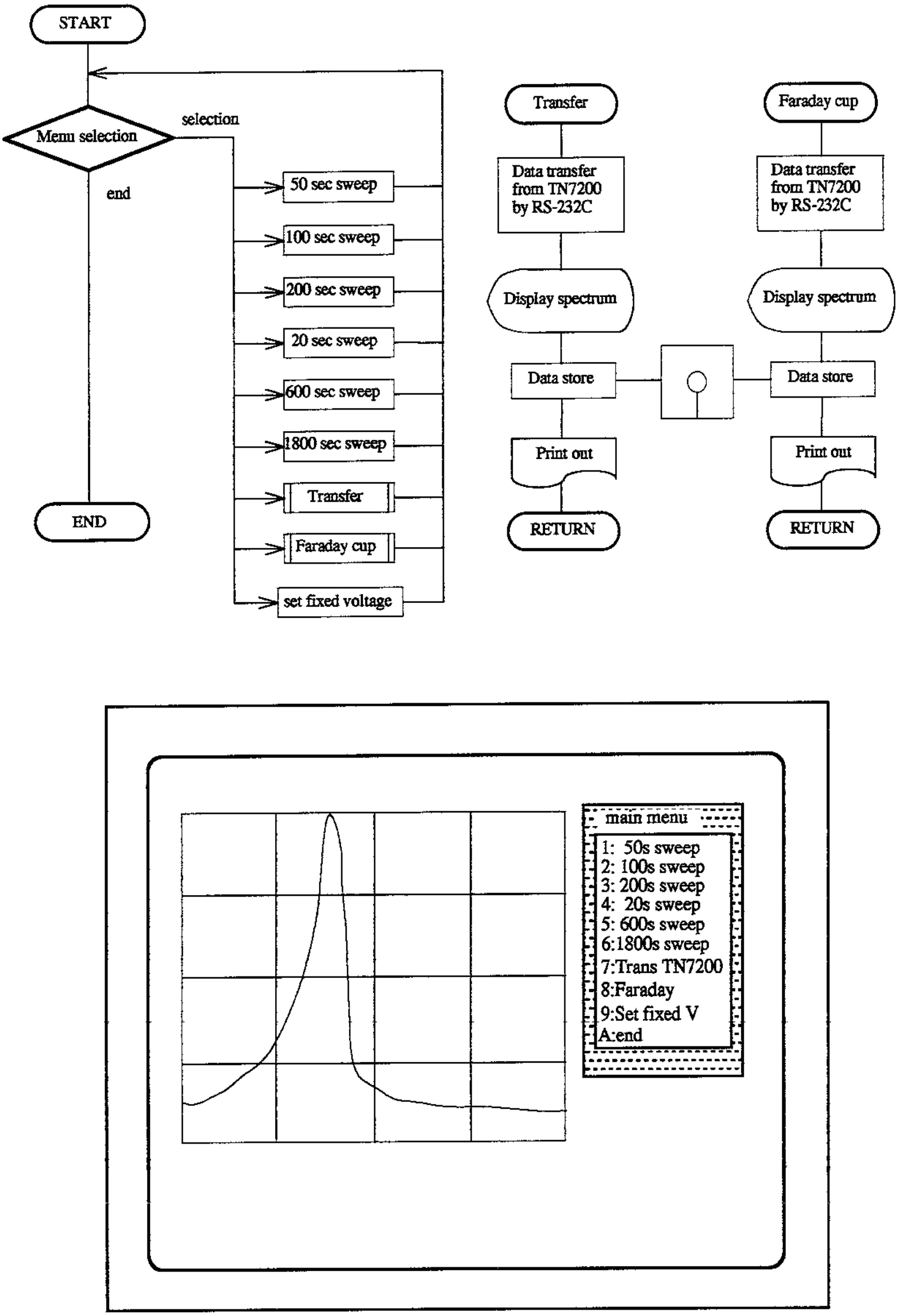

Fig. 18. A block diagram of the diagnostic operation system and an example of the control panel.

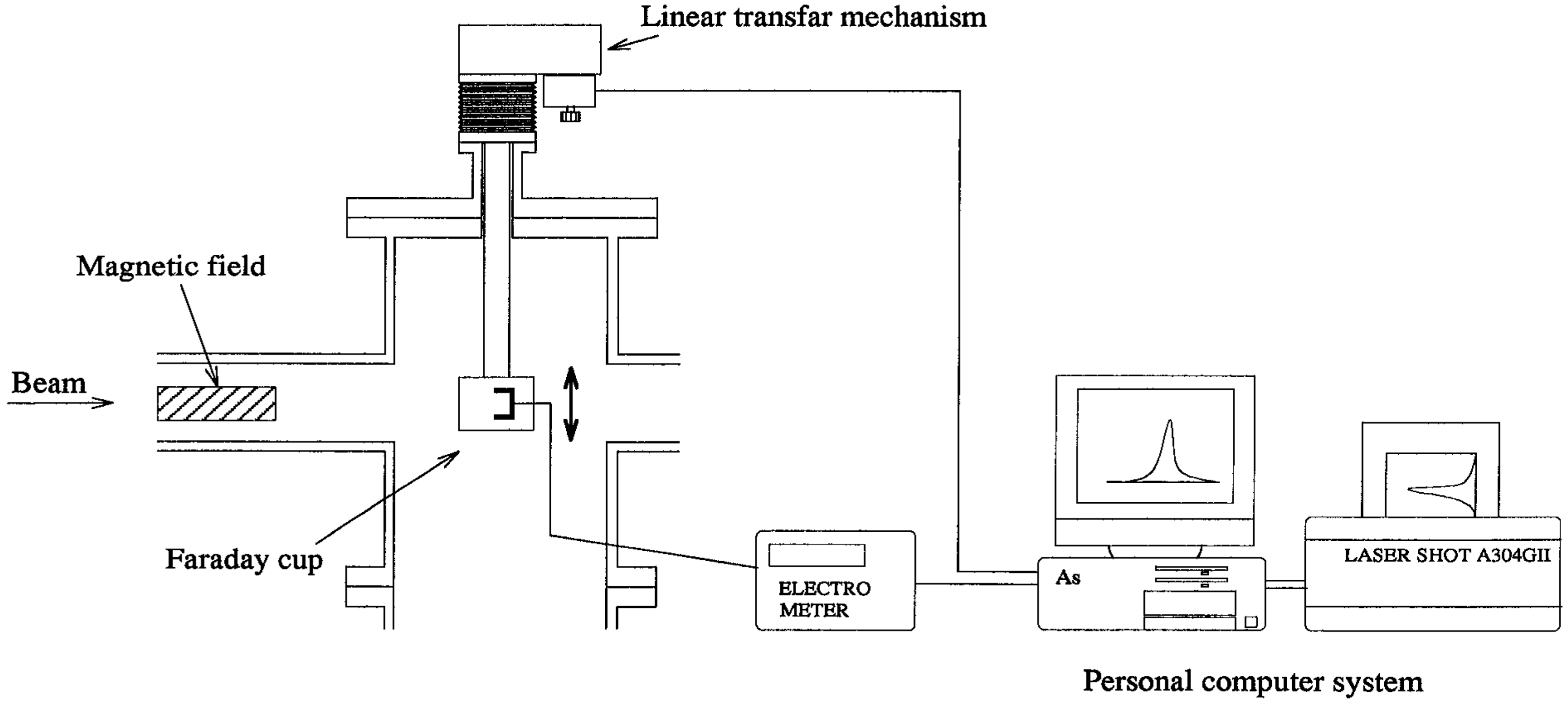

Fig. 19. A schematic view of the Faraday cup system.

§3. Energy Loss Processes

The energy loss mechanism of a projectile in collision with a neutral atom can be considered through the elastic and inelastic processes which occur simultaneously.

The elastic process corresponds to the scattering by the potential between two atoms, whereas, the inelastic process corresponds to that accompanied by an energy transfer into an internal energy, such as electron loss, ionization, and/or excitation of projectile and target atoms.

3-1 Elastic Process

For the elastic energy transfer, the classical theory can be used. The scattering angle θ [rad] in center of mass frame is expressed by an impact parameter b , and an impact energy E , as follows,

$$\theta(b,E)=\pi-2\int_{r_0}^{\infty}\frac{b}{\sqrt{1-\frac{b^2}{r^2}-\frac{V(r)}{E}}}\frac{\mathrm{d}r}{r^2}\ , \tag{9}$$

here, r_0 is the closest distance during the collision, and it is the solution of Eq. (10).

$$1-\frac{b^2}{{r_0}^2}-\frac{V(r_0)}{E}=0\ . \tag{10}$$

Here, $V(r)$ is the potential between the two atoms, and the unified potential which was proposed by Ziegler et al. [14] is used in the present work, because it is known that it well describes collisions between large Z atoms.

$$V(r) = \frac{Z^2 e^2}{r}\left(\phi_a(r) - Z^{-2/3}\phi_b(r)\right) \tag{11}$$

$$\phi_a(r) = 0.09e^{-0.19x} + 0.61e^{-0.57x} + 0.3e^{-2x}$$

$$\phi_b(r) = 0.07\exp\left\{-\left(\frac{1}{7R}\right)^2 - \frac{R}{4} - \left(\frac{R}{4}\right)^2\right\}$$

where,

$$x = R/a\ ,\ a = 0.8853 a_0 Z^{-1/3}\ ,\ R = Z^{1/3} r,$$

a_0 : Bohr radius.

When Z number of the two atoms are different, the effective potential can be given by

$$V_{12}(r) = \sqrt{V_1(r)V_2(r)}\ . \tag{12}$$

This potential gives good approximation for large Z atoms. The energy loss T_{el} by elastic process can be expressed,

$$T_{el}(\theta) = T_m \sin^2\left(\frac{\theta}{2}\right) \tag{13}$$

where T_m is the maximum energy transfer from the projectile to the target atom,

$$T_m = \frac{4M_1M_2}{(M_1+M_2)^2}E \tag{14}$$

M_1 : mass number of the projectile

M_2 : mass number of the target atom.

The largest scattering angle observed in the experiment, $\theta_{\max}$, is limited by the apparatus geometry. The minimum impact parameter, $b_{\min}$, is determined from this angle $\theta_{\max}$. In the present case, assuming that the incident beam to the cell is parallel to the cell axis, the largest scattering angle, $\Theta_{\max}$, in laboratory coordinate is determined by two lengths. One is the distance from the analyzer entrance slit to the exit position of a gas cell, L , and the other is a sum of the cell radius, r_{cell}, and the radius of aperture placed on the analyzer slit, r_{ap}. Then, $\Theta_{\max}$ can be expressed by

$$\Theta_{\max} = \arctan\left(\frac{r_{\text{cell}} + r_{\text{ap}}}{L} \right) . \tag{15}$$

In the present apparatus, r_{cell} is 7 mm, r_{ap} is 1 mm and L is 1400 mm. The maximum scattering angle in center of mass system is given by

$$\theta_{\max} = \Theta_{\max} + \arcsin\left(\frac{M_1}{M_2} \sin \Theta_{\max} \right) . \tag{16}$$

3-2 Inelastic Process

During the inelastic process, a part of the kinetic energy is transferred into an internal energy of projectile and target atoms. The minimum energy required to produce an $\mathrm{Au^+}$ ion from an $\mathrm{Au^-}$ ion is a sum of the electron affinity and the first ionization potential of an Au atom.

$$T_{\text{in}(\mathrm{Au^-} \to \mathrm{Au^+})} = T_{\text{in,min}} = 11.5 \quad [\text{eV}] \tag{17}$$

Firsov proposed a theoretical model to describe an inelastic energy transfer [15], which can be expressed as a function of an impact parameter b [Å] and velocity v [cm/s],

$$T_{\mathrm{in}}(b,\mathrm{v}) = \frac{(Z_1+Z_2)^{5/3}\cdot 4.3\times 10^{-8}\,\mathrm{v}}{\left[1+0.31(Z_1+Z_2)^{1/3}\cdot b\right]^5} \quad [\mathrm{eV}]\ , \tag{18}$$

where

Z_1 : atomic number of the projectile

Z_2 : atomic number of the target atom,

under the condition of

$$\frac{1}{4} \le \frac{Z_1}{Z_2} \le 4\ . \tag{19}$$

In this model, the two-electron stripping process can occur when

$$T_{\mathrm{in}}(b) \ge T_{\mathrm{in}(\mathrm{Au}^- \to \mathrm{Au}^+)}\ , \tag{20}$$

by which the maximum impact parameter b_{max} is determined as the following,

$$T_{\mathrm{in}(\mathrm{Au}^- \to \mathrm{Au}^+)} = T_{\mathrm{in}}(b_{\mathrm{max}})\ . \tag{21}$$

3-3 Total Energy Loss

The amount of energy loss due to elastic and inelastic processes depends upon the impact parameter. The sum of elastic and inelastic energy losses causes the energy broadening of an Au$^+$ beam.

$$T_{\text{tot}}(b) = T_{\text{el}}(b) + T_{\text{in}}(b) \tag{22}$$

Figure 20 shows the elastic scattering angle θ [rad] in the center of mass system, the elastic energy loss T_{el} [eV] and the inelastic energy loss T_{in} [eV] as a function of impact parameter b [Å], when Au$^-$ ion is injected with an impact energy of 44 keV into the Ar target. The elastic energy loss T_{el} does not affect the energy broadening in the energy range of the present experiment.

The energy spectrum which is observed in the experiment can be expressed as

$$F(\varepsilon) = -2\pi \cdot b(\varepsilon) \cdot \frac{\mathrm{d}b(\varepsilon)}{\mathrm{d}\varepsilon} \cdot f(\theta)\,, \tag{23}$$

where $b(\varepsilon)$ is the inverse function of $T_{\text{tot}}(b)$ defined in the region of $b_{\text{min}} \leq b \leq b_{\text{max}}$, and $f(\theta)$ is the efficiency of particle detection in the present experimental system. The latter is also a function of an impact parameter, which becomes zero at $b = b_{\text{min}}$(or $\theta = \theta_{\text{max}}$). Figure 21 shows an example of spectrum, $F(\varepsilon)$. To compare with the experimental results, here we consider the energy width, $F_{1/2}$, which is FWHM of the energy loss spectrum, $F(\varepsilon)$.

Figure 22 shows the energy width, $F_{1/2}$, as a function of the impact energy, $E \leq 50$ keV, in He, Ne, Ar, Kr and Xe. In the lower energy

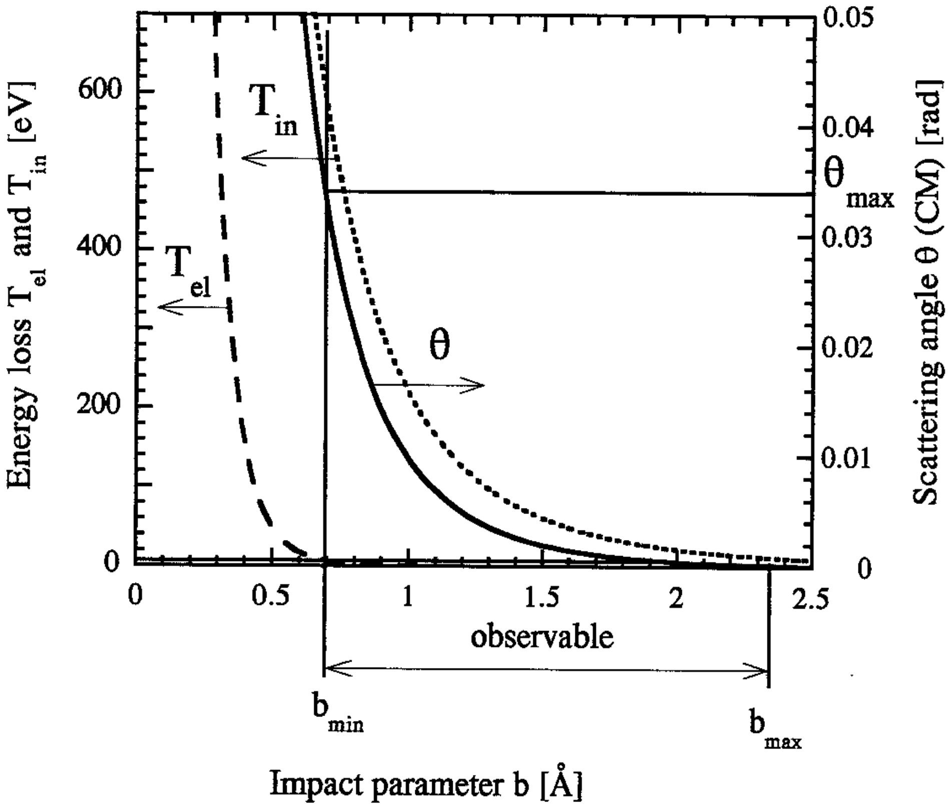

Fig. 20. The elastic scattering angle θ [rad] in the center of mass system (solid line), the elastic energy loss T_{el} [eV] (dashed line) and the inelastic energy loss T_{in} [eV] (dotted line) plotted as functions of impact parameter b [Å], when an Au^- ion is injected with an impact energy of 44 keV, into the Ar target to produce an Au^+ ion beam. The elastic scattering angle and the energy loss are calculated by the classical theory using the Ziegler's unified potential between two atoms, and the inelastic energy loss is calculated by the Firsov's theory. The θ_{max} is the largest observable angle in center of mass system determined by the experimental geometry.

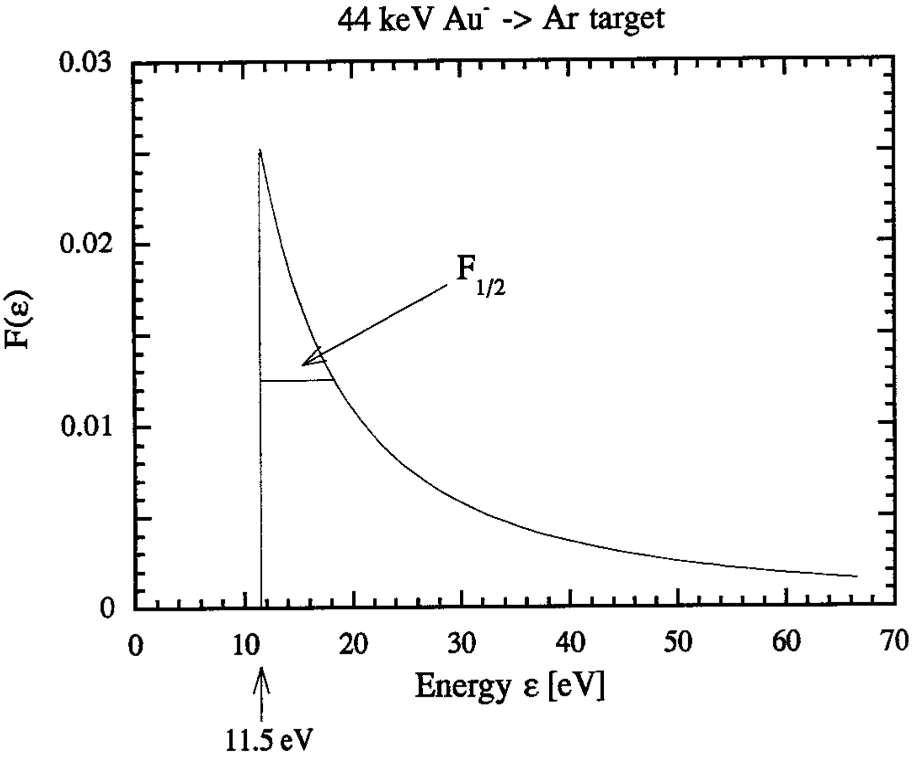

Fig. 21. An example of spectrum, $F(\varepsilon)$, at an impact energy of 44 keV for an Ar target.

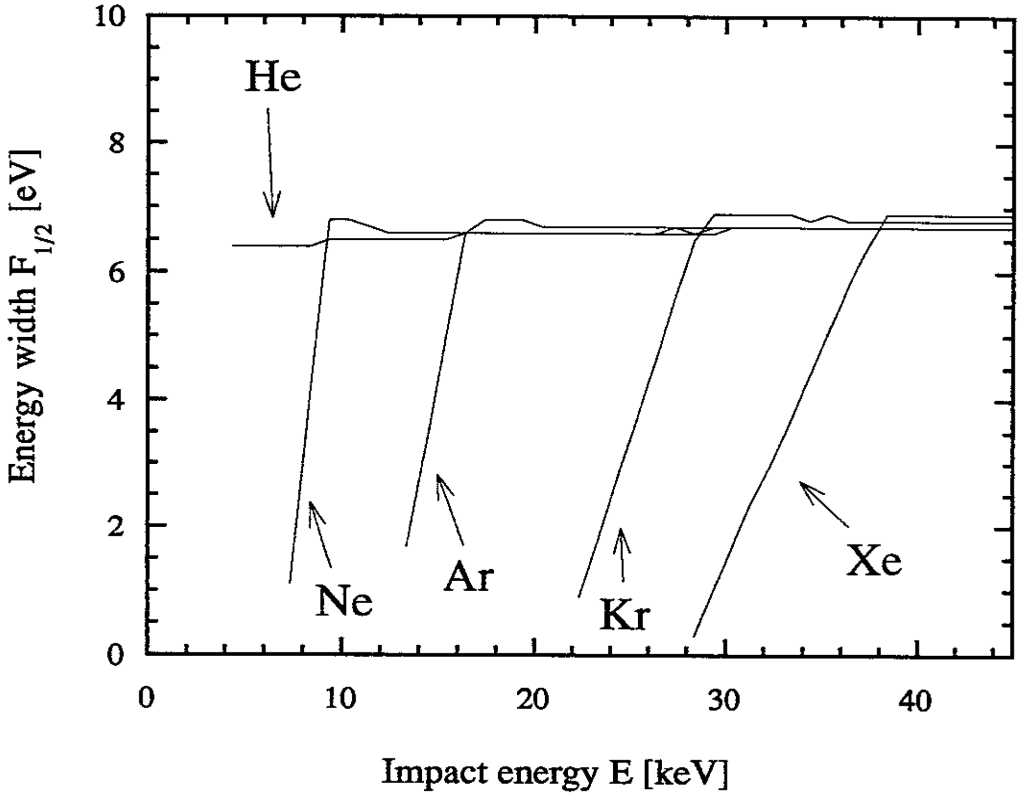

Fig. 22. The numerically calculated energy width, $F_{1/2}$, plotted as functions of impact energy, E [keV], for target gases of He, Ne, Ar, Kr and Xe.

region, the energy width increases as an impact energy increases, and it is larger for lighter target atoms. But in the higher energy region, the energy broadening is saturated at about 7 eV, and there is very weak dependence on the energy and the target mass. The spectra, $F(\varepsilon)$, for Xe target are shown in Fig. 23, where the impact energy is 40 keV, 100 keV, 500 keV, 1 MeV, 2 MeV and 3 MeV. These FWHM of those spectrum are always the same about 7 eV, and the reason is analytically explained in appendix B.

3-4 Energy Straggling

In the target density region that the multiple collision is not negligible, the energy straggling of a beam is generally explained by the L.S.S. theory [16]. In the energy region higher than a few MeV/nucleon, the elastic energy transfer is not negligible. But in the energy region less than that, like in the present case, the inelastic energy transfer is dominant. Therefore, the inelastic energy loss function, T_{in}, can be used to estimate the energy straggling. Equation (18) can be expressed in a simplified form as follows,

$$T_{in}(b) = \frac{C}{[1 + A \cdot b]^5} \ \text{[eV]} \qquad (24)$$

$$A = 3.1(Z_1 + Z_2)^{1/3} \cdot 10^7$$

$$C = (Z_1 + Z_2)^{5/3} \cdot 4.3 \times 10^{-8} \cdot \mathrm{v}$$

b [cm] : Impact parameter

v [cm/s] : Particle velocity.

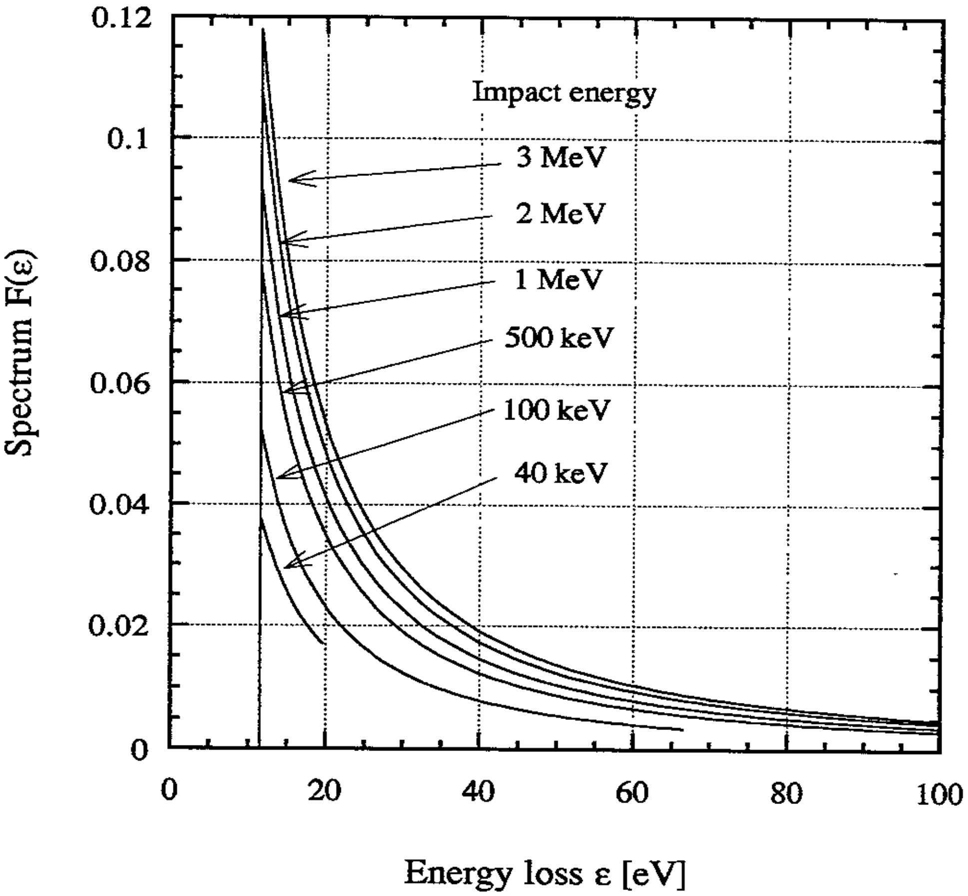

Fig. 23. The energy spectrum, F (ε), for Xe target at some impact energies. The FWHM does not depend upon the impact energy.

In the L.S.S. theory, the squared energy straggling is given by an integral of the squared energy loss function over the impact parameter from zero to infinity [17].

$$\begin{aligned}\Omega_0{}^2 &= nl\int_0^\infty \{T_{\mathrm{el}}(b)+T_{\mathrm{in}}(b)\}^2\cdot 2\pi b\mathrm{d}b\\ &\approx nl\int_0^\infty \{T_{\mathrm{in}}(b)\}^2\cdot 2\pi b\mathrm{d}b = \frac{2\pi C^2 nl}{72A^2}\ .\end{aligned}\tag{25}$$

However, when an energy loss spectrum of a singly-charged component of a beam is measured at a forward angle, the energy loss function in a small impact parameter region cannot contribute to the straggling. Therefore, the lower limit of the integral region, $b_{\text{s-min}}$, should be considered. The geometrical configuration of the gas cell and the tandem acceleration system limit the maximum observable scattering angle, which determines the minimum impact parameter, $b_{\theta}=b_{\text{min}}$, as is described in section (3-3). Another limit is the impact parameter, b_{++}, which corresponds to the inelastic energy transfer to produce an Au^{++}. The lower limit of the integral, $b_{\text{s-min}}$, is the larger of the two, b_{θ} or b_{++}.

$$\begin{aligned}\Omega_b{}^2 &= nl\int_{b_{\text{s-min}}}^\infty \{T_{\mathrm{in}}(b)\}^2\cdot 2\pi b\mathrm{d}b\\ &= \Omega_0{}^2\cdot\frac{1+9Ab_{\text{s-min}}}{\left(1+Ab_{\text{s-min}}\right)^9}\end{aligned}\tag{26}$$

Figure 24 shows the calculated energy straggling, Ω_b, and the impact parameter b_{θ} and b_{++} as a function of the impact energy when the Au^{+} beam passes through the Xe target of 10^{16} cm^{-2}. The straggling given by the L.S.S. theory, Ω_0, is also shown for comparison. The energy straggling of present calculation is smaller than that calculated by the

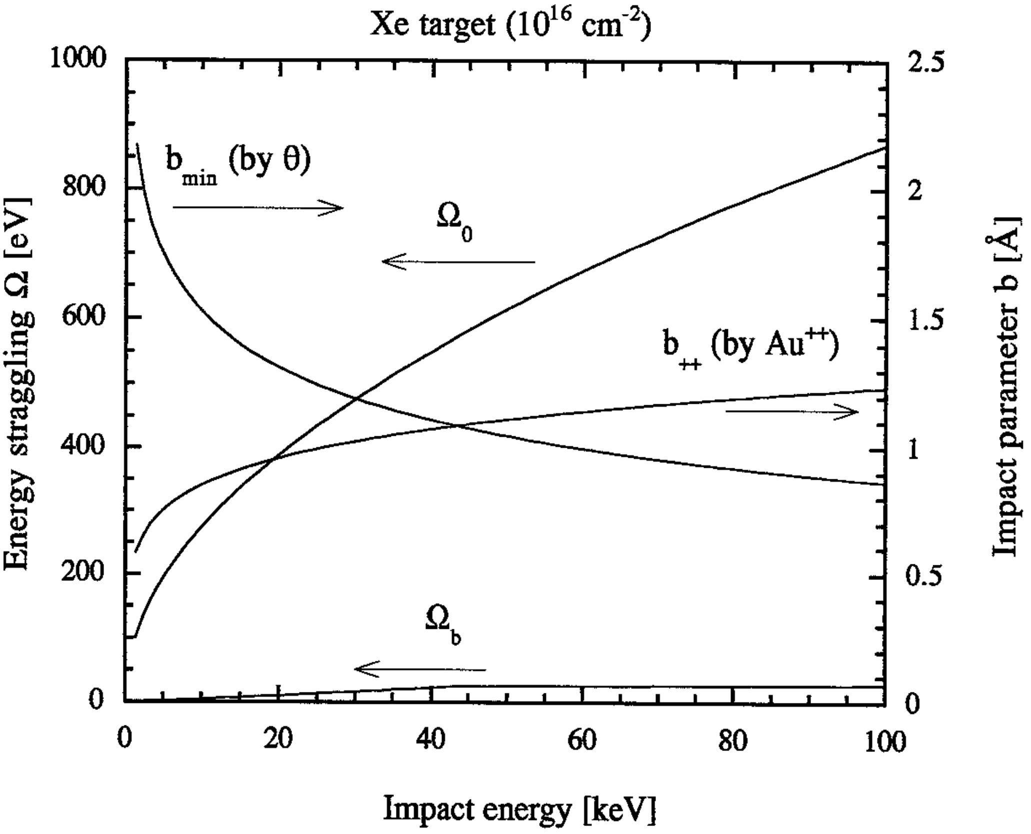

Fig. 24. Energy straggling for a Xe target of 10^{16} cm^{-2} calculated by integrating from zero to infinity (Ω_0) and that from $b_{s\text{-}min}$ to infinity (Ω_b). The minimum impact parameter $b_{s\text{-}min}$ is determined by the larger value of that defined by geometry and reionization.

original L.S.S. theory by factor of more than 5. In Fig. 25, the straggling in various target gases are compared at the thickness of 10^{16} cm^{-2}. When the impact energy is relatively low, the straggling is restricted by the maximum observable angle, but it is limited by the ionization at the higher energy. In the latter region, the difference due to the target gas is small. Figure 26 shows the increase of the straggling when the target thickness increases.

3-5 Cross Sections

Some cross sections can be calculated by the inelastic energy loss function of Firsov (Eq.18), and scattering angle, θ , (Eq.9) calculated with the unified potential of Ziegler's. Here the electron loss cross section is defined as $\sigma_{i\,f}$ where the suffix 'i ' and 'f ' denote the initial and the final charge state. In this thesis, the electron stripping and the scattering cross sections are mainly considered.

A differential cross section $q(\theta)$ is described with an impact parameter, as the following,

$$2\pi b\,\mathrm{d}b = 2\pi q(\theta)\sin\theta\,\mathrm{d}\theta \,. \tag{27}$$

Then, the cross section, $\sigma_{i\,f}$, measured under a certain geometrical condition, can be expressed as

$$\begin{aligned}\sigma_{i,f} &= \int q(\theta)\mathrm{d}\omega = \iint q(\theta)\sin\theta\,\mathrm{d}\theta\,\mathrm{d}\phi \\ &= 2\pi\int q(\theta)\sin\theta\,\mathrm{d}\theta = 2\pi\int_{b_{\min}}^{b_{\max}} b\,\mathrm{d}b \\ &= \pi\left(b_{\max}{}^2 - b_{\min}{}^2\right) \,.\end{aligned} \tag{28}$$

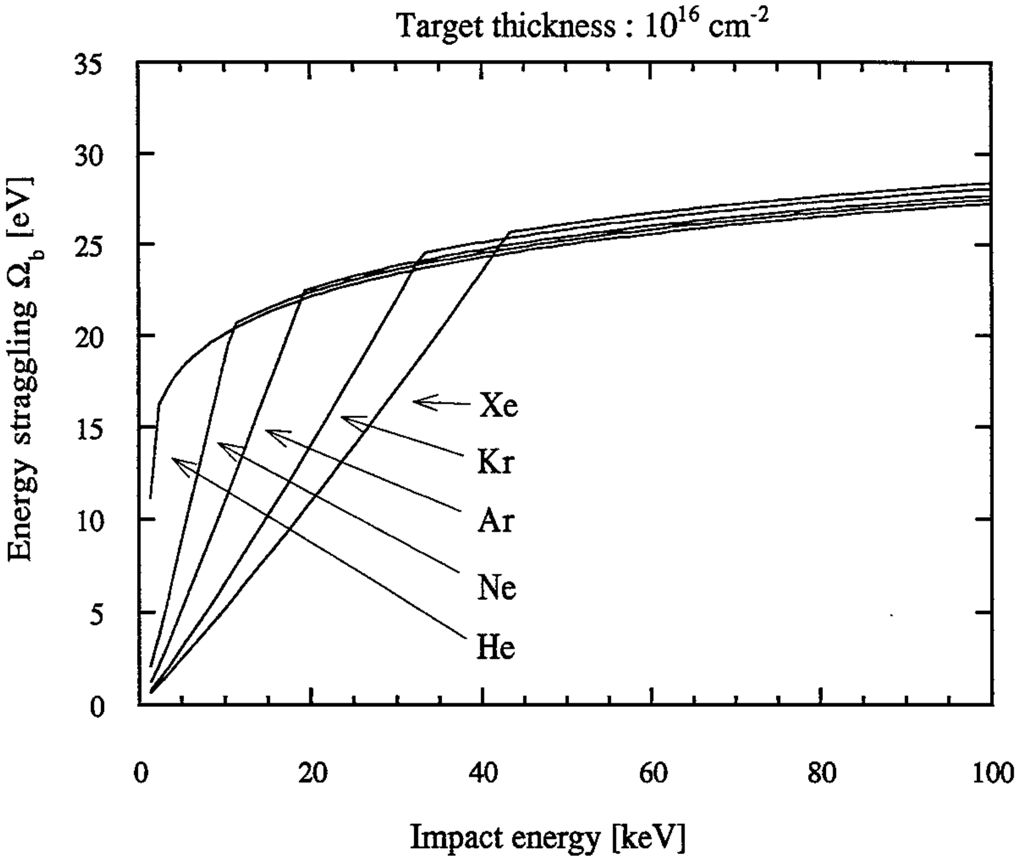

Fig. 25. The energy straggling as a function of impact energy for He, Ne, Ar, Kr and Xe gas target of 10^{16} cm^{-2}.

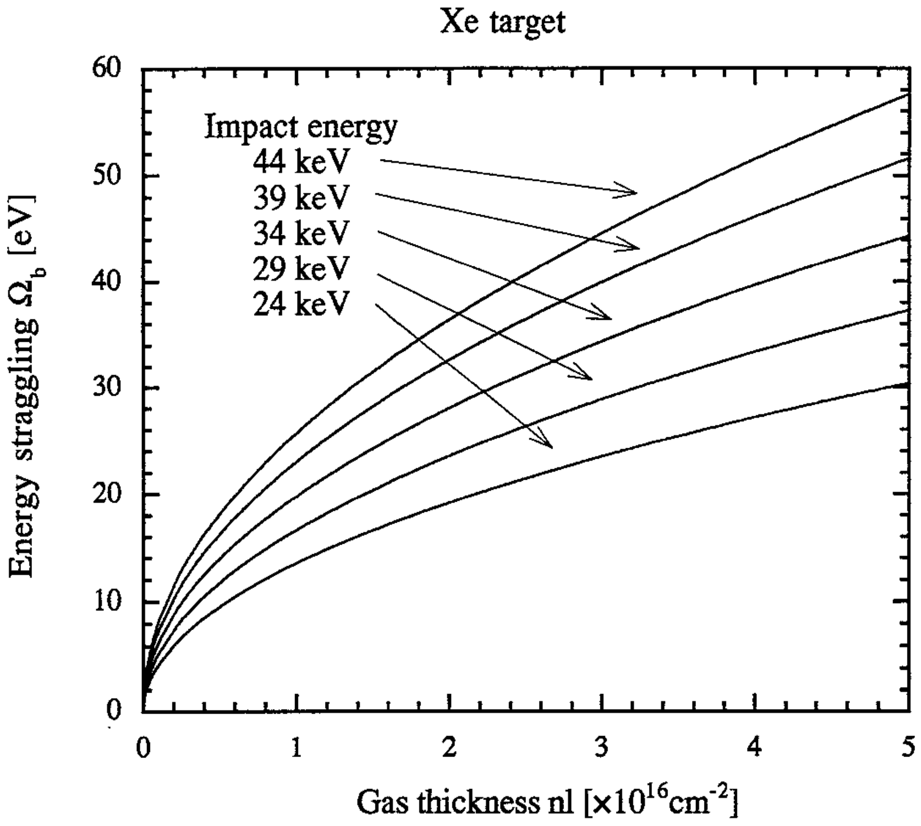

Fig. 26. The energy straggling as a function of target gas thickness. The impact energy is 44, 39, 34, 29 and 24 keV, and the target is Xe.

The cross section is determined by the minimum impact parameter, $b_{\min}$, and a maximum impact parameter, $b_{\max}$, defined in the section (3-1) and (3-2). Figure 27 shows the double charge stripping cross section, $\sigma_{-1,+1}$, as a function of the impact energy for He, Ne, Ar, Kr and Xe target.

Assuming that the potential between an Au and a target atom is not affected much for changing the charge state of the Au atom, and the same energy loss function can be used for various charge states, then, the minimum impact parameter is again determined by experimental geometry, and the maximum impact parameter is determined by the energy loss required for each electron loss process. Consequently, some cross sections such as $\sigma_{-1,0}$, σ_{-1+2}, $\sigma_{-1,+3}$ and so on can be calculated. Singly charge stripping cross section, $\sigma_{-1,0}$, is calculated using the maximum impact parameter, $b_{\max 0}$, determined by the electron affinity only. Figure 28 shows the cross section, $\sigma_{-1,0}$, as a function of the impact energy for various target atoms. Some cross sections can be calculated as shown Fig. 29 for some inert gases at 3 MeV. The scattering cross section, σ_{s} , is calculated as,$\sigma_{s} = \pi b_{\min}{}^{2}$.

These cross sections are used to estimate the charge fractions. The detail is discussed in the paragraph 4-6. An example of the calculation code is shown in appendix C.

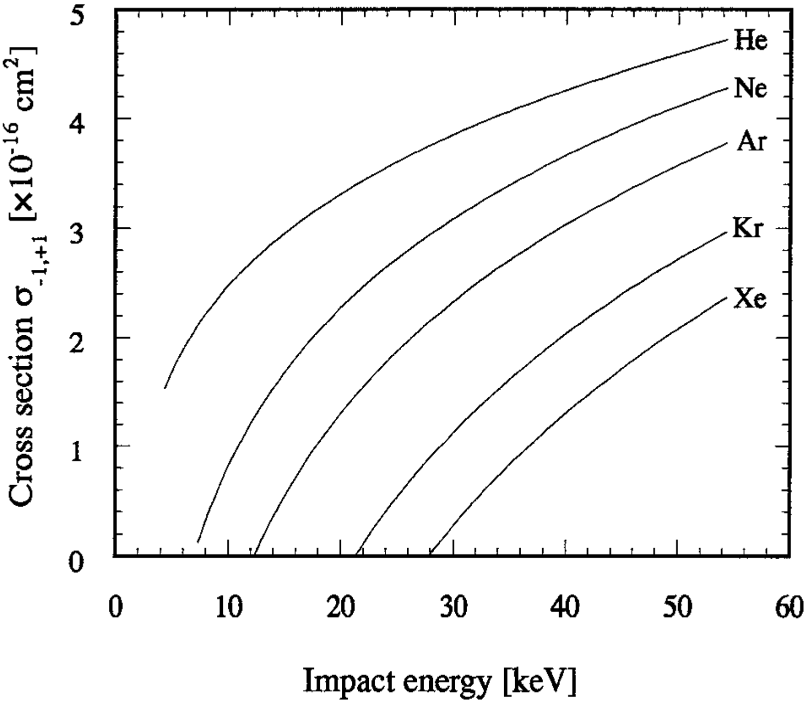

Fig. 27. The cross section $\sigma_{-1,+1}$, as a function of impact energy calculated by using b_{min} and b_{max}.

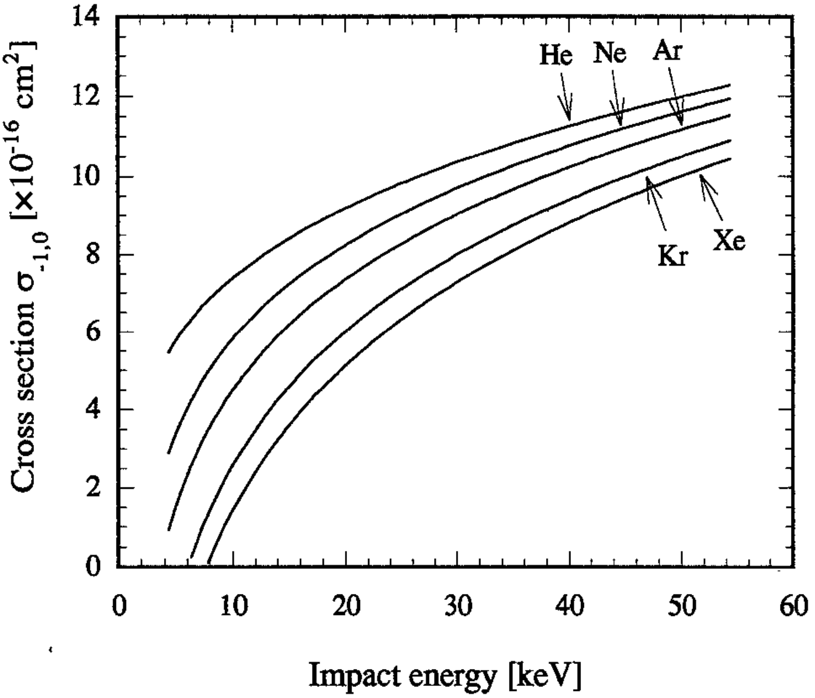

Fig. 28. The cross section $\sigma_{-1,0}$, as a function of impact energy calculated by using $b_{\min}$ and $b_{\max0}$.

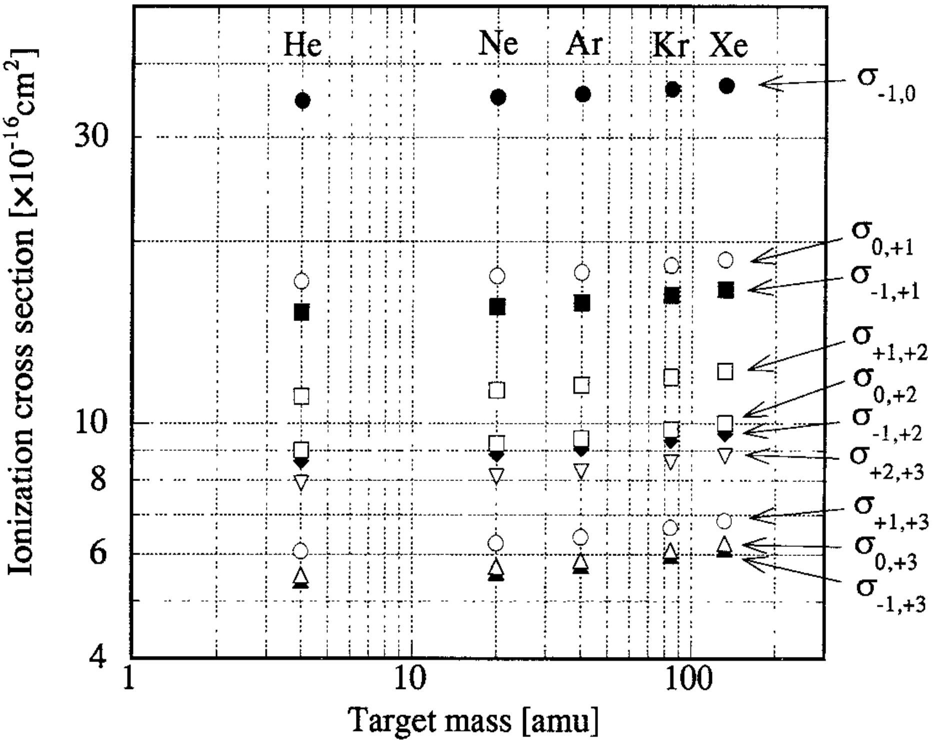

(a) Ionization cross section

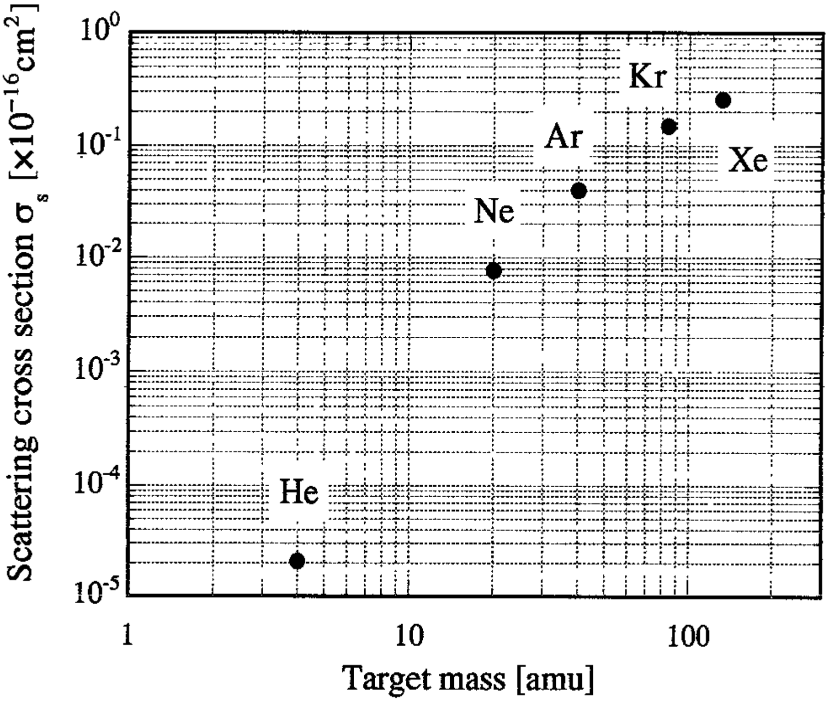

(b) Scattering cross section

Fig. 29. The electron stripping (a) and the scattering (b) cross sections as functions of target mass with an impact energy of 3 MeV calculated theoretically.

§4. Results and Discussion

4-1 Energy Width of Negative Ion Beam

Figure 30 shows a typical spectrum of negative ion beam extracted from the plasma-sputter-type negative ion source with the extraction voltage, V_{ext}, of 4 kV. Here two peaks are seen. One corresponds to the peak of negative ions produced by the surface production and the other corresponds to those by the volume production. The peak by the volume production contains mainly O^- and H^-, the peak by the surface production contains mainly Au^-. The difference of energy between the two peaks agrees with the target voltage, V_{T}.

The measured Au^- energy width as a function of the target voltage is shown in Fig. 31. The energy width at small acceleration voltage indicates an original Au^- energy width, because the instrumental width is much smaller than the measured spectrum width for a low energy beam. Thus, the original Au^- energy width is regarded to be 4~5 eV.

4-2 Au+ Energy Shift without Tandem Acceleration

An example of the energy spectrum of the positive ion beam produced by a charge stripping process is shown in Fig. 32 together with that of the original negative ion beam. An energy shift, a peak energy difference in positive and negative ion beam spectra can be seen clearly. Changing the acceleration voltage from 1 to 5 kV, the difference is always around 10~14 eV in the low gas cell pressure region. The energy shift is caused by the charge stripping process and the gas scattering. The latter is negligible because the target thickness is small. The former is caused by the two

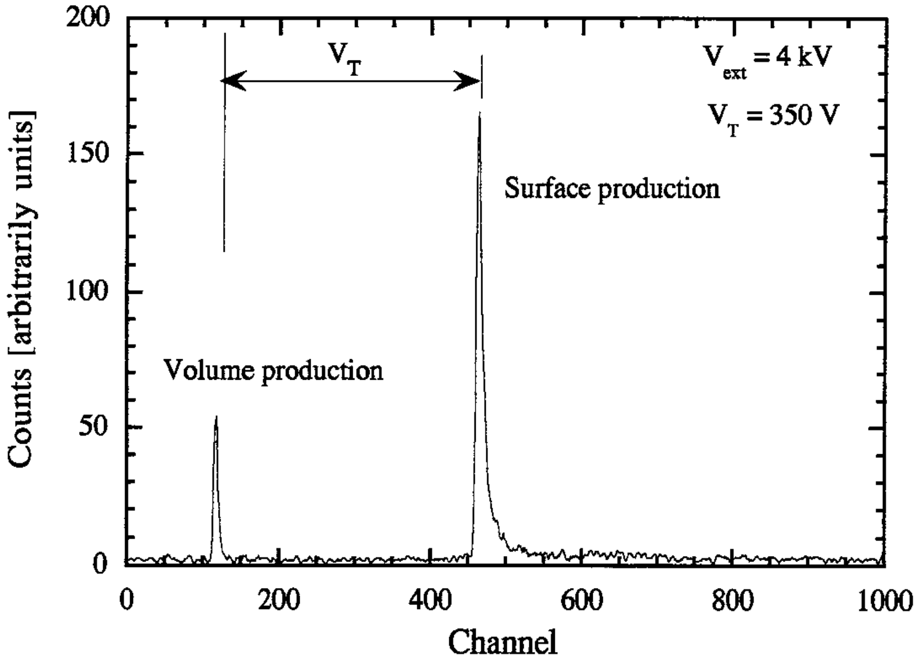

Fig. 30. An example of the negative ion beam spectrum. The beam is extracted at $V_{\text{ext}} = 4$ kV with a target voltage $V_{\text{T}} = 350$ V. Two peaks shown correspond to those made by the volume and the surface production.

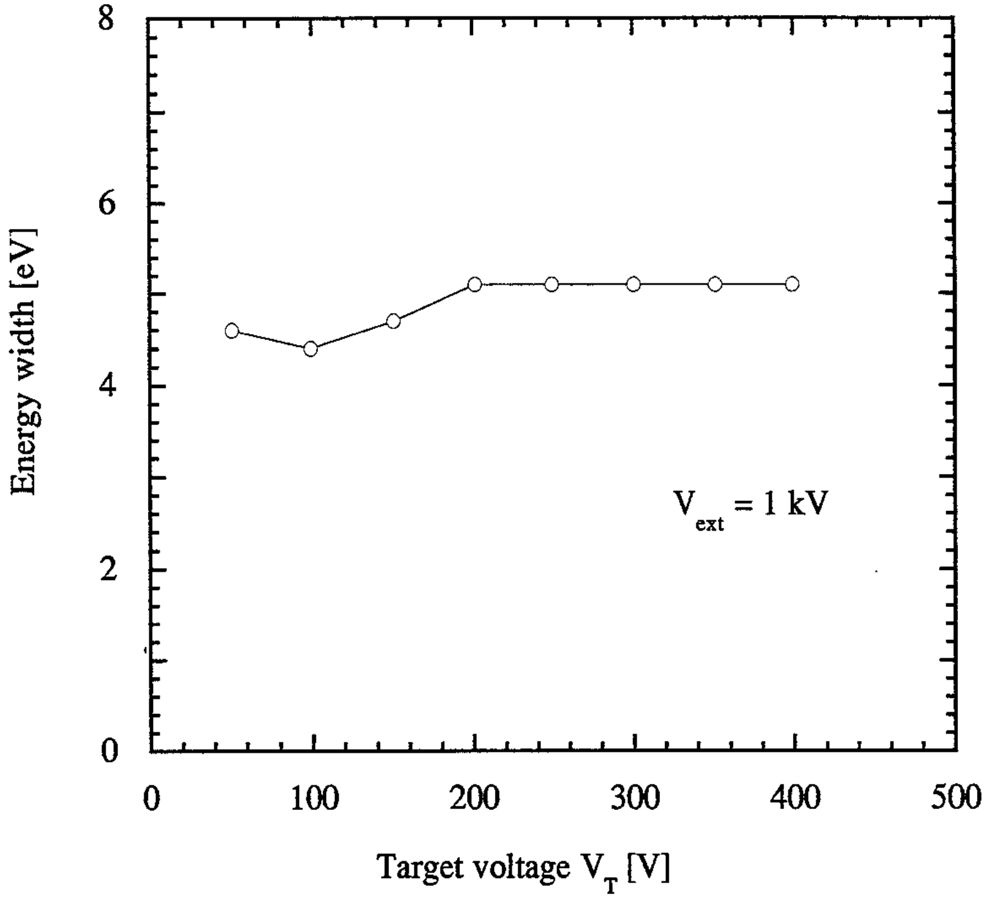

Fig. 31. Energy width of an Au$^-$ ion beam plotted as a function of target voltage at V_{ext}=1kV.

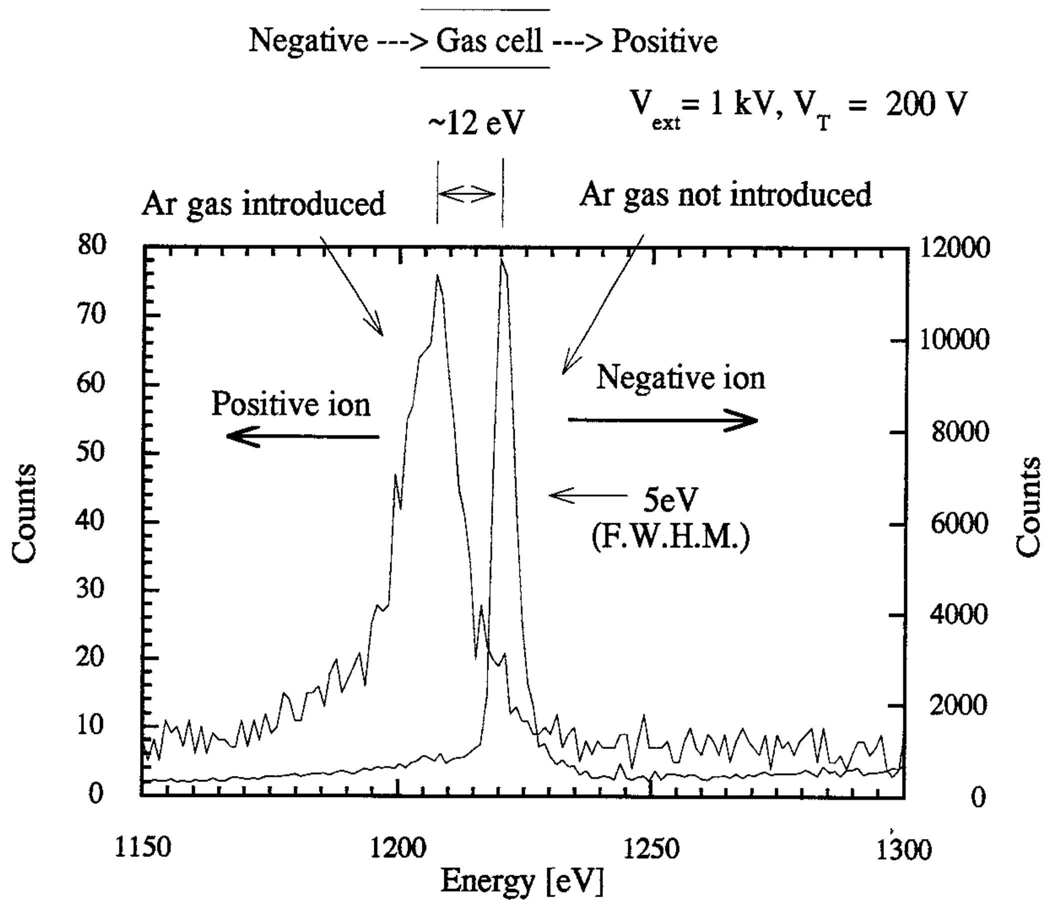

	Electron affinity [eV]	First ionization potential [eV]	Sum [eV]
Au	2.3	9.22	11.5
O	1.5	13.6	15.1
H	0.75	13.6	14.4

Fig. 32. An example of the original negative beam spectrum and that of the positive beam produced by the charge stripping process. The negative beam is measured when an Ar gas is not introduced into the charge stripping cell, and the positive beam is measured with an Ar gas. The electron affinity, the first ionization potential and the sum for three kinds of atoms, are summarized in the Table.

electron loss process, the energy of which is a sum of the electron affinity and the first ionization energy of the atom. In the spectra of Fig. 32, the ion beam contains gold, oxygen and hydrogen ions. The table inserted in the figure shows the electron affinity, the first ionization energy and its sum for these atoms. These values are about 12 eV and it explains the energy shift due to the two electron stripping process.

4-3 Estimation of Energy Width and its error;

In the present work, an energy width is determined by fitting the energy spectrum with a Gaussian distribution. For example, Fig.14(b) shows the energy spectrum separated by magnetic field on the entrance drift space on the analyzer. Three peaks are shown in Fig.14(b), which correspond to Au$^+$, O$^+$ and H$^+$ ion species, respectively. Fitting this spectrum with a combination of three Gaussians, these energy widths, W_{Gauss}, are determined as the following,

$$y = \sum_{i=\mathrm{Au,O,H}} \exp\left\{-\left((x - x_{0,i}) / W_{\mathrm{Gauss},i}\right)^2\right\} \tag{29}$$

where

x : a parameter corresponding to energy (horizontal axis in Fig.14(b))

$x_{0,i}$: the central value of x of Gaussian

y : the counts of ion (vertical axis in Fig 14(b))

$W_{\mathrm{Gauss},i}$: a half value of 1/e width of the i -th peak.

Therefore, the width, W_{Gauss}, is converted to the FWHM by,

$$W_{\mathrm{FWHM,Au}} = 2W_{\mathrm{Gauss,Au}}\sqrt{\ln 2}\ . \tag{29}$$

In the analysis of the energy width, the error, σ_{w}, is estimated by taking the fitting error, σ_{f}, and that of the analyzer resolution, σ_{an}, into account as the following,

$$\sigma_{\mathrm{w}} = \sqrt{\sigma_{\mathrm{f}}^{\,2} + \sigma_{\mathrm{an}}^{\,2}}\ . \tag{30}$$

Then, the measured energy width (FWHM) is expressed by

$$W \pm \sigma_{\mathrm{w}}\ . \tag{31}$$

The energy width at small target thickness, W_{s}, is determined as the mean energy width in the region where the thickness, nl , is less than 1.0×10^{15} cm^{-2}. When an each value in this region is expressed as the following,

$$W_i \pm \sigma_i\ , \tag{32}$$

then, the mean value, W_{s}, and its uncertainty, σ_{s}, are denoted as,

$$W_{\mathrm{s}} = \frac{\sum(w_i W_i)}{\sum w_i} \tag{33}$$

$$\sigma_{\mathrm{s}} = \frac{1}{\sum(w_i)} \tag{34}$$

where

$w_i = \dfrac{1}{\sigma_i^{\,2}}$: the weighting factor.

Finally, the measured energy width at small target thickness is expressed by

$$W_s \pm \sigma_s \,. \tag{35}$$

4-4 Energy Width of Positive Ion Beams Produced at Small Target Gas Thickness

As is shown in Fig. 33, the spectrum of the two-electron stripped Au^+ shows a broader peak than that of the original Au^- beam. The energy width is constant in the region of the target gas thickness less than 1×10^{15} cm^{-2}, and it is broadened by multiple collision at a larger gas thickness. In this paragraph, the widths in the region, where the effect of multiple collision processes are negligible, are dealt with. We also measured the attenuation curve of the Au^- beam, and selected a gas thickness region where the two-electron stripping process ($Au^- \rightarrow Au^+$) was dominant. Several kinds of inert gases, He, Ar, Kr and Xe were introduced into the stripping cell as the target gas. Figure 34 shows the energy width of the beam as a function of an impact energy for those gases when its thickness is smaller than 2×10^{15} cm^{-2}.

The dependence of the energy width upon an impact energy and that upon the target mass show the tendencies as the theoretical prediction. In order to compare them, the calculated energy spectra are convoluted with energy resolution of the analyzer and the stability of the tandem accelerator power supply. The result is shown in Fig. 34, here, the experimental data points are the measured FWHM before the correction of the resolution. The energy dependence and that upon the target mass are well reproduced but the calculated values are much smaller than the measured width.

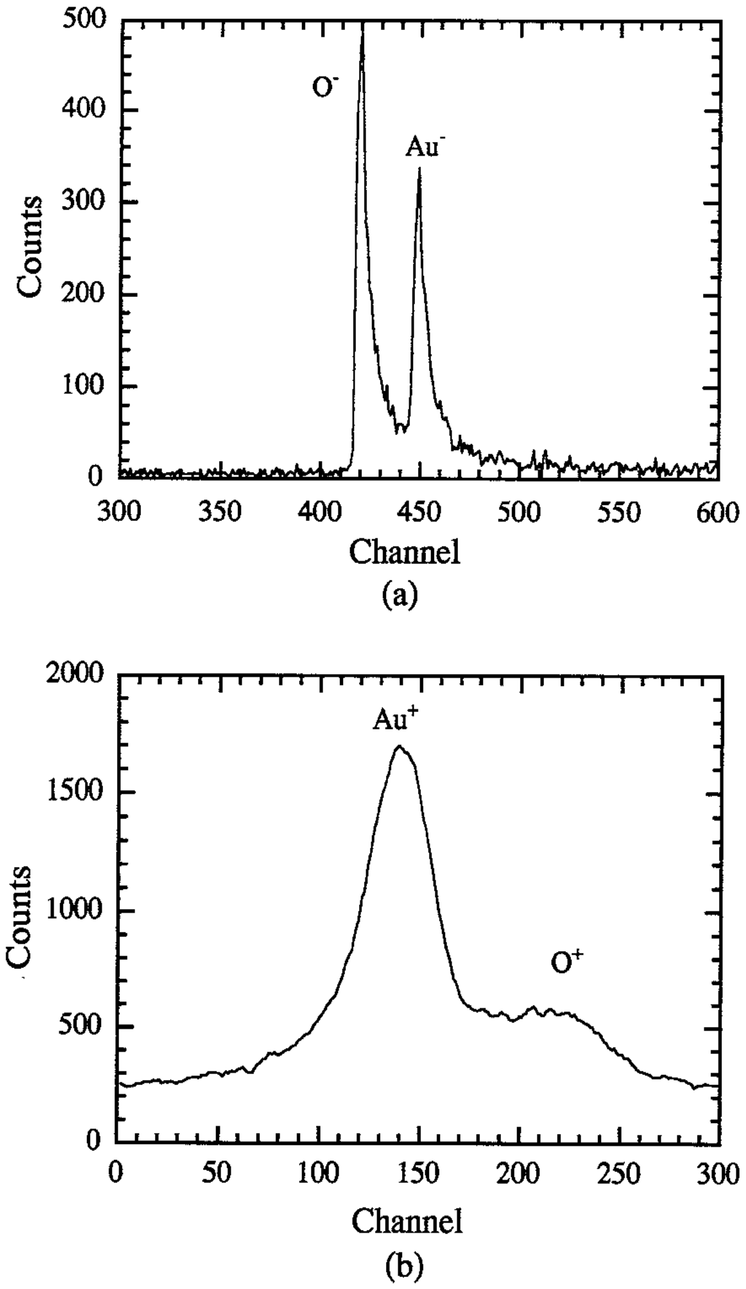

Fig. 33. Typical spectra of (a) the original Au$^-$ beam, and (b) the Au$^+$ beam from the tandem acceleration system. An Ar gas of 2.3×10^{-3} Torr was introduced to the charge stripping cell. The preacceleration and tandem acceleration voltages were 4 kV and 35 kV, respectively. Here, one channel corresponds to 1.04 eV. The oxygen component has the same energy as the gold beam, but it is swept by the magnets by 30 channels (O$^-$), or by 80 channels (O$^+$).

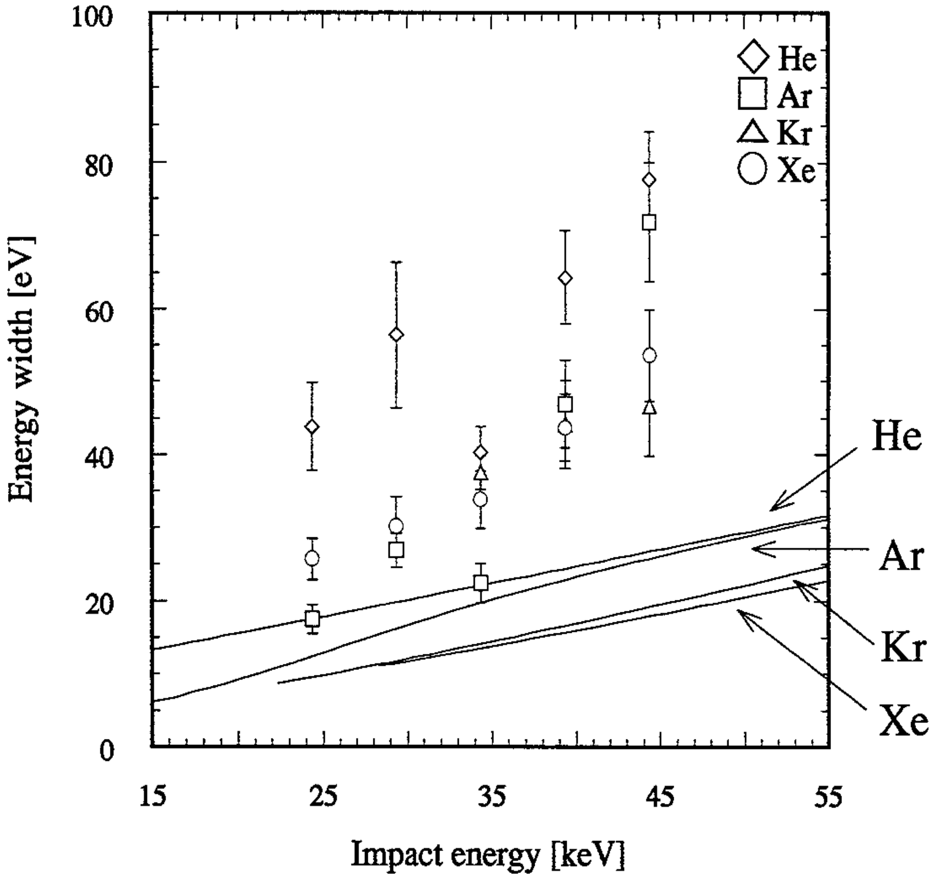

Fig. 34. The dependence of the measured energy width on the impact energy, for target gases of He, Ar, Kr and Xe. Solid curves indicate the calculated energy width of *F(ε)* (Fig. 22.) convoluted by the energy resolution of the analyzer and the stability of the tandem accelerator power supply.

Because the scattering angle is a steep increasing function for decreasing impact parameter, the increase of the observation solid angle should not severely affect the spectrum. Especially, the peak shape is mostly determined by the inelastic energy loss near $b_{\max}$. Some discrepancies are seen in comparison of the measured energy width with the theoretical prediction. The discrepancy in case of He target, might be due to the unsatisfactory condition of Firsov's theory (see Eq.19). The inelastic energy transfer model of Firsov uses an electron distribution function of the semi-classical Thomas-Fermi model. This model is widely accepted to describe an overall structure of collisions between heavy particles at low velocity, but the modification of electron distribution function in an atom might affect the shape of $T(b)$.

If the positive ions are produced from Au^0 in the two step process ($Au^- \rightarrow Au^0$, $Au^0 \rightarrow Au^+$), the energy width of Au^+ beam is mainly determined by the second process, because the first step occurred at the large impact parameter and the energy broadening is small. Then the two step process might results in a little bit less energy width than that of the single step, because the internal energy change of the former process ($Au^0 \rightarrow Au^+$, 9.2 eV) is less than that of the latter ($Au^- \rightarrow Au^+$, 11.5 eV).

4-5 Energy Width of Positive Ion Beams Produced at Large Target Gas Thickness

In this paragraph, the widths in the region where the multiple collision processes are not negligible are dealt with. The energy width as a function of target thickness are shown in Fig. 35, Fig. 36, Fig. 37 and Fig. 38 when the target is Xe, Kr, Ar and He, respectively. The energy

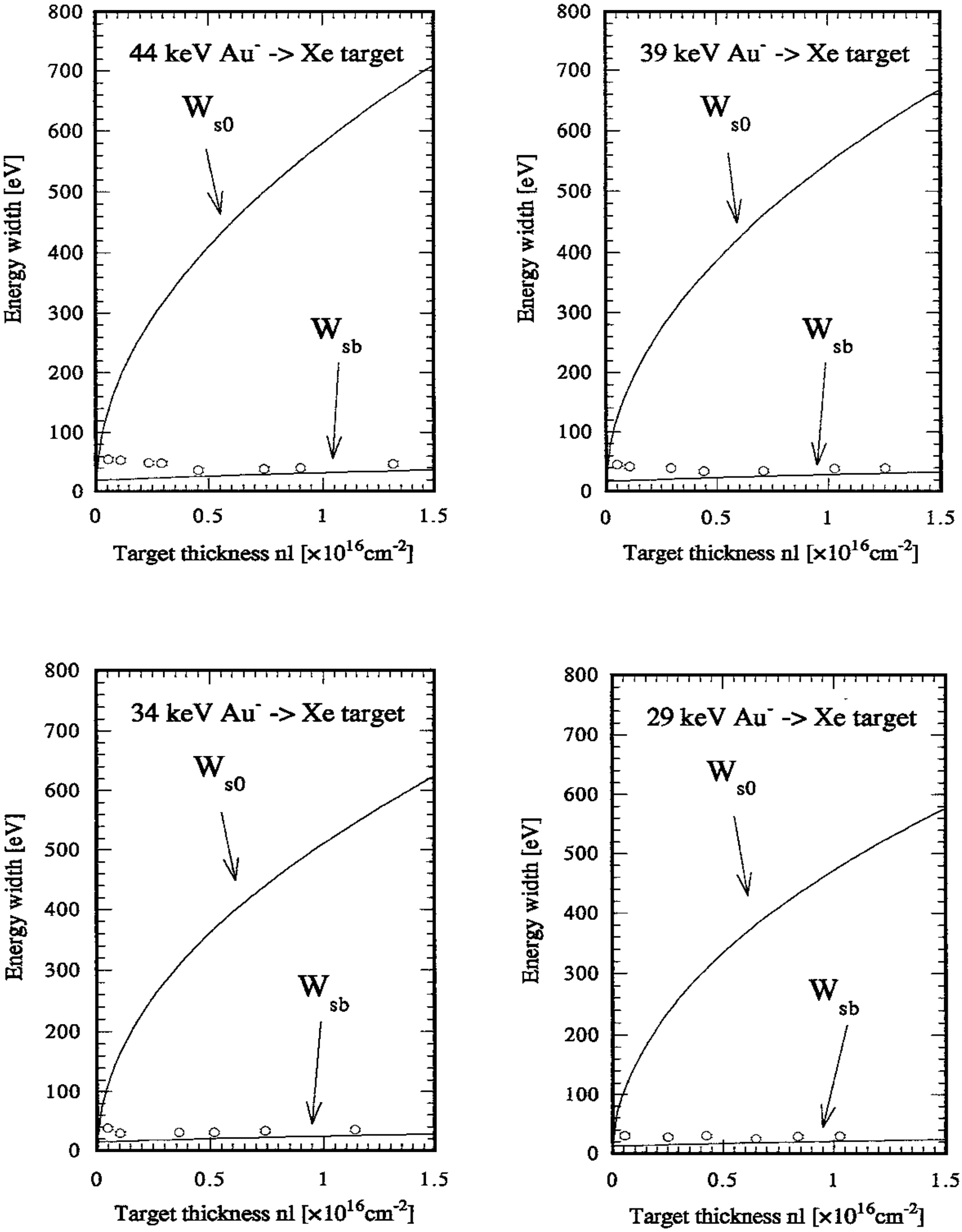

Fig. 35. The measured energy width and the theoretically calculated one plotted as a function of Xe target gas thickness for impact energies of 44, 39, 34 and 29 keV.

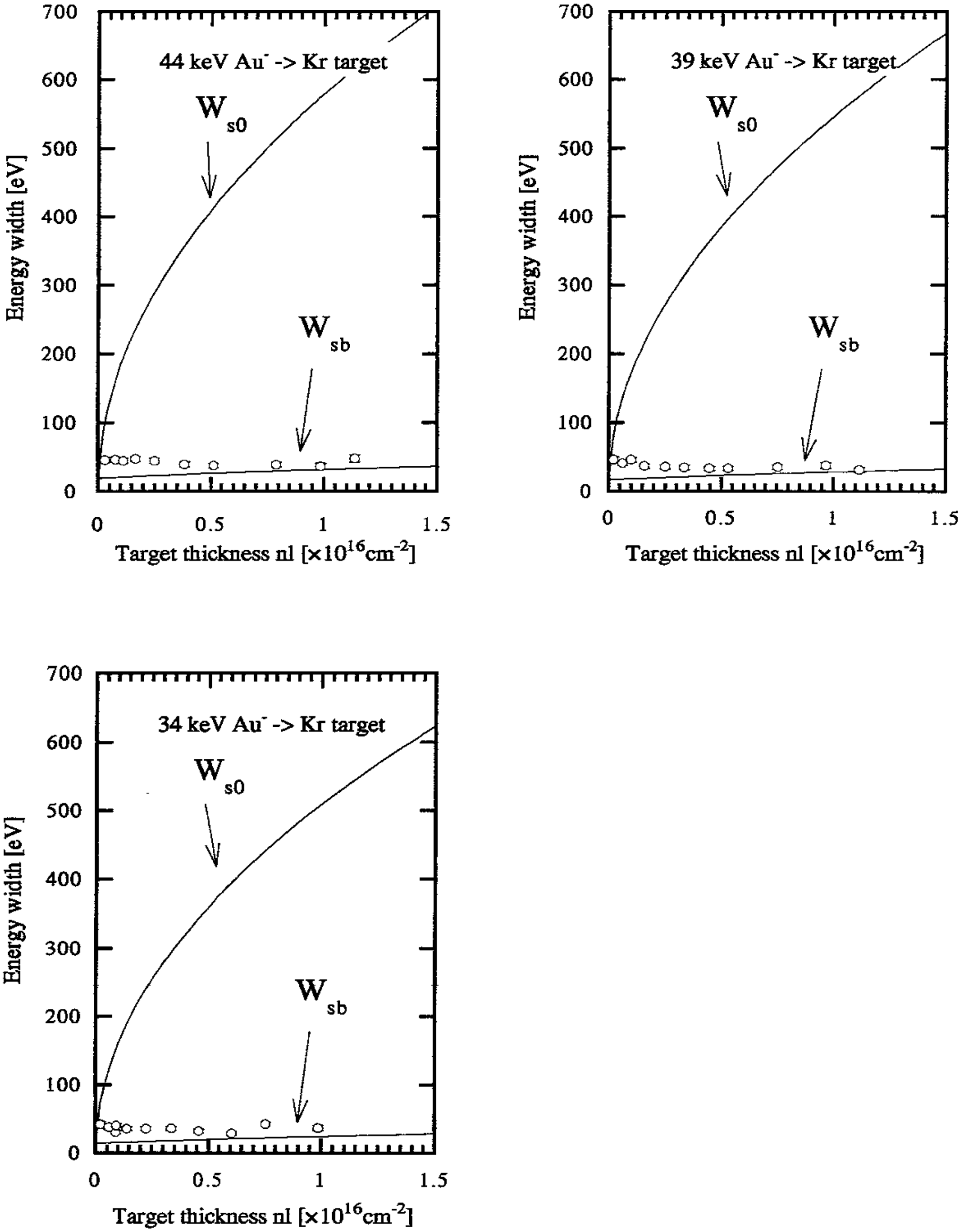

Fig. 36. The measured energy width and the theoretically calculated one plotted as a function of Kr target gas thickness for impact energies of 44, 39 and 34 keV.

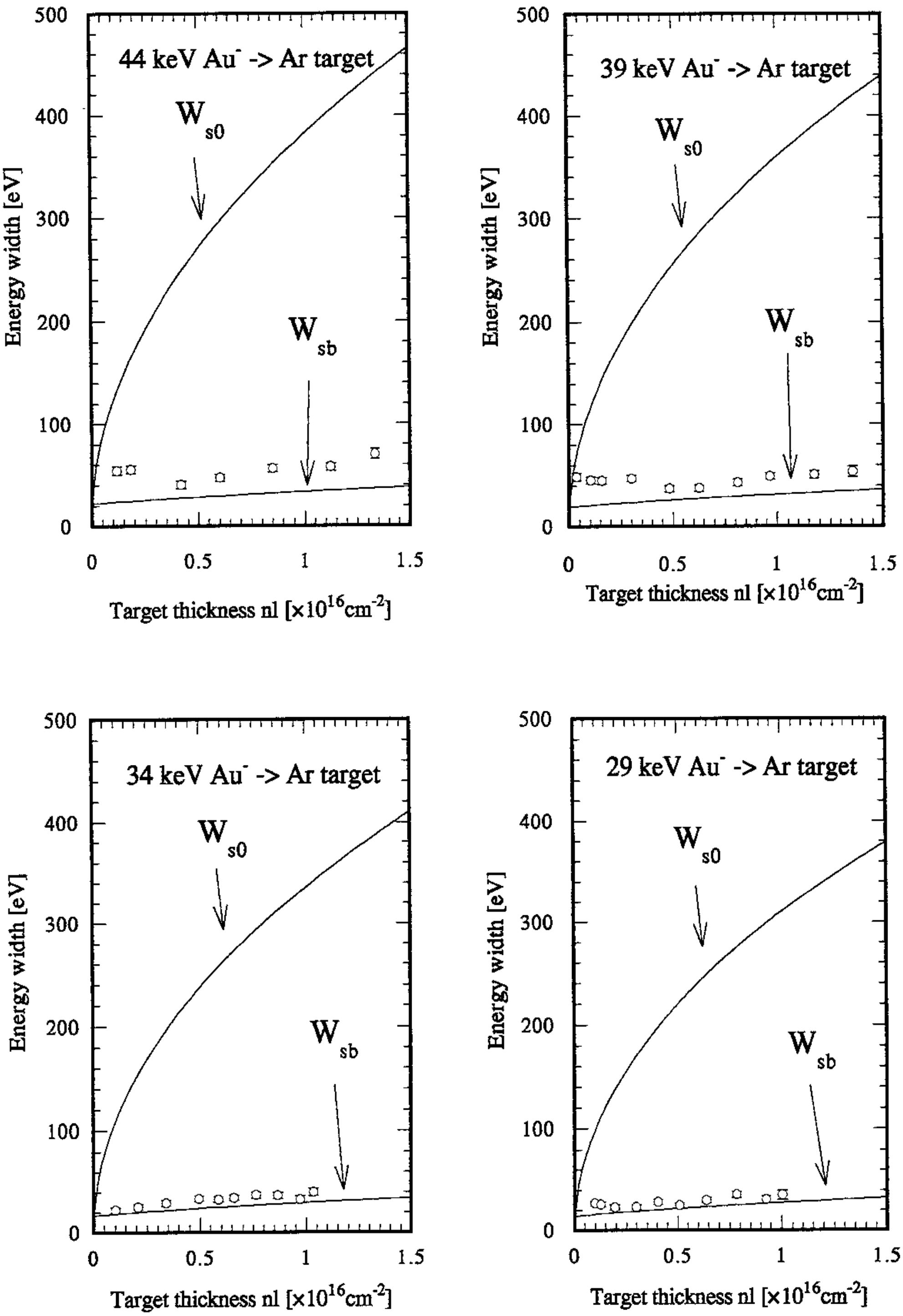

Fig. 37. The measured energy width and the theoretically calculated one plotted as a function of Ar target gas thickness for impact energies of 44, 39, 34 and 29 keV.

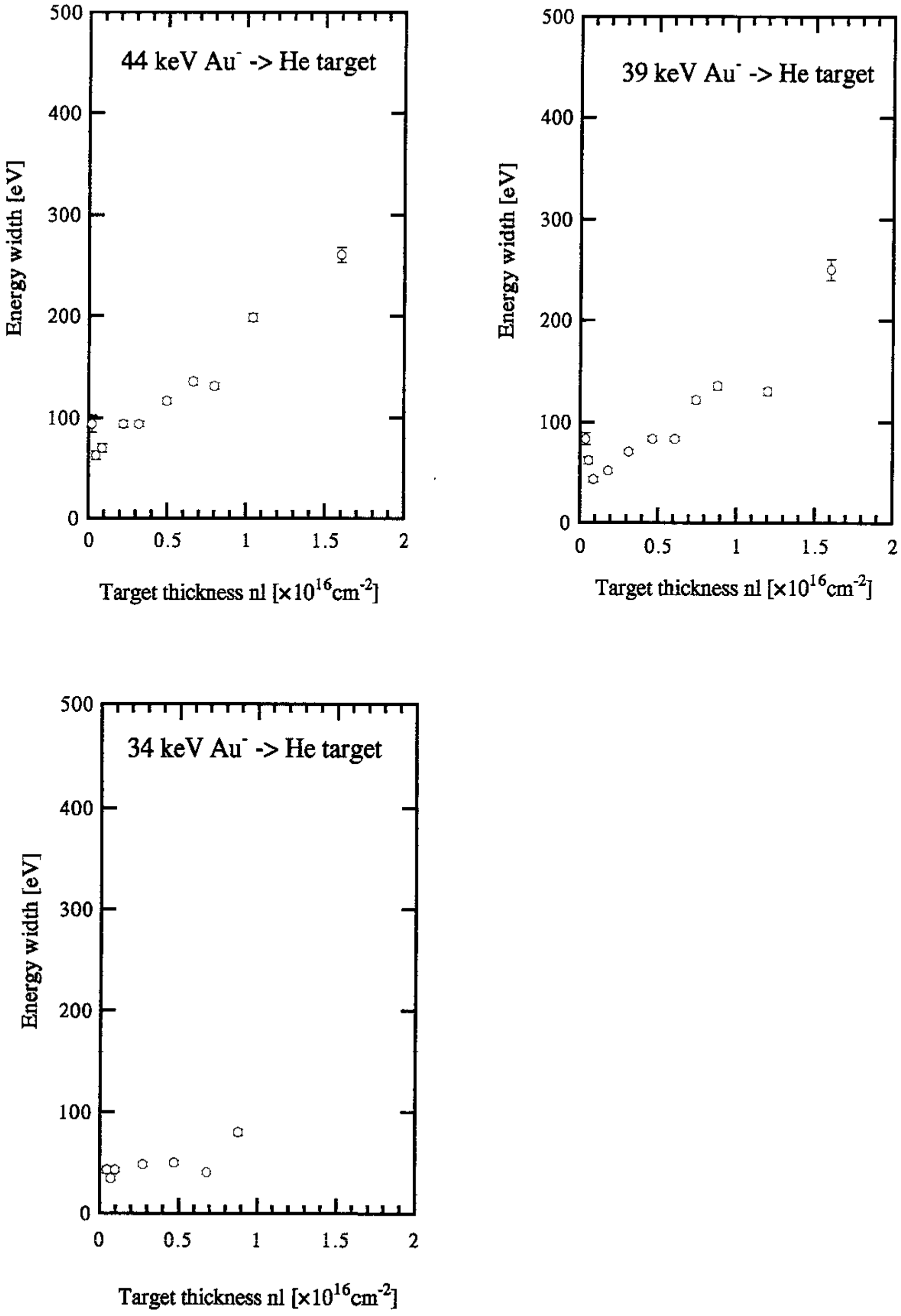

Fig. 38. The measured energy width plotted as a function of He target gas thickness for impact energies of 44, 39 and 34 keV.

width, W, is calculated as the following from the energy loss, $F_{1/2}$, original width of Au$^-$, W_{org}, and the energy straggling, Ω,

$$W = \sqrt{\Omega^2 + F_{1/2}{}^2 + W_{org}{}^2} \ . \tag{37}$$

is also shown in these figures.

In the region of target thickness smaller than about 2.5×10^{16} cm^{-2}, the energy width increases gradually as the gas thickness increases. The energy straggling calculated by considering minimum impact parameter, Ω_b, is closer to the measured value than that calculated by the original L.S.S. theory, Ω_0.

Because the condition of Eq.(19), on which the Firsov's theory can be used, is not satisfied on a He target, the calculated curve is not shown for a He target.

4-6 Cross Sections by Beam Attenuation Measurement

The electron detachment cross section, σ_D, can be mainly determined by two processes, that are two electron stripping ($\sigma_{-1,+1}$) and one electron stripping ($\sigma_{-1,0}$) processes. Then, the electron detachment cross section, σ_D, is expressed as,

$$\sigma_D = \sigma_{-1,0} + \sigma_{-1,+1} \ . \tag{38}$$

The differential equation for a negative beam current, I^-, is expressed as the following,

$$\frac{\mathrm{d}I^-}{\mathrm{d}x} = -n\left(\sigma_{-1,0} + \sigma_{-1,+1}\right)I^- \ . \tag{39}$$

Then,

$$I^- = I_0^- \exp\left\{-\left(\sigma_{-1,0} + \sigma_{-1,+1}\right)nl\right\} \ , \tag{40}$$

where I_0^- is the initial current of the negative beam and nl denotes the target thickness. The σ_D can be determined by beam attenuation curve, where the higher ionization is considered to be negligible in the present energy range.

Suppose that the beam intensity is uniform in the profile, the electron stripping cross section can be measured by the energy analyzer. Figure 39 shows the Au^- beam intensity as a function of target thickness of Ar at the impact energy 35, 30 and 20 keV by energy analyzer. The electron stripping cross sections calculated by Eq.(39), are 9.4×10^{-16}, 6.5×10^{-16} and 8.3×10^{-16} cm^2, respectively. Figure 40 shows the Au^- beam intensity as a function of target thickness at the impact energies of 44 and 24 keV measured by the movable Faraday cup. The electron stripping cross section are 7.2×10^{-16}, 1.6×10^{-16} cm^2, respectively.

Figure 41 shows the measured electron detachment cross sections and the theoretical one calculated by using Eq.(28), as shown in Fig. 27 and Fig. 28. They are consistent with the latter in order. The difference of the cross sections measured by two methods is due to the beam scattering effect. The measurements by the energy analyzer give a larger cross section than that by the Faraday cup, because the beam attenuation due to scattering is include.

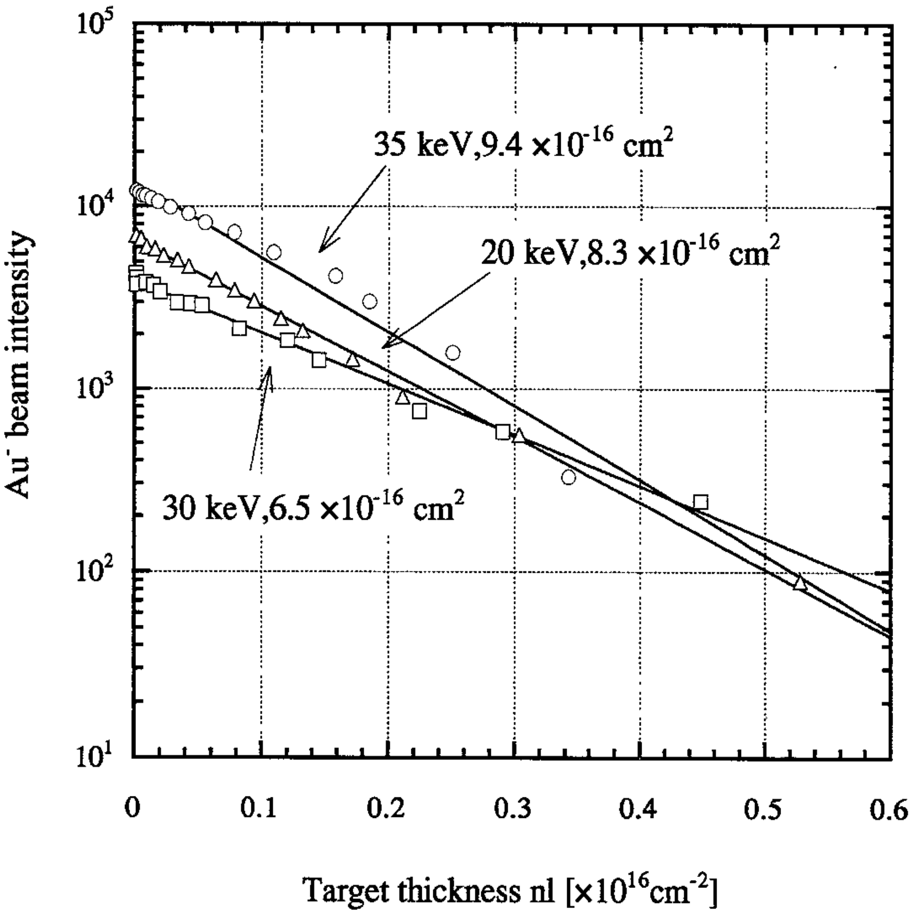

Fig. 39. Beam attenuation curves at impact energies of 35, 30 and 20 keV using by the energy analyzer.

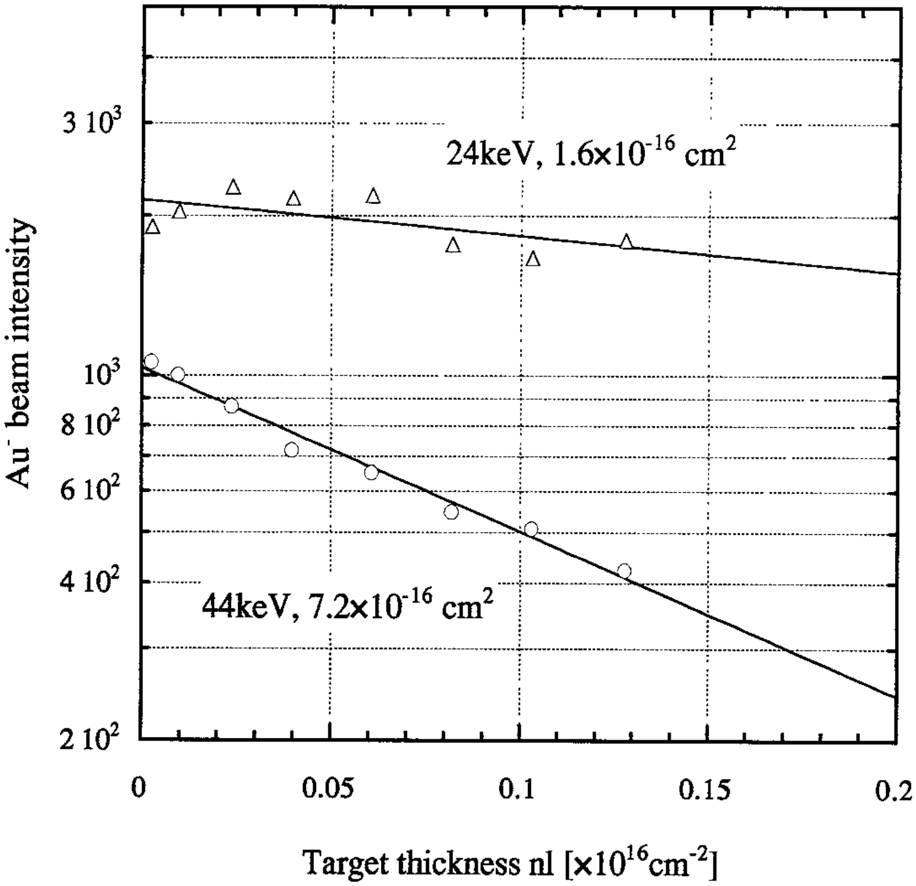

Fig. 40. Beam attenuation curves at impact energies of 44 and 24 keV using by the movable Faraday cup.

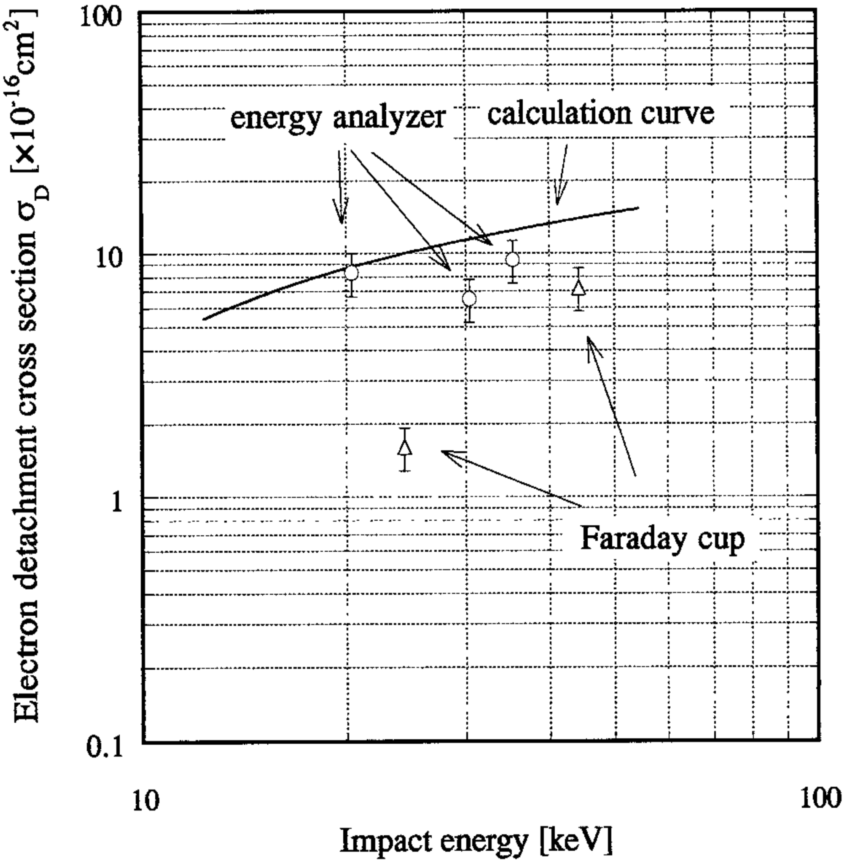

Fig. 41. The electron detachment cross section, σ_D, by theoretical calculation and measurements at Ar target.

4-7. Energy Width and Charge Fraction on 3 MV Tandem Acceleration System

In this section, the 3 MV tandem accelerator system is considered which will be applied to the 6 MeV HIBP for LHD. The performance of this system can be considered from two aspects, the energy width and the beam current.

At first, the energy width can be estimated from

1. the original energy width of an Au^- beam
2. the energy broadening on an Au^+ beam produced from an Au^- beam
3. the energy straggling by the multiple collisions
4. the voltage ripple of tandem power supply

The original energy width of Au^- beam is measured and it is about 5 eV as shown in Fig. 31.

Because the gas cell of the 3 MV tandem accelerator of LHD will have the same geometry as that of the present test stand, then, the restriction on the $\theta_{\max}$ is assumed to be same as in the present case. Therefore, the energy broadening due to the electron stripping, $F_{1/2}$, can be calculated to be 7 eV, and it does not depend upon the target mass as has been discussed in the paragraph 3-3.

The energy straggling, Ω_b, is a function of target thickness, nl, and it can be estimated as the paragraph 3-4.

The voltage ripple ratio of the 3 MV tandem power supply will be less than $\pm 10^{-5}$. Then, the broadening of the 6 MeV beam due to the ripple will be

$$W_{\text{ripple}} \leq 2 \cdot \left(3 \times 10^6\right) \times \left(2 \cdot 10^{-5}\right) = 120 \ \ [\text{eV}] \ . \qquad (41)$$

Consequently the energy width of 6 MeV Au+ beam, $W_{3\mathrm{MV}}$, can be estimated by the following equation,

$$W_{3\mathrm{MV}} = \sqrt{\{\Omega_{\mathrm{b}}(nl)\}^2 + F_{1/2}{}^2 + W_{\mathrm{org}}{}^2} + W_{\mathrm{ripple}} \ [\mathrm{eV}] \ . \qquad (42)$$

The second, charge fractions can be calculated from the cross sections. These cross sections are described in paragraph 3-5. In this paragraph, the electron loss and the scattering cross sections are considered, but electron capture is not considered. The electron loss cross sections, $\sigma_{i\,f}$, and scattering cross section, σ_{s}, for Ar target are calculated as the following,

$$\begin{array}{llll}
\sigma_{-1,0} = 35.6\times10^{-16}\ [\mathrm{cm}^2]\,, & \sigma_{-1,+1} = 15.8\times10^{-16}\ [\mathrm{cm}^2]\,, & & \\
\sigma_{-1,+2} = 9.1\times10^{-16}\ [\mathrm{cm}^2]\,, & \sigma_{-1,+3} = 5.7\times10^{-16}\ [\mathrm{cm}^2]\,, & & \\
\sigma_{0,+1} = 17.8\times10^{-16}\ [\mathrm{cm}^2]\,, & \sigma_{0,+2} = 9.4\times10^{-16}\ [\mathrm{cm}^2]\,, & & \\
\sigma_{0,+3} = 6.4\times10^{-16}\ [\mathrm{cm}^2]\,, & & & (43) \\
\sigma_{+1,+2} = 11.6\times10^{-16}\ [\mathrm{cm}^2]\,, & \sigma_{+1,+3} = 6.4\times10^{-16}\ [\mathrm{cm}^2]\,, & & \\
\sigma_{+2,+3} = 8.3\times10^{-16}\ [\mathrm{cm}^2]\,, & \sigma_{\mathrm{s}} = 0.04\times10^{-16}\ [\mathrm{cm}^2]\,. & &
\end{array}$$

The charge fractions can be calculated by the following rate equation,

$$\begin{aligned}
\frac{\mathrm{d}I^-}{\mathrm{d}x} &= -\sigma_{-1,0}I^- - \sigma_{-1,+1}I^- - \sigma_{-1,+2}I^- - \sigma_{-1,+3}I^- - \sigma_s I^- \\
\frac{\mathrm{d}I^0}{\mathrm{d}x} &= \sigma_{-1,0}I^- - \sigma_{0,+1}I^0 - \sigma_{0,+2}I^0 - \sigma_{0,+3}I^0 - \sigma_s I^0 \\
\frac{\mathrm{d}I^+}{\mathrm{d}x} &= \sigma_{-1,+1}I^- + \sigma_{0,+1}I^0 - \sigma_{+1,+2}I^+ - \sigma_{+1,+3}I^+ - \sigma_s I^+ \qquad (44) \\
\frac{\mathrm{d}I^{++}}{\mathrm{d}x} &= \sigma_{-1,+2}I^- + \sigma_{0,+2}I^0 + \sigma_{+1,+2}I^+ - \sigma_{+2,+3}I^{++} - \sigma_s I^{++}
\end{aligned}$$

$$\frac{dI^{+++}}{dx} = \sigma_{-1,+3}I^{-} + \sigma_{0,+3}I^{0} + \sigma_{+1,+3}I^{+} + \sigma_{+2,+3}I^{++} - \sigma_{s}I^{+++}$$

under the condition of

$I^{-}(0)=1,\ I^{0}(0)=0,\ I^{+}(0)=0,\ I^{++}(0)=0,\ I^{+++}(0)=0$,

where parameter, x , represents gas thickness, nl .

Figure 42 shows the energy width without power supply ripple and the charge fractions. From this figure, the tandem acceleration should be operated where target thickness is around the 6×10^{14} cm^{-2}. Together with the energy broadening due to the multiple collision at this target thickness, the total energy width of the Au^{+} beam produced in a gas cell of a tandem system might be less than several tens eV. The energy broadening due to the voltage ripple of the tandem power supply is about a hundred eV. Therefore, the total energy spread of an Au^{+} beam is mainly determined by the voltage ripple. It will be small enough for a HIBP diagnostics on LHD where the plasma potential is a few keV.

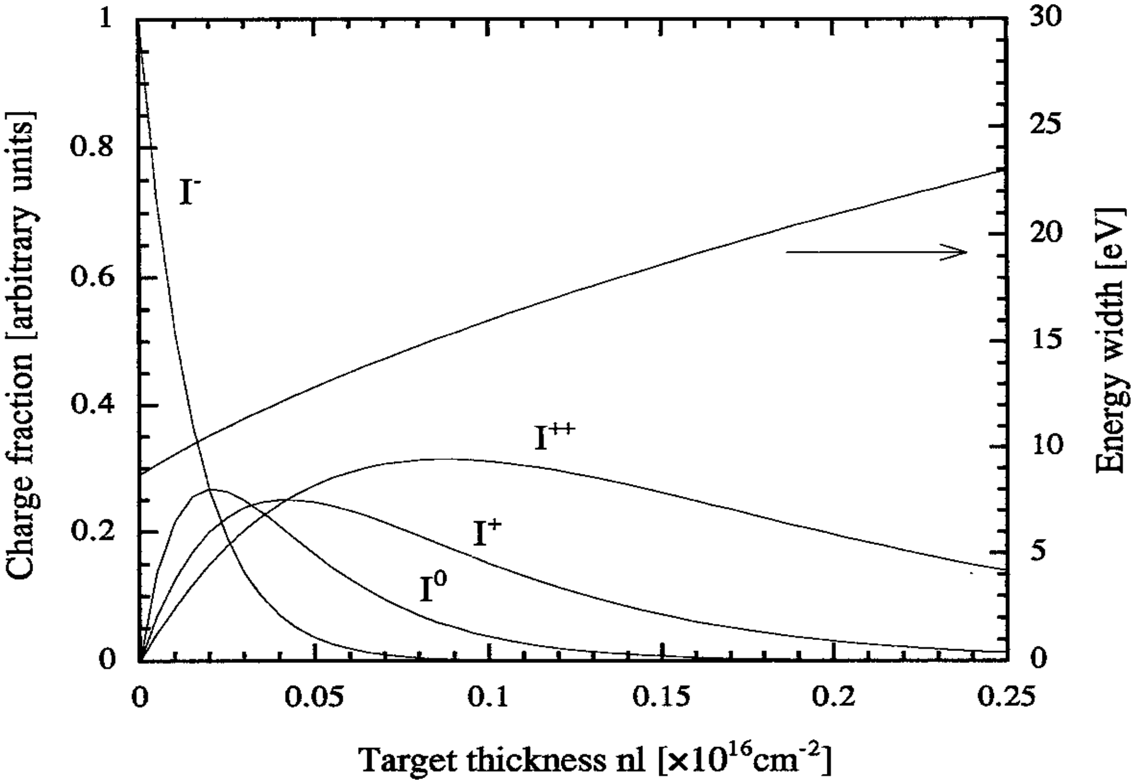

Fig. 42. The charge fractions and the energy width as functions of the target thickness at impact energy of 3 MeV for the Ar gas. The charge fractions are calculated by the rate equation, Eq.(44), and the energy width is calculated by energy broadening on the double charge stripping, $F_{1/2}$, and the energy straggling, Ω_b.

§5. Conclusion

In order to study the feasibility of a tandem accelerator system for the application to HIBP, a tandem acceleration test stand was constructed and the charge stripping mechanism and the tandem acceleration performance were studied. The energy width of an Au^- beam extracted from the plasma-sputter-type negative ion source is small enough to be used on a tandem accelerator for HIBP. When two electrons are stripped from a negative ion, the beam energy shift is about 12 eV. This can be explained that the sum of electron affinity and first ionization potential is lost from the initial energy.

Energy broadening due to the two-electron stripping process of gold ions ($Au^- \rightarrow Au^+$) in He, Ar, Kr and Xe is measured at a forward angle in the impact energy range from 24 to 44 keV. The FWHM is typically 20~80 eV, and it increases as the impact energy increases. Stripping with low Z target atoms results in a broader energy width. In order to explain the measured energy dependence and the target mass dependence of the spectrum width, a simple model using the semi-classical internal energy transfer function of Firsov's, and the scattering by the unified potential is proposed. Theoretical prediction of the present model reproduces the energy and mass dependence of the broadening. The absolute values of the theoretically predicted width are much smaller than the measured width.

In the region that multiple collisions are not negligible, the energy straggling is found much less than the prediction of the original L.S.S. theory. By imposing restriction on the integral over the impact parameter, the theoretical values approach to the measurement drastically.

The electron detachment cross sections are measured by beam attenuation method, and they are in the range of $1\sim10\times10^{-16}$ cm^2 and increase as the impact energy increases. The absolute values and the dependence on the impact energy are roughly explained by the theory.

Applying the present theoretical prediction to estimate the energy width of the 6 MeV Au^+ beam generated by a tandem acceleration system on LHD, the energy broadening due to the electron stripping will be less than that due to the ripple of the tandem accelerator power supply. Various electron loss cross sections and scattering cross sections have been estimated with the present theory, and the charge fractions have been calculated with them at 3 MeV. The optimum gas thickness is around 6×10^{14} cm^{-2} (2×10^{-4} Torr), and the energy spread including the multiple collision effect will be small enough for the measurement of a plasma potential of a few keV.

Finally, the cross sections and the energy spread of the output beam can be estimated for beams in a wide energy region by the present model. Those information are useful for a design of a tandem acceleration system.

References

[1] G. A. Hallock, J. Mathew, W. C. Jennings, R. L. Hickok, A. J. Wootton and R. C. Isler, Phys. Rev. Lett.. 56,1248 (1986)

[2] O. Motojima, et al., In Plasma Physics and Controlled Nuclear Fusion Research 1990 (proc. 13th Int. Conf. Washington, 1990), IAEA-CN-53/G-I-5, 513 (1990).

[3] A. Fujisawa, H. Iguchi, Y. Hamada, M. Sasao, J. Fujita, Rev. of Sci. Instrum. Vol.63, 3694 (1992).

[4] Y.Mori , G.D.Alton, A.Takagi, A.Ueno, and S.Fukumoto, Nucl. Instrum. Meth. A273, 5 (1988).

[5] Y. Mori, Rev. Sci. Instrum. Vol.63, 2357 (1992).

[6] A. Taniike, M. Sasao, A. Fujisawa, H. Iguchi, Y. Hamada, J. Fujita, M. Wada and Y. Mori, IEEE Transactions on Plasma Science, Vol. 22, No.4, August 1994.

[7] H. S. W. Massey and H. B. Gilbody, "Electronic and Ionic Impact Phenomena IV", Sec. 24, (1974, Oxford Press)

[8] Y. Okabe, M. Sasao, H. Yamaoka, M. Wada and J. Fujita, Jpn. J. Appl. Phys. Vol.30, 1428 (1991).

[9] Y. Okabe, M. Sasao, H. Yamaoka, M. Wada and J. Fujita, Jpn. J. Appl. Phys. Vol.30, 1307 (1991).

[10] J. K. Nørskov and B. I. Lundqvist, Phys. Rev. B19 (1979) 5661.

[11] A. Blandin, A. Nourtier and D. W. Hone, J. Physique Vol.37, 369 (1976).

[12] M. W. Thompson, Phil. Mag. 18 (1968) 377.

[13] N. Andersen, T. Andersen, L. Jepsen and J. Macek, J. Phys. B: At. Mol. Phys. 17, 2281 (1984).

[14] J. P. Biersack and J. F. Ziegler, Nucl. Inst. Meth. 194, 93 (1982).

[15] O.B.Firsov, Soviet Phys. JETP 9, 1076 (1959).

[16] J.Lindhard, M.Scharff, and H.E.Schiøtt, Mat. Fys. Medd. Dan. Vid. Selsk. 33 (1963) 14.

[17] P. Hvelplund, K. Dan. Vid. Selsk. Mat. Fys. Medd. 38, no.4 (1971).

Appendices

A. *Conductance Calculation for a Gas Cell*

In order to estimate the target thickness in a gas cell roughly, conductance calculation is done here. Fig. A-1(a) shows the geometry of the gas cell and its vicinity. Three simple columns are considered in this calculation, and those conductance are c_1, c_2 and c_3, respectively. Two ionization gauges are placed at the point A and D in the system, and the pressures at the point A, B, C and D are denoted p_0, p_1, p_2 and p_3, respectively.

Assuming that a gas flow rate Q at the point A is divided into two at the point B, then, the relations between the conductance and the pressure are expressed with the following equations,

$$Q = c_1(p_0 - p_2) \tag{A1}$$

$$\frac{Q}{2} = c_{2+3}(p_2 - p_1) \tag{A2}$$

$$\frac{Q}{2} = c_2(p_2 - p_3) \tag{A3}$$

where

$$\frac{1}{c_{2+3}} = \frac{1}{c_2} + \frac{1}{c_3}$$

The ratio, p_2/p_0, is obtained by Eq.(A1) and Eq.(A2) as the following,

$$\frac{p_2}{p_0} = \frac{2c_{2+3}\dfrac{p_1}{p_0} + c_1}{2c_{2+3} + c_1} \quad , \tag{A4}$$

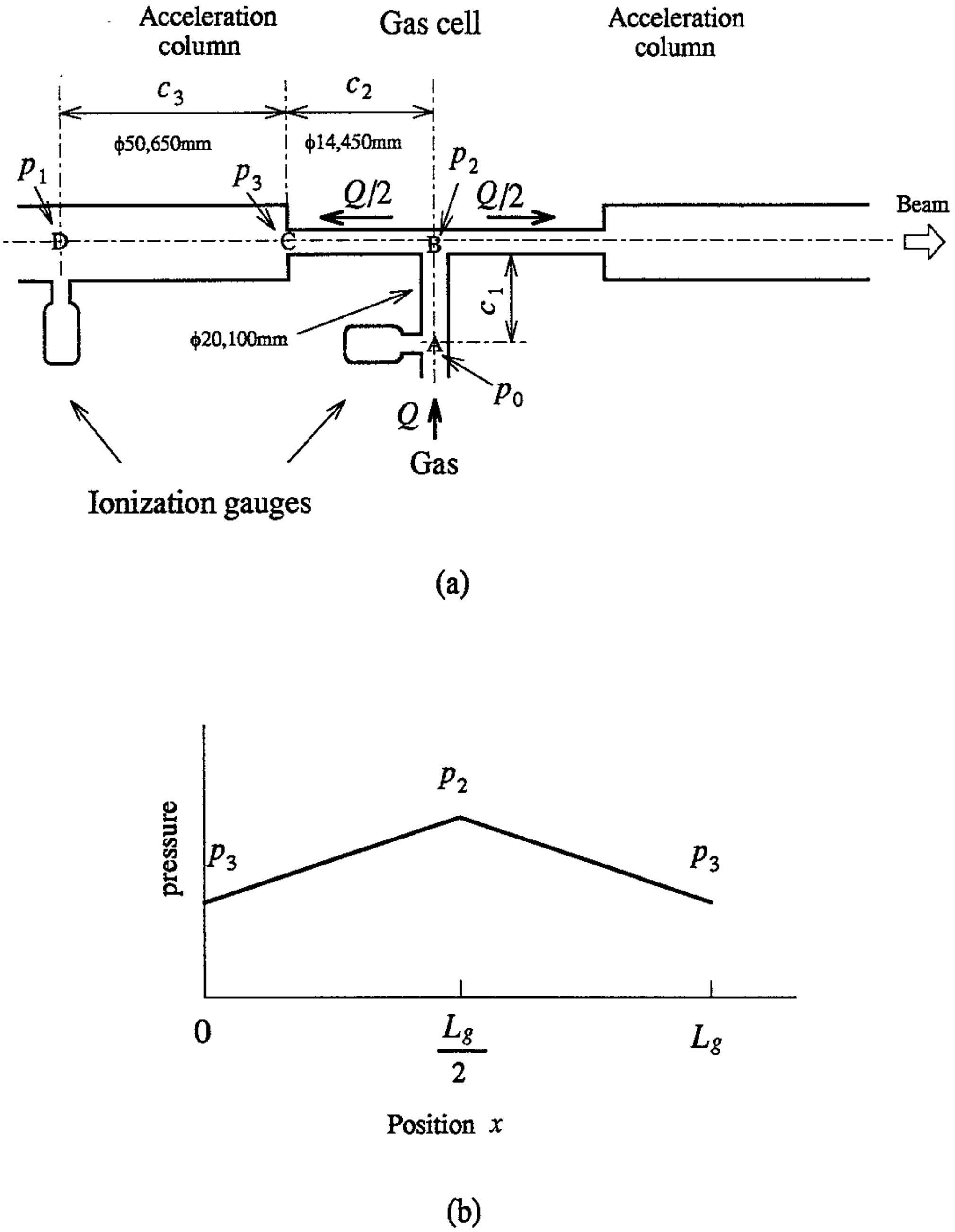

Fig. A-1. A schematic view of vacuum chamber at the gas cell and the acceleration columns (a). The gas pressure distribution in the cell is a function of the position, x , (b).

and the ratio, p_3/p_0, is also obtained by Eq.(A1) and Eq.(A3) as the following,

$$\frac{p_3}{p_0}=\left(1+\frac{c_1}{2c_2}\right)\frac{p_2}{p_0}-\frac{c_1}{2c_2} \quad . \tag{A5}$$

In this experimental system, the ratio, p_1/p_0, is directly measured by two gas gauges,

$$\frac{p_1}{p_0}=5.68\times10^{-3} \quad . \tag{A6}$$

The conductance, c_1, c_2 and c_3 for Ar gas are calculated to

$$c_1=8.5\,[\ell/\mathrm{s}] \ , \ c_2=0.65\,[\ell/\mathrm{s}] \text{ and } c_3=24\,[\ell/\mathrm{s}] \,.$$

Then, putting these values into Eq.(A4) and Eq.(A5), the ratios are obtained as the following,

$$\frac{p_2}{p_0}=0.87 \tag{A7}$$

$$\frac{p_3}{p_0}=0.02 \ . \tag{A8}$$

The gas pressure in the cell is proportional to the position, x , as shown in the Fig. A-1(b), and is expressed as the following,

$$p(x)=\left(\frac{\frac{p_2}{p_0}-\frac{p_3}{p_0}}{\frac{L_g}{2}}x+\frac{p_3}{p_0}\right)p_0=\left(\frac{2\cdot 0.85}{L_g}x+0.02\right)p_0$$

for $\left(0\le x\le \frac{L_g}{2}\right)$. (A9)

Therefore, the gas thickness can be calculated as the following,

$$\int_0^{2L_g} p(x)\mathrm{d}x=2\int_0^{L_g} p(x)\mathrm{d}x=\frac{p_0 L_g}{1.2} \qquad \text{(A10)}$$

$$nl=3.5\times 10^{16}\cdot\frac{p_0\cdot L_g}{1.2}\quad [\mathrm{cm}^{-2}]\,. \qquad \text{(A11)}$$

This result is not accurate because this estimation is not taken the fringing effect into account.

B. *Saturation of the Energy Broadening*

Elastic and inelastic processes result in the energy loss of an ion. In this experiment, the elastic energy loss is negligibly small because the scattering angle is restricted by the geometry of the experimental set up and the impact energy is small. Then, only the energy loss due to the inelastic process is considered in this section.

Firsov's inelastic energy transfer equation is simply expressed as the following,

$$T = \frac{C}{[1 + A \cdot b]^5} \ [\mathrm{eV}] \qquad \text{(B1)}$$

$$A = 3.1(Z_1 + Z_2)^{1/3} \cdot 10^7$$

$$C = (Z_1 + Z_2)^{5/3} \cdot 4.3 \times 10^{-8} \cdot \mathrm{v}$$

b [cm] : Impact parameter

v [cm/s] : Particle velocity.

The inverse function of Eq.(B1) and its derivative are,

$$b = \frac{1}{A}\left\{(C\mathrm{v})^{1/5} T^{-1/5} - 1\right\} \qquad \text{(B2)}$$

$$\frac{\mathrm{d}b}{\mathrm{d}T} = -\frac{(C\mathrm{v})^{1/5}}{5A} T^{-6/5} \ . \qquad \text{(B3)}$$

Then, the energy spectrum which is observed in the experiment, $F(\varepsilon)$, is proportional to multiplication of Eq.(B2) and Eq.(B3),

$$F(\varepsilon) \propto -b\frac{\mathrm{d}b}{\mathrm{d}T}$$

$$
\begin{aligned}
&= \frac{(C\mathrm{v})^{1/5}}{5A^2} T^{-6/5} \left\{ (C\mathrm{v})^{1/5} T^{-1/5} - 1 \right\} \\
&\equiv f(\varepsilon) \ .
\end{aligned}
\tag{B4}
$$

The maximum value of $F(\varepsilon)$, $f_{\max}$, is taken at $T = T_{\min}$,

$$
f_{\max} = \frac{(C\mathrm{v})^{1/5}}{5A^2} T_{\min}{}^{-6/5} \left\{ (C\mathrm{v})^{1/5} T_{\min}{}^{-1/5} - 1 \right\}
\tag{B5}
$$

where

$$
T_{\min} = 11.5 \quad [\mathrm{eV}] \ .
\tag{B6}
$$

Considering the full width at half maximum, $f_{1/2}$,

$$
f_{1/2} = \frac{1}{2} f_{\max}
\tag{B7}
$$

Putting Eq.(B4) and Eq.(B5) into Eq.(B7), we obtain

$$
\begin{aligned}
&\frac{(C\mathrm{v})^{1/5}}{5A^2} T^{-6/5} \left\{ (C\mathrm{v})^{1/5} T^{-1/5} - 1 \right\} \\
&= \frac{1}{2} \frac{(C\mathrm{v})^{1/5}}{5A^2} T_{\min}{}^{-6/5} \left\{ (C\mathrm{v})^{1/5} T_{\min}{}^{-1/5} - 1 \right\} \ .
\end{aligned}
\tag{B8}
$$

The function, $g(T)$, is

$$
\begin{aligned}
&g(T) = (C\mathrm{v})^{1/5} T^{-7/5} - T^{-6/5} \\
&- \frac{1}{2} (C\mathrm{v})^{1/5} T_{\min}{}^{-7/5} + \frac{1}{2} T_{\min}{}^{-6/5} \ .
\end{aligned}
\tag{B9}
$$

Consequently, the solution of $g(T_0)=0$ gives the energy loss at FWHM. Figure B-1 shows the function, $g(T)$, for the impact energy of 10 keV, 100 keV, 1 MeV and 10 MeV for a Xe target. All solutions of $g(T_0)=0$ are about T = 18 eV, the energy broadening is represent to $T_0 - T_{\min} \approx 7$ eV. Thus, the energy broadening does not depend on the impact energy.

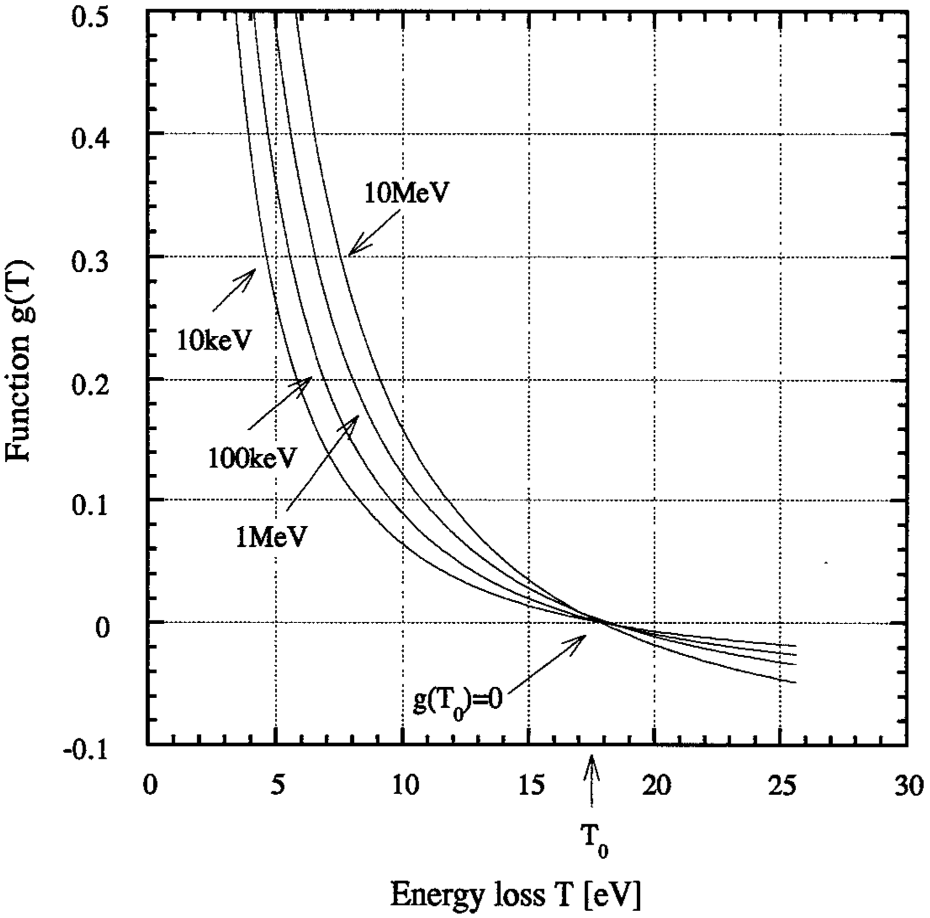

Fig. B-1. The function, *g* (*T*), for impact energies of 10 keV, 100 keV, 1 MeV and 10 MeV at a Xe target. The solution of *g* (*T*)=0 gives the energy at FWHM of *F* (ε).

C. *The Calculation Code for the Elastic and the Inelastic Process*

```
C
C     BMIN AND BMAX CALCULATION PROGRAM
C                                AKIRA TANIIKE
C     BEL=BMAX
C     BIN=BMIN
C     ———> CROSS SECTION CALC
C
C       THIS PROGRAME USE SSL2 SUBROUTINE
C                              (FOR FUJITSU S-4/IX)
C
      IMPLICIT REAL*8(A-H,O-Z)
      COMMON /PAR/R0,B,EN,Z1,Z2,DM1,DM2
      PARAMETER(ZERO=0.0D0)
      PARAMETER(TWO=2.0D0)
      PARAMETER(ONE=1.0D0)
      PAI=DATAN(ONE)*4.0D0
C
C      Z NUMBER
C
      ZAU=79.0D0
      ZRN=86.0D0
      ZXE=54.0D0
      ZKR=36.0D0
      ZAR=18.0D0
      ZNE=10.0D0
      ZHE=2.0D0
C
C       MASS NUMBER
C
      DMAU=196.96654D0
      DMRN=222D0
      DMXE=131.29D0
      DMKR=83.80D0
      DMAR=39.948D0
      DMNE=20.1797D0
      DMHE=4.002602D0
C
      ENMIN=4.35D3
      ENMAX=54.35D3
      ENDIV=0.5D3
C
      OPEN(9,FILE='Ar.dat')
C
```

```
C          AU^- ---> AR TARGET
C
      Z1=ZAU
      Z2=ZAR
      DM1=DMAU
      DM2=DMAR
C
      WRITE(6,100)
  100 FORMAT(1H ,'-1 -> +1 CROSS SECTION CALC')
C
C
      MULTI=ONE
      DO 200,EN=ENMIN,ENMAX,ENDIV
        TM=4.0D0*DM1*DM2*EN/(DM1+DM2)**TWO
        CALL INEL(TIN,BIN)
        DLTH=DATAN(8.0D0/1.4D3)*MULTI
        O1=(DM1/DM2)*SIN(DLTH)
        O2=O1/DSQRT(ONE-O1**TWO)
        THMAX=DLTH+DATAN(O2)
C
        CALL ELAS(TM,THMAX,TEL,BEL)
        IF((BIN-BEL).LT.ZERO) THEN
          SIGMA=ZERO
        ELSE
          SIGMA=PAI*(BIN**TWO-BEL**TWO)
        ENDIF
        WRITE(6,160) EN,SIGMA
        WRITE(9,170) EN,SIGMA
  200 CONTINUE
  160 FORMAT(1H ,'EN=',D18.10,' SIGMA=',D23.15)
  170 FORMAT(1H ,D18.10,',',D23.15)
      STOP
      END
C
C   -----------------------------------------------------
C          BMAX CALC
C   -----------------------------------------------------
C
      SUBROUTINE ELAS(TM,THMAX,TEL,BEL)
      IMPLICIT REAL*8 (A-H,O-Z)
      COMMON /PAR/R0,B,EN,Z1,Z2,DM1,DM2
      EXTERNAL FUN1
      DIMENSION DIV(5)
      PARAMETER(ZERO=0.0D0)
      PARAMETER(ONE=1.0D0)
      PARAMETER(TWO=2.0D0)
```

```
      PARAMETER(TEN=1.0D1)
      EPSA=1.0D-4
      EPSR=0.0D0
      NMIN=20
      NMAX=689
      PAI=DATAN(ONE)*4.0D0
C
      DIV(1)=1.0D-1
      DO 100,I=2,5
      DIV(I)=DIV(I-1)/TEN
  100 CONTINUE
C
      S=-ONE
      B=3.0D0
C
      DO 10,I=1,5
   30   CONTINUE
        B=B+(S**I)*DIV(I)
        R0=CALR0(B,EN,Z1,Z2)
        CALL DAQEH(FUN1,EPSA,EPSR,NMIN,NMAX,SSS,ERR,N,ICON)
        TH=PAI-TWO*SSS
        IF((TH-THMAX)*(S**I).GT.ZERO) GO TO 30
   10 CONTINUE
      BEL=B
      TEL=TM*((DSIN(TH/TWO))**TWO)
      RETURN
      END
C
C    -------------------------------------------------------
C                   BMIN CALC
C    -------------------------------------------------------
C
      SUBROUTINE INEL(TIN,BIN)
      IMPLICIT REAL*8 (A-H,O-Z)
      COMMON /PAR/R0,B,EN,Z1,Z2,DM1,DM2
      DIMENSION DCS(10)
      PARAMETER(ZERO=0.0D0)
      PARAMETER(ONE=1.0D0)
      PARAMETER(THREE=3.0D0)
      PARAMETER(FIVE=5.0D0)
      PARAMETER(TEN=1.0D1)
C
C         -1 -> 0
      DCS(1)=2.3086D0
C         -1 -> +1
      DCS(2)=11.52D0
```

```
C          -1 -> +2
      DCS(3)=32.12D0
C          -1 -> +3
      DCS(4)=69.52D0
C           0 -> +1
      DCS(5)=9.21D0
C           0 -> +2
      DCS(6)=29.81D0
C           0 -> +3
      DCS(7)=67.21D0
C          +1 -> +2
      DCS(8)=20.6D0
C          +1 -> +3
      DCS(9)=58.0D0
C          +2 -> +3
      DCS(10)=37.4D0
C
C
      QQ13=(Z1+Z2)**(ONE/THREE)
      QQ53=(Z1+Z2)**(FIVE/THREE)
      VEL=9.89D4*DSQRT(EN)
      CCC=QQ53*4.3D-8*VEL
      AAA=QQ13*3.1D-1
C
      NO=2
      BIN=((CCC**(ONE/FIVE))*(DCS(NO)**(-ONE/FIVE))-ONE)/AAA
      RETURN
      END
C
C    ------------------------------------------------------------
C               POTENTIAL
C    ------------------------------------------------------------
C
      REAL*8 FUNCTION FUN1(X)
      IMPLICIT REAL*8(A-H,O-Z)
      COMMON /PAR/R0,B,EN,Z1,Z2,DM1,DM2
      PARAMETER(ZERO=0.0D0)
      PARAMETER(ONE=1.0D0)
      PARAMETER(TWO=2.0D0)
C
      R=X+R0
      FUN1=ZERO
      IF(R.NE.ZERO) THEN
        VP=CALV1(Z1,Z2,R)
        FUN1=B/(DSQRT(ONE-(B/R)**TWO-VP/EN)*(R**TWO))
      ENDIF
```

```
      RETURN
      END
C
C    ------------------------------------------------------------
C               POTENTIAL
C    ------------------------------------------------------------
C
      REAL*8 FUNCTION CALV1(Z1,Z2,R)
      IMPLICIT REAL*8(A-H,O-Z)
      PARAMETER(ZERO=0.0D0)
C
      V1=VVV(R,Z1)
      V2=VVV(R,Z2)
      IF((V1*V2).LT.ZERO) THEN
        WRITE(6,100) R,V1,V2
        STOP
      ELSE
        CALV1=DSQRT(V1*V2)
      ENDIF
  100 FORMAT(1H ,'ERROR',' R=',D23.15,'V1=',D23.15,'V2=',D23.15)
      RETURN
      END
C
C    ------------------------------------------------------------
C             UNIFIED POTENTIAL BY ZIEGLER
C    ------------------------------------------------------------
C
      REAL*8 FUNCTION VVV(SR,Z)
      IMPLICIT REAL*8(A-H,O-Z)
      PARAMETER(ZERO=0.0D0)
      PARAMETER(ONE=1.0D0)
      PARAMETER(TWO=2.0D0)
      PARAMETER(THREE=3.0D0)
      PARAMETER(FOUR=4.0D0)
      PARAMETER(SEVEN=7.0D0)
      PARAMETER(ELEP2=14.4D0)
C
      ZLR=(Z**(ONE/THREE))*SR
      X=ZLR/0.295D0
      Q1=0.09D0*DEXP(-0.19D0*X)
      Q2=0.61D0*DEXP(-0.57D0*X)
      Q3=0.3D0*DEXP(-TWO*X)
      FAI1=Q1+Q2+Q3
      IF(X.EQ.ZERO) THEN
        V=Z*Z*ELEP2/SR
      ELSE
```

```
       FAIN1=(SEVEN*ZLR)**(-TWO)
       FAIN2=ZLR/FOUR
       FAIN3=(ZLR/SEVEN)**TWO
       FAI2=0.07D0*DEXP(-FAIN1-FAIN2-FAIN3)
       V=Z*Z*ELEP2*(FAI1-(Z**(-TWO/THREE))*FAI2)/SR
      ENDIF
      IF(V.GT.0)THEN
        VVV=V
      ELSE
        VVV=0
      ENDIF
      RETURN
      END
C
C   ------------------------------------------------------------
C          R0 CALC
C   ------------------------------------------------------------
C
      REAL*8 FUNCTION CALR0(B,EN,Z1,Z2)
      IMPLICIT REAL*8(A-H,O-Z)
      DIMENSION DIV(9)
      PARAMETER(ZERO=0.0D0)
      PARAMETER(ONE=1.0D0)
      PARAMETER(TWO=2.0D0)
      PARAMETER(TEN=1.0D1)
C
      DIV(1)=1.0D-4
      DO 100,I=2,9
        DIV(I)=DIV(I-1)/TEN
  100 CONTINUE
C
      S=-ONE
      R=B
      DO 10,I=1,9
   30   CONTINUE
        R=R-(S**I)*DIV(I)
        V=CALV1(Z1,Z2,R)
        F=1-(B/R)**TWO-V/EN
        IF(F*(S**I).GT.ZERO) GO TO 30
   10 CONTINUE
      CALR0=R
      RETURN
      END
```

Recent Issues of NIFS Series

NIFS-304 K. Ida, H. Idei, H. Sanuki, K. Itoh, J. Xu, S. Hidekuma, K. Kondo, A. Sahara, H. Zushi, S.-I. Itoh, A. Fukuyama, K. Adati, R. Akiyama, S. Bessho, A. Ejiri, A. Fujisawa, M. Fujiwara, Y. Hamada, S. Hirokura, H. Iguchi, O. Kaneko, K. Kawahata, Y. Kawasumi, M. Kojima, S. Kubo, H. Kuramoto, A. Lazaros, R. Liang, K. Matsuoka, T. Minami, T. Mizuuchi, T. Morisaki, S. Morita, K. Nagasaki, K. Narihara, K. Nishimura, A. Nishizawa, T. Obiki, H. Okada, S. Okamura, T. Ozaki, S. Sakakibara, H. Sakakita, A. Sagara, F. Sano, M. Sasao, K. Sato, K.N. Sato, T. Saeki, S. Sudo, C. Takahashi, K. Tanaka, K. Tsumori, H.Yamada, I. Yamada, Y. Takita, T. Tuzuki, K. Toi and T. Watari,
Control of Radial Electric Field in Torus Plasma; Sep. 1994
(IAEA-CN-60/A-2-IV-2)

NIFS-305 T. Hayashi, T. Sato, N. Nakajima, K. Ichiguchi, P. Merkel, J. Nührenberg, U. Schwenn, H. Gardner, A. Bhattacharjee and C.C.Hegna,
Behavior of Magnetic Islands in 3D MHD Equilibria of Helical Devices;
Sep. 1994 (IAEA-CN-60/D-2-II-4)

NIFS-306 S. Murakami, M. Okamoto, N. Nakajima, K.Y. Watanabe, T. Watari, T. Mutoh, R. Kumazawa and T. Seki,
Monte Carlo Simulation for ICRF Heating in Heliotron/Torsatrons;
Sep. 1994 (IAEA-CN-60/D-P-I-14)

NIFS-307 Y. Takeiri, A. Ando, O. Kaneko, Y. Oka, K. Tsumori, R. Akiyama, E. Asano, T. Kawamoto, T. Kuroda, M. Tanaka and H. Kawakami,
Development of an Intense Negative Hydrogen Ion Source with a Wide-Range of External Magnetic Filter Field; Sep. 1994

NIFS-308 T. Hayashi, T. Sato, H.J. Gardner and J.D. Meiss,
Evolution of Magnetic Islands in a Heliac; Sep. 1994

NIFS-309 H. Amo, T. Sato and A. Kageyama,
Intermittent Energy Bursts and Recurrent Topological Change of a Twisting Magnetic Flux Tube; Sep.1994

NIFS-310 T. Yamagishi and H. Sanuki,
Effect of Anomalous Plasma Transport on Radial Electric Field in Torsatron/Heliotron; Sep. 1994

NIFS-311 K. Watanabe, T. Sato and Y. Nakayama,
Current-profile Flattening and Hot Core Shift due to the Nonlinear Development of Resistive Kink Mode; Oct. 1994

NIFS-312 M. Salimullah, B. Dasgupta, K. Watanabe and T. Sato,
Modification and Damping of Alfvén Waves in a Magnetized Dusty Plasma; Oct. 1994

NIFS-313 K. Ida, Y. Miura, S -I. Itoh, J.V. Hofmann, A. Fukuyama, S. Hidekuma,
H. Sanuki, H. Idei, H. Yamada, H. Iguchi, K. Itoh,
Physical Mechanism Determining the Radial Electric Field and its Radial Structure in a Toroidal Plasma; Oct. 1994

NIFS-314 Shao-ping Zhu, R. Horiuchi, T. Sato and The Complexity Simulation Group,
Non-Taylor Magnetohydrodynamic Self-Organization; Oct. 1994

NIFS-315 M. Tanaka,
Collisionless Magnetic Reconnection Associated with Coalescence of Flux Bundles; Nov. 1994

NIFS-316 M. Tanaka,
Macro-EM Particle Simulation Method and A Study of Collisionless Magnetic Reconnection; Nov. 1994

NIFS-317 A. Fujisawa, H. Iguchi, M. Sasao and Y. Hamada,
Second Order Focusing Property of 210° Cylindrical Energy Analyzer; Nov. 1994

NIFS-318 T. Sato and Complexity Simulation Group,
Complexity in Plasma - A Grand View of Self- Organization; Nov. 1994

NIFS-319 Y. Todo, T. Sato, K. Watanabe, T.H. Watanabe and R. Horiuchi,
MHD-Vlasov Simulation of the Toroidal Alfvén Eigenmode; Nov. 1994

NIFS-320 A. Kageyama, T. Sato and The Complexity Simulation Group,
Computer Simulation of a Magnetohydrodynamic Dynamo II: Nov. 1994

NIFS-321 A. Bhattacharjee, T. Hayashi, C.C.Hegna, N. Nakajima and T. Sato,
Theory of Pressure-induced Islands and Self-healing in Three-dimensional Toroidal Magnetohydrodynamic Equilibria; Nov. 1994

NIFS-322 A. Iiyoshi, K. Yamazaki and the LHD Group,
Recent Studies of the Large Helical Device; Nov. 1994

NIFS-323 A. Iiyoshi and K. Yamazaki,
The Next Large Helical Devices; Nov. 1994

NIFS-324 V.D. Pustovitov
Quasisymmetry Equations for Conventional Stellarators; Nov. 1994

NIFS-325 A. Taniike, M. Sasao, Y. Hamada, J. Fujita, M. Wada,
The Energy Broadening Resulting from Electron Stripping Process of a Low Energy Au^- *Beam;* Dec. 1994

NIFS-326 I. Viniar and S. Sudo,
New Pellet Production and Acceleration Technologies for High Speed Pellet Injection System "HIPEL" in Large Helical Device; Dec. 1994

NIFS-327 Y. Hamada, A. Nishizawa, Y. Kawasumi, K. Kawahata, K. Itoh, A. Ejiri,

K. Toi, K. Narihara, K. Sato, T. Seki, H. Iguchi, A. Fujisawa, K. Adachi,
S. Hidekuma, S. Hirokura, K. Ida, M. Kojima, J. Koong, R. Kumazawa,
H. Kuramoto, R. Liang, T. Minami, H. Sakakita, M. Sasao, K.N. Sato,
T. Tsuzuki, J. Xu, I. Yamada, T. Watari,
Fast Potential Change in Sawteeth in JIPP T-IIU Tokamak Plasmas;
Dec. 1994

NIFS-328 V.D. Pustovitov,
Effect of Satellite Helical Harmonics on the Stellarator Configuration;
Dec. 1994

NIFS-329 K. Itoh, S-I. Itoh and A. Fukuyama,
A Model of Sawtooth Based on the Transport Catastrophe; Dec. 1994

NIFS-330 K. Nagasaki, A. Ejiri,
Launching Conditions for Electron Cyclotron Heating in a Sheared Magnetic Field; Jan. 1995

NIFS-331 T.H. Watanabe, Y. Todo, R. Horiuchi, K. Watanabe, T. Sato,
An Advanced Electrostatic Particle Simulation Algorithm for Implicit Time Integration; Jan. 1995

NIFS-332 N. Bekki and T. Karakisawa,
Bifurcations from Periodic Solution in a Simplified Model of Two-dimensional Magnetoconvection; Jan. 1995

NIFS-333 K. Itoh, S.-I. Itoh, M. Yagi, A. Fukuyama,
Theory of Anomalous Transport in Reverse Field Pinch; Jan. 1995

NIFS-334 K. Nagasaki, A. Isayama and A. Ejiri
Application of Grating Polarizer to 106.4GHz ECH System on Heliotron-E; Jan. 1995

NIFS-335 H. Takamaru, T. Sato, R. Horiuchi, K. Watanabe and Complexity Simulation Group,
A Self-Consistent Open Boundary Model for Particle Simulation in Plasmas; Feb. 1995

NIFS-336 B.B. Kadomtsev,
Quantum Telegragh : is it possible?; Feb. 1995

NIFS-337 B.B.Kadomtsev,
Ball Lightning as Self-Organization Phenomenon; Feb. 1995

NIFS-338 Y. Takeiri, A. Ando, O. Kaneko, Y. Oka, K. Tsumori, R. Akiyama, E. Asano, T. Kawamoto, M. Tanaka and T. Kuroda,
High-Energy Acceleration of an Intense Negative Ion Beam; Feb. 1995

NIFS-339 K. Toi, T. Morisaki, S. Sakakibara, S. Ohdachi, T.Minami, S. Morita,
H. Yamada, K. Tanaka, K. Ida, S. Okamura, A. Ejiri, H. Iguchi,

K. Nishimura, K. Matsuoka, A. Ando, J. Xu, I. Yamada, K. Narihara, R. Akiyama, H. Idei, S. Kubo, T. Ozaki, C. Takahashi, K. Tsumori,
H-Mode Study in CHS; Feb. 1995

NIFS-340 T. Okada and H. Tazawa,
Filamentation Instability in a Light Ion Beam-plasma System with External Magnetic Field; Feb. 1995

NIFS-341 T. Watanbe, G. Gnudi,
A New Algorithm for Differential-Algebraic Equations Based on HIDM; Feb. 13, 1995

NIFS-342 Y. Nejoh,
New Stationary Solutions of the Nonlinear Drift Wave Equation; Feb. 1995

NIFS-343 A. Ejiri, S. Sakakibara and K. Kawahata,
Signal Based Mixing Analysis for the Magnetohydrodynamic Mode Reconstruction from Homodyne Microwave Reflectometry; Mar.. 1995

NIFS-344 B.B.Kadomtsev, K. Itoh, S.-I. Itoh
Fast Change in Core Transport after L-H Transition; Mar. 1995

NIFS-345 W.X. Wang, M. Okamoto, N. Nakajima and S. Murakami,
An Accurate Nonlinear Monte Carlo Collision Operator; Mar. 1995

NIFS-346 S. Sasaki, S. Takamura, S. Masuzaki, S. Watanabe, T. Kato, K. Kadota,
Helium I Line Intensity Ratios in a Plasma for the Diagnostics of Fusion Edge Plasmas; Mar. 1995

NIFS-347 M. Osakabe,
Measurement of Neutron Energy on D-T Fusion Plasma Experiments; Apr. 1995

NIFS-348 M. Sita Janaki, M.R. Gupta and Brahmananda Dasgupta,
Adiabatic Electron Acceleration in a Cnoidal Wave; Apr. 1995

NIFS-349 J. Xu, K. Ida and J. Fujita,
A Note for Pitch Angle Measurement of Magnetic Field in a Toroidal Plasma Using Motional Stark Effect; Apr. 1995

NIFS-350 J. Uramoto,
Characteristics for Metal Plate Penetration of a Low Energy Negative Muonlike or Pionlike Particle Beam: Apr. 1995

NIFS-351 J. Uramoto,
An Estimation of Life Time for A Low Energy Negative Pionlike Particle Beam: Apr. 1995